MODITIC

large-eddy simulations of dense gas dispersion in urban environments

—

Daniel Eriksson
Andreas Osnes
Oskar Parmhed
Emma M. M. Wingstedt
Guillaume Leroy

MODITIC

large-eddy simulations of dense gas dispersion in urban environments

Daniel Eriksson
Andreas Osnes
Oskar Parmhed
Emma M. M. Wingstedt
Guillaume Leroy

Norwegian Defence Research Establishment (FFI)   13 October 2016

Keywords

Computational Fluid Dynamics (CFD)
Spredning
Gassutslipp
Vindtunnel
Turbulent strømning
Atmosfærisk turbulens

Summary

The European Defence Agency (EDA) project B-1097-ESM4-GP "MOdelling the DIspersion of Toxic Industrial Chemicals in urban environments" (MODITIC) (2012 – 2016) has studied the release and transport of neutral and non-neutral chemicals in complex urban environments, in order to enhance the understanding of the dominating physical processes involved, and to support improvements in modelling techniques.

This report describes the work conducted using large-eddy simulations (LES) to simulate release and dispersion of neutral and dense gases. The dispersion process takes place in geometries with increasing complexity, and thus an increasingly complex flow field. The main purpose of the study is to improve the methodology for high fidelity dispersion models, to study the simulated effects of dense gas release, and to validate the results against wind tunnel data. The simulations reported in this work element, WE5300, have been performed by the Swedish Defence Research Agency (FOI), the Institut National de l'Environnement Industriel et des Risques (INERIS), and the Norwegian Defence Research Establishment (FFI) using different solvers and methods to treat the dense gas release. In this report, results from the solvers OpenFOAM and CDP are presented.

Results show that the methods used managed to predict the release and dispersion of both dense and neutral gas very well compared to the wind tunnel experiments. The complex flow fields were also simulated correctly. In all cases studied, there was a big difference in the dispersion pattern between dense and neutral gas. The dense gas was transported upwind from the source, against the wind, and the plume spread close to the ground and more laterally compared to the neutral gas. It was also seen that the dense gas changed the local wind field which led to reduced mixing and lower turbulence kinetic energy in areas with high concentrations. In order to assure satisfactory results, special care needs to be taken to the generation of the incoming turbulent boundary layer. This is especially true when there is no geometry (e.g. buildings) affecting the wind field.

Sammendrag

European Defence Agency-prosjektet B-1097-ESM4-GP MODITIC (MOdelling the DIspersion of Toxic Industrial Chemicals in urban environments) har studert utslipp og spredning av nøytrale og ikke-nøytrale industrikjemikalier i urbane miljøer. Målene er både å øke kunnskapen om de dominerende fysikalske prosessene som er involvert og å støtte opp om forbedring av modelleringsteknikker.

Denne rapporten beskriver arbeidet, som er utført ved hjelp av large-eddy simuleringer (LES), med å simulere utslipp og spredning av nøytrale og ikke-nøytrale gasser. Gassene spres i geometrier med økende kompleksitet, og dermed et stadig mer komplekst vindfelt. Hovedformålet med studien er å forbedre metodikken for high fidelity-spredningsmodeller, å studere de simulerte effektene av tunggass-utslipp, og å validere resultatene mot vindtunneldata. Simuleringene rapportert i WE5300 er utført av Totalförsvarets Forskningsinstitut (FOI), Institut National de l'Environnement Industriel et des Risques (INERIS) og Forsvarets forskningsinstitutt (FFI) ved hjelp av ulike løsere og ulike metoder for å behandle spredningen av tunggass. I denne rapporten presenteres resultatene fra programmene OpenFOAM og CDP.

Resultatene viser at metodene som har blitt brukt er i stand til å forutsi utslipp og spredning av både tung og nøytral gass meget godt sammenlignet med vindtunnelresultatene. De komplekse strømningsfeltene ble også simulert riktig. I alle scenarier som er studert var det stor forskjell i spredningsmønstrene i tung- og nøytralgasstilfellene: den tunge gassen ble transportert fra kilden mot vinden, og skyen ble spredt nær bakken og mer sideveis i forhold til den nøytrale gassen. Det ble også observert at den tunge gassen endret det lokale vindfeltet, noe som førte til redusert miksing og lavere turbulent kinetisk energi i områder med høye konsentrasjoner. For å sikre tilfredsstillende resultater må det tas særskilt hensyn til genereringen av det innkommende turbulente grensesjiktet. Dette gjelder spesielt når det ikke er noen geometri (for eksempel bygninger) som påvirker vindfelt i stor grad.

Contents

Preface

This work is part of the European Defence Agency (EDA) project B-1097-ESM4-GP "MOdelling the DIspersion of Toxic Industrial Chemicals in urban environments" (MODITIC). The scientific objective of this project is the systematic study of the release and transport of neutral and non-neutral chemicals in complex urban environments, to enhance understanding of the dominating physical processes involved, and to support improvements in modelling techniques. The participating organisations are:

- Direction Générale de l'Armement (DGA), DGA CBRN Defence, France
- Institut National de l'Environnement Industriel et des Risques (INERIS), France
- Norwegian Defence Research Establishment (FFI), Norway
- Swedish Defence Research Agency (FOI), Sweden
- University of Surrey (UoS), United Kingdom

FFI is the lead organisation. The project was initiated 1 September 2012 with the duration of three-and-a-half years. The project is funded by the Norwegian Ministry of Defence, the Swedish Ministry of Defence, the French Ministry of Defence, and the French Ministry of Ecology, Sustainability and Energy.

This report describes the work and results for WE5300 "LES computations, analysis, and reporting". Chapters 1–5 are authored by FFI, and Chapter 6 is authored by FOI. Each institute has conducted their own validation of the quality of their contribution.

1   Introduction

In recent years attention has been focused on release and aerial dispersion of toxic industrial chemicals (TIC), whether it is due to industrial accidents or terrorist activities, since it may threaten the lives and health of an urban population. In order to estimate the consequences and to identify most effective countermeasures to limit the impact, responsible authorities need to have reliable predictions of the spatial patterns as well as the time variations of the TIC concentrations. When considering non-neutral TIC, i.e. a denser-than-air or lighter-than-air gas, the dispersion process poses sever challenges especially in complex urban environments and is an important area of research.

The transport and dispersion of pollutants in the atmosphere are governed by the conservation laws of mass, momentum, and energy. Non-neutral gases will predominantly be transported with the wind field, but the transport may also be significantly affected by e.g. the density differences, heat exchange, and gravitational force. The density difference may severely alter the turbulence field due to the resulting stably or unstably stratified background. The impact of the stratification primarily modifies the vertical mixing process of the plume, and therefore also the overall transport process. A neutral gas, i.e. a gas with the same density as air, on the other hand will be transported with the wind field without affecting its dynamics. In both cases it is the wind field that is the most important dynamical process, and in order to model the dispersion successfully, it is crucial to accurately model the wind field.

In urban environments the dominating effects on the flow field are kinematic blocking of velocity components normal to solid surfaces and non-local pressure effects caused by reflections (cf. e.g. [1]). The kinematic blocking dominates the local flow conditions in built up areas, where buildings cause street canyon effects, flow separation and generation of unsteady wakes. In the atmospheric boundary layer, the non-local effects dominates and modify the turbulence anisotropy which in turn changes the dispersion process.

In the past two decades Computational Fluid Dynamics (CFD) has become a more popular tool for modelling dispersion. However, a number of modelling issues need to be addressed in order to warrant the use of CFD in urban areas [2]. Many urban dispersion studies are based on the assumption that the flow field is statistically steady and therefore the steady state Reynolds-Averaged Navier-Stokes (RANS) method is widely used (see e.g. [3, 4, 5, 6]). However, results show that even though the mean velocity field can be fairly well predicted using this method, the turbulence kinetic energy is in generally underpredicted, which may lead to a poorly predicted mixing process.

Several studies regarding numerical simulation of dense gas dispersion using the Unsteady RANS (URANS) approach have been carried out in the past [7, 8, 9, 10] with fairly good results. The URANS method inherently assumes that the mean flow field is statistically unsteady. This assumption is better suited for flows involving bluff body shedding, which occurs downstream building structures. Another approach that naturally includes the flow unsteadiness is Large Eddy Simulation (LES), which resolves the inherent unsteadiness of the large scale turbulence irrespectively of the nature of the averaged flow field. Previous studies using the LES approach for urban dispersion modelling of neutral gases have shown good results [11, 12, 13, 14].

This report describes the work conducted using the LES approach to simulate release and dispersion of neutral and dense gas in geometries with increasing complexity - from a simple hill configuration

to a scale model of an actual urban area comprising a part of Paris. The purpose of the study is to improve the methodology for high fidelity dispersion models and validate the results to wind tunnel data.

2 Scenario description

A more detailed description of the various scenarios is found in [15] and [16]. The scenarios are designed with increased complexity to investigate how the dispersion of dense and neutrally buoyant gases interact with an increasingly more complex wind field. It is also of interest to explore different numerical models as to how well they manage to predict the dispersion and wind field. The scenarios are using the same incoming wind field, see Table 2.1. Carbon dioxide is used as dense gas, and has a density of approximately 1.5 times the density of air.

Parameter	Description	Value
Q	Emission rate	50/100 dm^3/min
d	Source diameter	0.103 m
U_{ref}	Reference velocity at $H = 1$ m	1 m/s
H	Boundary layer height	1 m
U^*/U_{ref}	Friction velocity	0.055

Table 2.1 *Parameters describing the incoming wind field and dissemination.*

2.1 Two dimensional hill

This scenario features a large smooth hill that covers most of the spanwise length of the wind tunnel. As shown in Figure 2.1, the hill is homogeneous in the spanwise direction. The sources are positioned both on the upstream and downstream side of the crest. This geometry creates an adverse pressure gradient on the upstream side of the crest, and a favorable pressure gradient on the downstream side of the crest. The emission rate of both the neutral and dense gas is 100 dm^3/min.

2.2 Backward-facing step

In order to investigate the two-way coupling between a dense gas and a wind field affected by recirculation, the upstream part from the hill scenario is used to create a backward-facing step (see Figure 2.2). In order to get a high enough aspect ratio of the recirculation to provide two-dimensional conditions, the floor behind the back-step was lifted. This yielded a back-step height of 0.1 m. The source is located in the recirculation region, just behind the step, with an emission rate of 100 dm^3/min.

2.3 Backward-facing step with cubes

To include separation effects, as well as recirculation, rows of cubes were placed behind the backward-facing step. Two different placements of the arrays are tested (see Figures 2.3 and 2.4). In
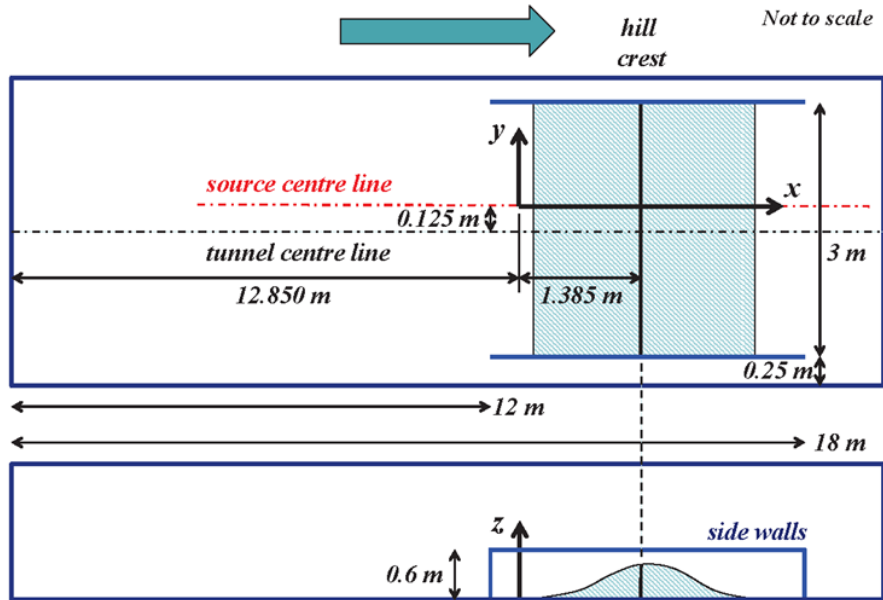
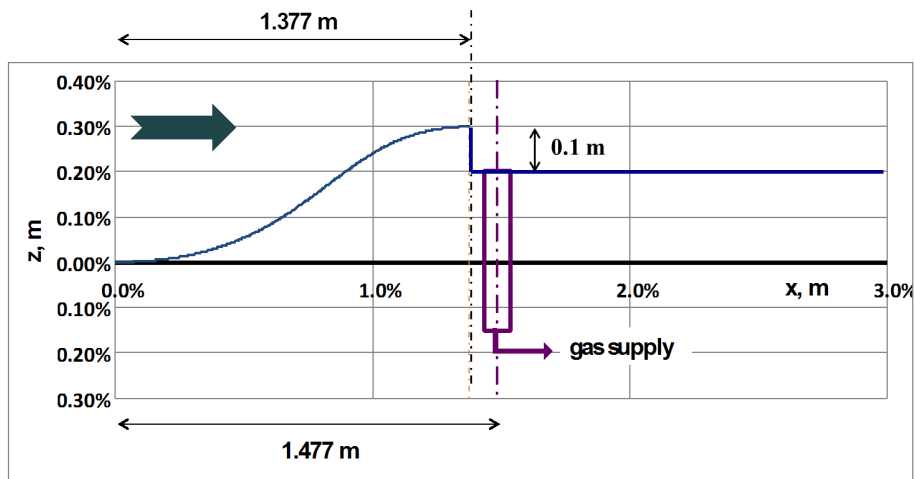*Figure 2.1 Schematic picture of the hill scenario.*

Figure 2.2 Schematic picture of the back-step.

array 1 the cubes are located outside of the recirculation region whereas they in array 2 are placed in the recirculation zone. In both cases the source is located behind the back-step and releases 100 dm^3/min.

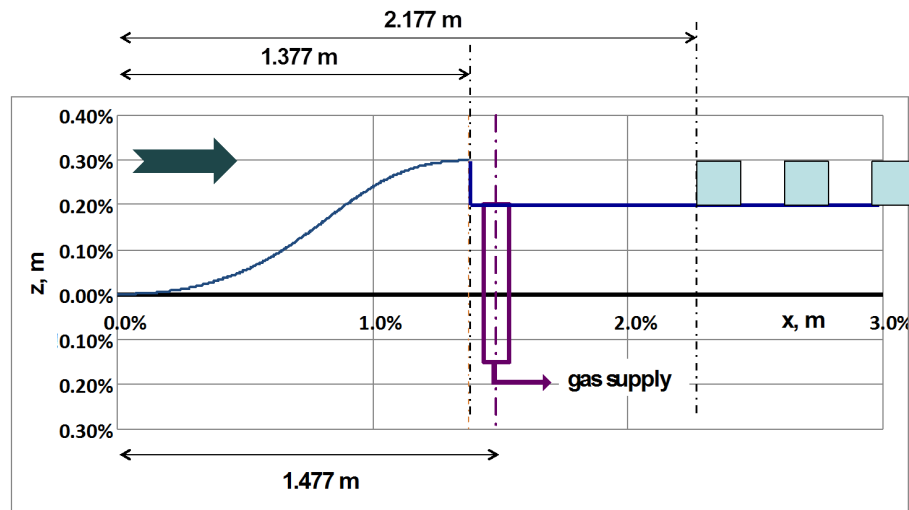**Figure 2.3** *Schematic picture of Back-step with cubes. Array 1.*
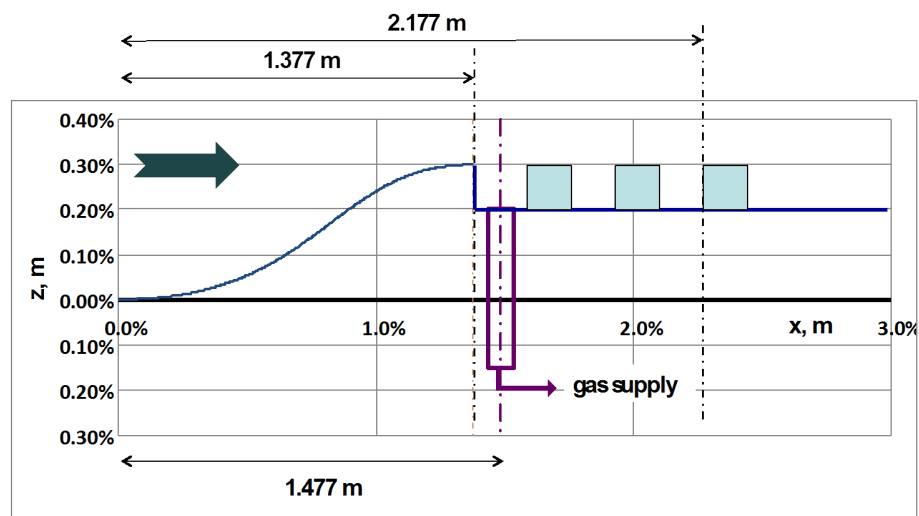

Figure 2.4 *Schematic picture of Back-step with cubes. Array 2.*

2.4   Simple array

Four cubes are used to represent a simple urban street canyon with vortex shedding, separation, and recirculation. Three sources are placed upstream as seen in Figure 2.5. A separate study is also conducted where the four blocks are rotated 45 degrees. The cube height is 0.110 m, and the emission rate is 50 dm^3/min.

Figure 2.5 *Schematic picture of Simple array.*
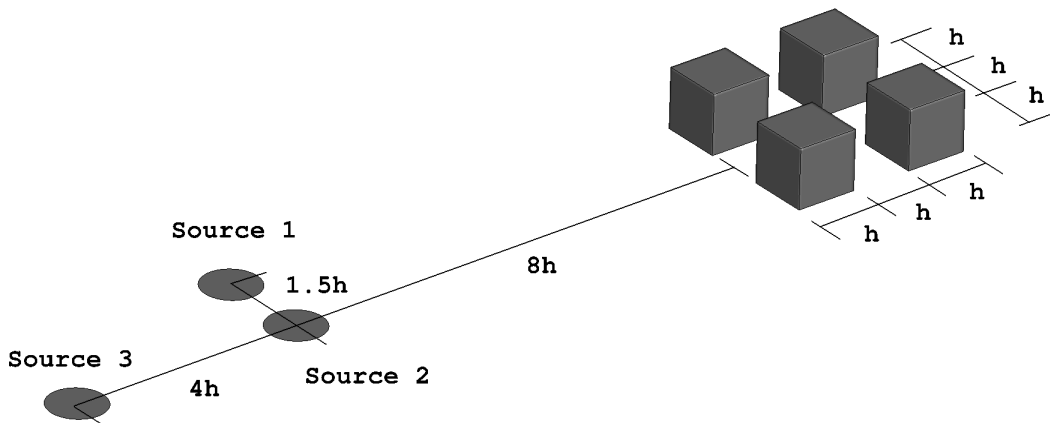
2.5   Complex array

The complex array (see Figure 2.6) model buildings with four different shapes with trees placed in some of the streets. Three source position are used and two different wind directions. The emission rate is 50 dm^3/min.
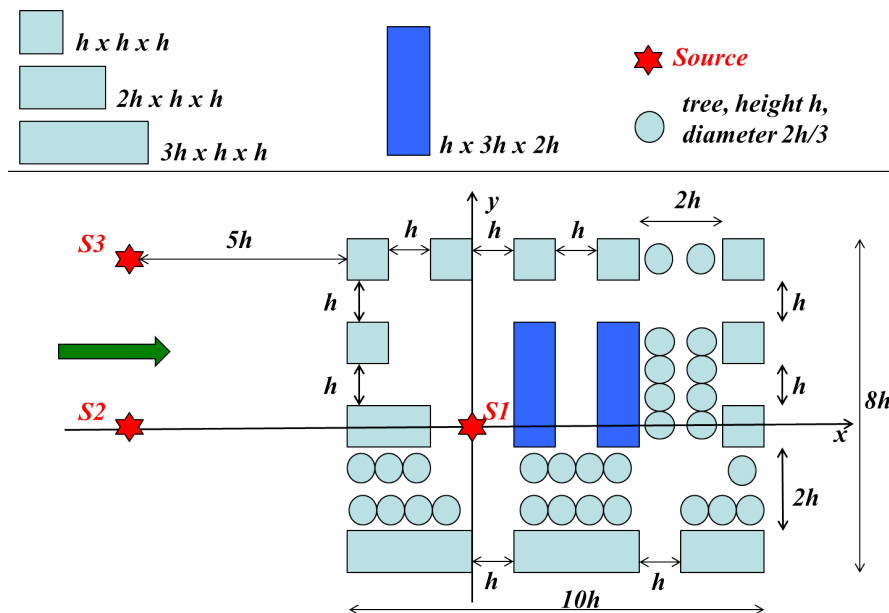

Figure 2.6 *Schematic picture of the complex array. Sources are marked by red stars and trees with light blue circles.*

2.6 Paris

A section of Paris is used to represent a large urban area. The model scale is 350 times smaller than full-scale with an averaged building height of 0.077 m. Irregular avenues and buildings create an environment that produces a very complex wind field. Three different source locations have been investigated as seen in Figure 2.7. The emission rate is 50 dm^3/min. More information about the different Paris cases is found in Table 2.2.

Figure 2.7 *Schematic picture of Paris*
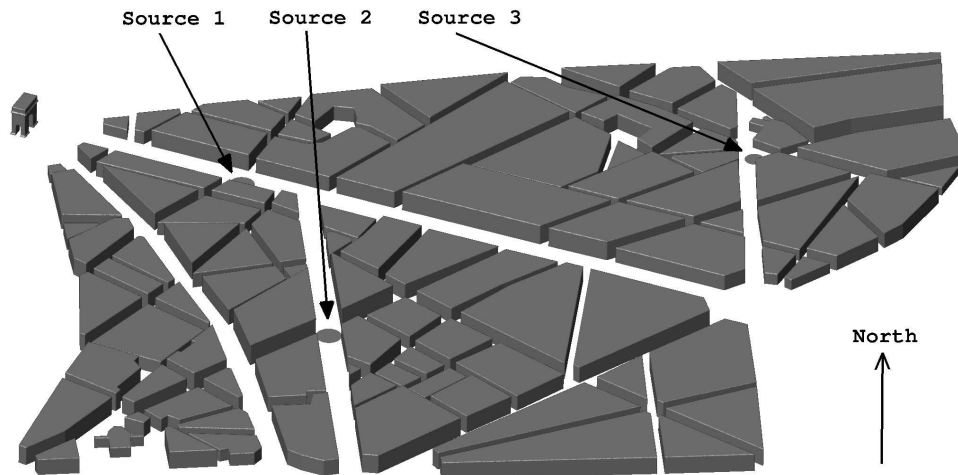
Source number	Wind direction	Source diameter
1	300°	0.1143 [m]
2	220°	0.1143 [m]
3	40°	0.0857 [m]

Table 2.2 *Parameters describing the incoming wind field and dissemination.*

3 Wind tunnel experiment

The wind tunnel experiments are conducted in the meteorological wind tunnel at the Environmental Flow Research Center (EnFlo). The center is located at the University of Surrey. The tunnel has a working section of $20 \times 3.5 \times 1.5$ [m] with a overall length of 27 meters. See [16] for a more detailed description regarding the wind tunnel experiments.

Figure 3.1 *The Paris model inside the meteorological wind tunnel at the University of Surrey.*

4   Mathematical modelling

The filtered equations governing the conservation of mass and momentum for a Newtonian fluid with variable density are given by

$$\partial_t(\bar{\rho}) + \partial_j(\bar{\rho}\tilde{u}_j) = 0, \tag{4.1}$$

$$\partial_t(\bar{\rho}\tilde{u}_i) + \partial_j(\bar{\rho}\tilde{u}_i\tilde{u}_j) = -\partial_i\bar{p} + \partial_j(2\bar{\mu}\tilde{s}_{ij}) + \bar{\rho}g_i - \partial_j\tau_{ij}. \tag{4.2}$$

Here, the filtering operation is denoted by $(\bar{\cdot})$ whereas $(\tilde{\cdot})$ represents Favre (density-weighted) filtering. Temporal and spatial gradients are denoted $\partial_t = \partial/\partial t$ and $\partial_i = \partial/\partial x_i = (\partial/\partial x, \partial/\partial y, \partial/\partial z)$, respectively. $\tilde{u}_i = (\tilde{u}, \tilde{v}, \tilde{w})$, $\bar{p}$, and $\bar{\mu}$ are the resolved velocity field, pressure field, and dynamic viscosity, respectively, and $g_i = (0, 0, -g)$ is the gravitational acceleration. $\tilde{s}_{ij}$ denotes the resolved strain-rate tensor given by

$$\tilde{s}_{ij} = \frac{1}{2}(\partial_j\tilde{u}_i + \partial_i\tilde{u}_j) - \frac{1}{3}\delta_{ij}\partial_k\tilde{u}_k. \tag{4.3}$$

It should be notet that $\tilde{s}_{ij}$ is divergence free. The last term in (4.2) is the residual stress tensor, $\tau_{ij} = \bar{\rho}(\widetilde{u_iu_j} - \tilde{u}_i\tilde{u}_j)$, which needs to be modelled.

5　Work conducted by FFI Norway

This chapter is authored by FFI who is also responsible for the quality validation.

5.1　Objectives

The objectives of this study are to

- Provide detailed description of set-up and modelling of dense and neutral gas
- Evaluate methodology used for urban dispersion modelling
- Address important findings regarding dispersion in urban-like geometries

5.2　Mathematical modeling

5.2.1　Turbulence modeling

The residual stress tensor, $\tau_{ij} = \bar{\rho}(\widetilde{u_i u_j} - \tilde{u}_i \tilde{u}_j)$, is modelled using the dynamic Smagorinsky sub-grid viscosity approach, i.e. $\tau_{ij} = -2\mu_t \tilde{s}_{ij}$, where μ_t is the eddy viscosity calculated through a dynamic procedure based on the the resolved velocity field. The density is defined as:

$$\bar{\rho}(\tilde{m}) = \frac{1}{\tilde{m}\rho_{gas}^{-1} + (1 - \tilde{m})\rho_{air}^{-1}}, \tag{5.1}$$

where m is the mass fraction.

5.2.2　Dispersion modelling

The filtered equation governing the transport of mass fraction of a scalar field is given by

$$\partial_t(\bar{\rho}\tilde{m}) + \partial_j(\bar{\rho}\tilde{m}\tilde{u}_j) = \partial_j\left(\bar{\rho}\alpha\partial_j\tilde{m}\right) - \partial_j t_j, \tag{5.2}$$

where α is the scalar molecular diffusion coefficient, and $t_j = \bar{\rho}(\widetilde{u_j m} - \tilde{u}_j\tilde{m})$ represents the unresolved sub-grid scalar flux which is modelled similarly to the momentum sub-grid stresses, i.e. $t_j = -(\mu_t/Sc_t)\partial_j\tilde{m}$, where the turbulent Schmidt number is set to $Sc_t = 0.9$.

5.3　Meshing procedure

The co-ordinate system used is oriented with the x, y, z-axes aligned with the streamwise, spanwise and wall-normal directions, respectively. The size of the computational domains used is not exactly the same as the wind tunnel. For example, the length of the computational domain is shorter than the wind tunnel since the already developed turbulent boundary layer is provided at inflow.

To sustain the turbulent boundary layer upstream, the grid size is $\Delta z^+ \leq 30$ in the wall-normal direction close to the ground. The viscous length scale is estimated using the friction velocity which in turn is estimated from wind tunnel measurements.

5.3.1   Hill

The computational domain used in the hill case is $x \in [0, 10]$ m, $y \in [-1.5, 1.5]$ m, $z \in [0, 1.5]$ m. The computational mesh uses hexagonal cells, and the cell-sizes in the various areas are listed in Table 5.1.

	Δx^+	Δy^+	Δz^+
Around sources	54	54	18-223
Elsewhere	73 - 344	44 - 128	18 223

Table 5.1   Computational grid size used for the hill simulations.

5.3.2   Simple array

The computational domain used in the simple array case is $x \in [-0.3955, 4.5645]$ m, $y \in [-1.75, 1.75]$ m, $z \in [0.0, 1.5]$ m. The placement of the buildings is seen in Figure 2.5 with source 2 placed at $(0, 0, 0)$. The mesh has a hexahedral structure, divided into 3 regions defined in Table 5.2.

	x [m]	y [m]	z [m]	Δx^+	Δy^+	Δz^+
Source (surface)				6.3	6.3	
Region 1	$[-0.3955, 1.7245]$	$[-0.33, 0.33]$	$[0.00, 0.23]$	13	13	$4.0 - 13$
Region 2	$[-0.3955, 2.4145]$	$[-1.10, 1.10]$	$[0.00, 0.57]$	61	61	$20 - 61$
Region 3	$[-0.3955, 4.5645]$	$[-1.75, 1.75]$	$[0.00, 1.50]$	185	185	$60 - 185$

Table 5.2   Computational grid size used for the simple array simulations.

5.3.3   Paris

The computational domain for the Paris case is $x \in [-1.176, 3.644]$ m, $y \in [-3.0429, 2.8171]$ m, $z \in [0.0, 1.5]$ m with source 1 placed at $(0, 0, 0)$. The wind direction of 300 degrees is aligned with the x-axis. The mesh has a tetrahedral structure.

	x [m]	y [m]	z [m]	Δx^+	Δy^+	Δz^+
all surfaces				20	20	
Region 1	$[-1.176, 3.324]$	$[-2.6229, 2.4271]$	$[0, 0.3]$	$20 - 98$	$20 - 98$	$20 - 98$
Region 2	$[-1.176, 3.644]$	$[-3.0429, 2.8171]$	$[0, 1.5]$	196	196	196

Table 5.3   Computational grid size used for the Paris simulations.

5.4   Boundary condition

The boundary layer developing on the top and side surfaces are much thinner, compared to the height of the boundary layer developing on the ground. Therefore, slip condition (see Table 5.4) are used on these surfaces for the simple array and Paris case. Due to the pressure effects introduced by the geometry of the hill, no-slip condition is used on the top surface in the hill case.

	Hill	**Simple array**	**Paris**
Source	$u_i = (0, 0, w_s)$	$u_i = (0, 0, w_s)$	$u_i = (0, 0, w_s)$
Buildings	-	no-slip	no-slip
Ground	no-slip	no-slip	no-slip
Side walls	slip	slip	slip
Top	no-slip	slip	slip
Inflow	u_i	u_i	u_i
Outflow	$\partial_n u_i = 0$	$\partial_n u_i = 0$	$\partial_n u_i = 0$

Table 5.4   *Velocity boundary conditions for the different cases simulated. w_s is the vertical velocity at the source and ∂_n is the normal derivative.*

Defining $m = 1$ at the source boundary gives a pure carbon dioxide emission. The emission is controlled by defining the mass fraction and the vertical velocity, w_s. The inflow boundary condition for the scalar field is 0, the outflow is $\partial_n m = 0$, and the remaining surfaced uses a zero-flux condition.

5.4.1   Inflow

The wind tunnel is using roughness elements placed on the floor to generate a specific turbulent boundary layer. The same technique is adopted for the numerical simulations (see Figure 5.1). The turbulent boundary layer is simulated separately with a computational domain ($7 \times 1.44 \times 1.5$ meters) with 22 rows of roughness elements, placed staggered with a distance of 0.12 m apart, in the streamwise direction. The elements are placed 0.24 m apart, in the spanwise direction with the dimensions $(x, y, z) = (0.002, 0.08.0.02)$ meters.

Synthetic turbulence is used to add fluctuations to the average streamwise velocity which is used as the inflow boundary condition [17]. The spatial and temporal scales used for the synthetic turbulence are taken from wind tunnel measurements [16]. All other surfaces have the same boundary conditions as the simple array, except the spanwise boundary conditions which is periodic. A plane, located behind the last row of roughness elements, containing the instantaneous velocity field is stored for 29.6 seconds with $\Delta t = 0.0016$. Using a linear interpolation in time and space, this plane is used as an inflow boundary condition (see Figure 5.1), for all cases except the hill. In the hill simulations, inflow condition is generated using the same technique but without roughness elements and time interpolation.
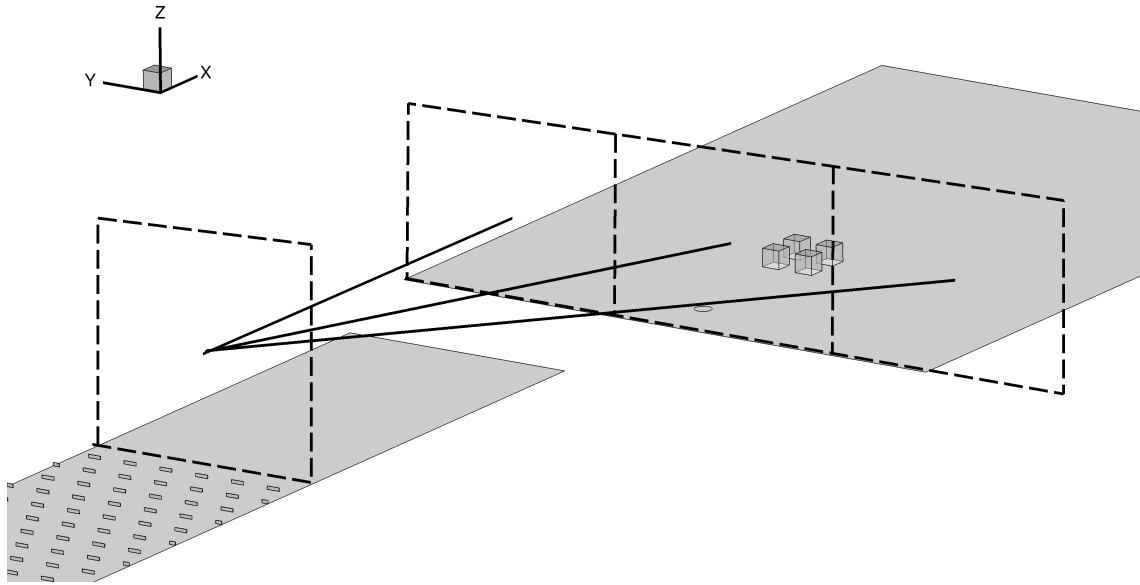
Figure 5.1 *The stored instantaneous flow field used as an inflow boundary condition.*

5.5   Calculation set-up and control

The gas is released when a satisfactory boundary layer has developed corresponding to the wind tunnel boundary layer. The statistics are gathered when the mass flux for the outflow boundary correspond to the mass flux for the source boundary. The time step is either fixed, as in the hill case, or controlled by specifying the Courant–Friedrichs–Lewy (CFL= $U\Delta t/\Delta x$) number, as in the simple array and Paris case. The number of computer nodes are 16 or 20-core processors with 64 or 128 GB of memory, respectively. Using 80 (20×4) processor cores on a computational grid of 9 500 000 nodes give a computational time of $\approx 12\ s/\Delta t$.

The software used is developed by *Cascade technologies* [18]. The solver used is *vida*, which is a high-fidelity, low-Mach, variable density solver based on Large Eddy Simulation methodology.

Scenario	Source	Release	start [s]	Statistics start/stop [s]	avg time [s]	CFL	Δt avg [s]
Hill	Upwind	Neutral	–	–/–	19	-	0.0005
	Upwind	Dense	–	–/–	11.8	-	0.0005
	Downwind	Neutral	–	–/–	12.5	-	0.0005
	Downwind	Dense	–	–/–	22	-	0.0005
Simple array	2	Neutral	19.5	50.9/79.9	29	0.9	0.0005
	2	Dense	19.5	38.5/114.2	75.7	0.7	0.0003
Paris	1	Neutral	19.4	29/90.9	61.9	0.9	0.0005
	1	Dense	19.4	43.9/104.7	60.8	0.7	0.0003

Table 5.5 *Simulation control parameters*

5.6 Results

Reynolds decomposition is used defining an arbitrary quantity as $\tilde{a} = A + a$, where $\tilde{a}$ is the instantaneous quantity, A is the averaged, and a is the fluctuating part. Besides comparing statistics from the simulations to experimantal values, an MOE2 (Measure Of Efficiency) method is used. This method is based on experimental and numerical profiles. Using the same measurement position in the experiment and the simulation the MOE2 is defined as

$$MOE2 = \left(\frac{A_u}{A_{Exp}}, \frac{A_u}{A_{CFD}} \right),$$
(5.3)

where A_{CFD} is the area under the profile obtained with numerical simulation, A_{Exp} is the area under the profile obtained with experiments, and A_u is the union. These two numbers approaches 1 when the experimental and numerical results are the same. If the LES results overpredicts the entire experimental profile the MOE2 values are $(1, < 1)$.

The mass fraction m is used to calculate the concentration, c, defined as

$$c = \frac{\rho m}{\rho_{gas}},$$
(5.4)

where ρ_{gas} is the density of the released gas and ρ is the local (mixed) density.

5.6.1 The turbulent boundary layer

As mentioned in section 5.4.1, the turbulent boundary layer is generated by specifying the inflow so that it corresponds to the wind tunnel boundary layer. In Figure 5.2 the spanwise averaged turbulence kinetic energy is shown. Even if the correct Reynolds stresses and turbulence kinetic energy are obtained on the inflow boundary, the total energy is reduced within the domain due to adaptation to the new geometry. The use of roughness elements downstream increases the production of turbulence kinetic energy and the results correspond well with experiments after insertion into the simple array scenario (see Figure 5.4 and 5.3). Without roughness elements, the boundary layer would only depend on viscosity to transfer the energy to higher regions, which reduces the turbulence kinetic energy in those regions (see Figure 5.5).

The domain width of the precursor simulation generating the turbulent boundary layer is 1.44 m, which may limit the large flow structures. However, due to the good experimental agreement, where both a time and spanwise average are used, it seems that the width is sufficient to capture the important dynamics in the lower part of the boundary layer. The turbulent integral time scale derived from experiments in [16] depends on height and direction, with a maximum not exceeding 1 s. This means the inflow boundary cycle of 29.2 s is acceptable and the non-zero spanwise average, seen in Figure 5.32a, probably is influenced by the roughness elements. Hence, a theoretical flat plate boundary layer is unable to develop.

Figure 5.3 shows the time and spanwise averaged streamwise velocity from the simple array simulation. The friction velocity is defined as $U^* = \sqrt{\nu \frac{\partial U}{\partial z}}|_{z=0}$ and the viscous length scale as
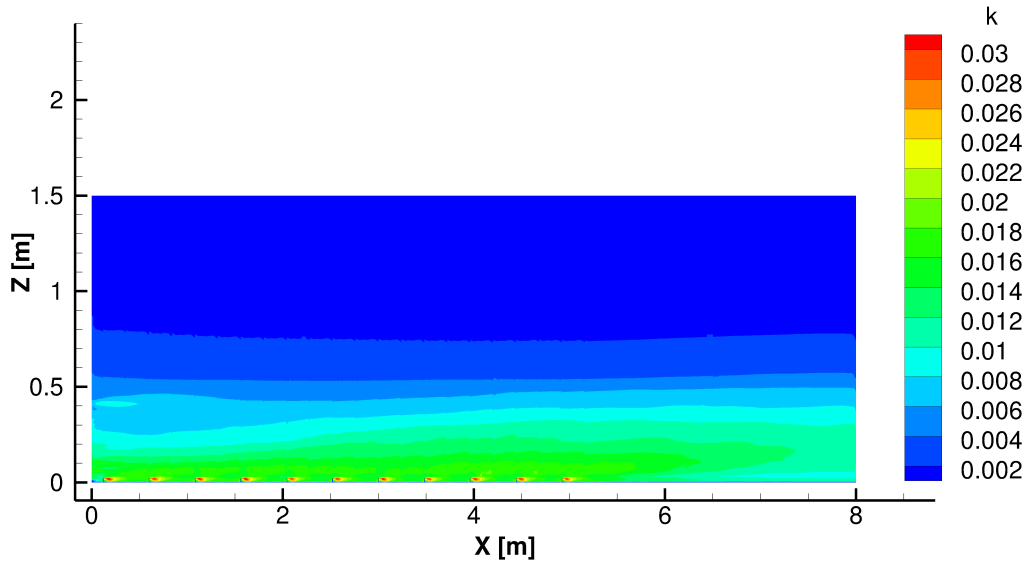
Figure 5.2 *The spanwise averaged turbulence kinetic energy k. The main flow direction is from left to right.*

$l = \nu/u^*$. The agreement compared to the experimental results are very good, with a visible log-layer above $z^+ = 100$ ($z = 0.044$ m). The turbulent boundary layer is triggered by roughness elements with a height of $z^+ = 45$ (z = 0.02 m), which is the same as the lowest experimental measurement position.

The relation $U_* = \sqrt{-\overline{uw}}$ is used to estimate the friction velocity in the wind tunnel, on the lower 20 % of the boundary layer. Using the same relation for the LES data, the scaled friction velocity is $U_*/U_{ref} = 0.0536$. A good agreement compared to the experimental value of $U_*/U_{ref} = 0.055$. However, using the other definition mentioned above, the friction velocity from the LES simulation is $U^* = 0.0339$ m/s. As also mentioned in [19] this could mean that the viscous length scale is larger than previously estimated which could mean that the plus-values for the grid are finer than estimated in section 5.3.

5.6.2   Hill

The velocity components, the Reynolds stresses, and the concentration were measured along a number of lines in the vertical and horizontal directions at different streamwise positions. The measured lines are given in Tables 5.6 and 5.7. Statistics were sampled for the quantities U, W, C, $\overline{uu}$, $\overline{ww}$ for all lines. However, only a limited number of plots are shown here. For the simulations with release of dense gas, statistics were not taken for the volume fraction C, hence no concentration results from the dense gas cases will be presented.

The vertical and horizontal profiles of the mean streamwise velocities are shown in Figure 5.6 for the release of the neutral gas from the upwind source. It can be seen that there are deviations in the LES results when comparing to the experimental results. The difference is largest at the first streamwise location. This difference is most likely due to the inflow used in these simulations.
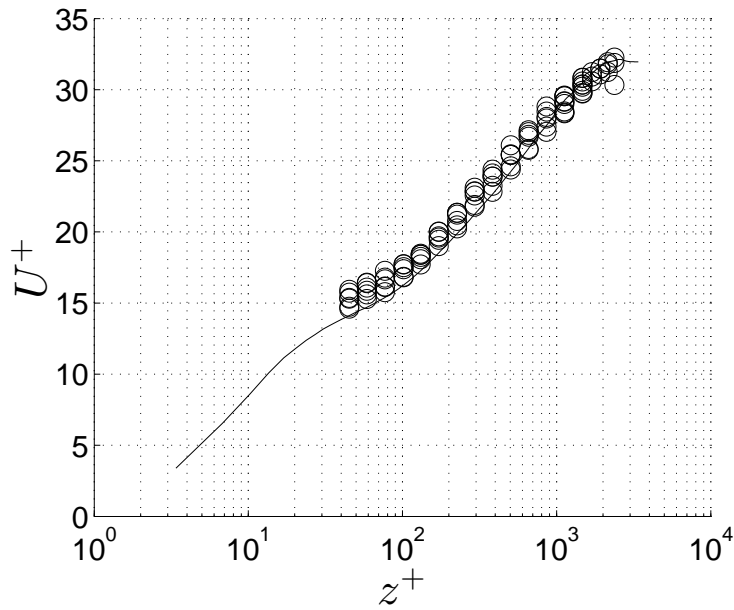
Figure 5.3 *Time averaged streamwise velocity profile at x = −0.2 m. The data is averaged in the spanwise direction. Experimental data (○) and LES data (——).*

Horizontal	x [m]	z [m]		Vertical	x [m]	y [m]
line 1	1.050	0.273		line 7	1.050	0
line 2	1.400	0.320		line 8	1.400	0
line 3	1.750	0.283		line 9	1.750	0
line 4	2.300	0.136		line 10	2.300	0
line 5	3.000	0.028		line 11	3.000	0
line 6	4.000	0.022		line 12	4.000	0
(a)				**(b)**		

Table 5.6 *Position of the measurement lines in the hill cases with release from the upwind source.*

Horizontal	x [m]	z [m]		Vertical	x [m]	y [m]
line 1	1.750	0.283		line 7	1.750	0
line 2	1.900	0.252		line 8	1.900	0
line 3	2.200	0.175		line 9	2.200	0
line 4	2.700	0.062		line 10	2.700	0
line 5	3.000	0.028		line 11	3.000	0
line 6	4.000	0.022		line 12	4.000	0
(a)				**(b)**		

Table 5.7 *Position of the measurement lines in the hill cases with release from the downwind source.*
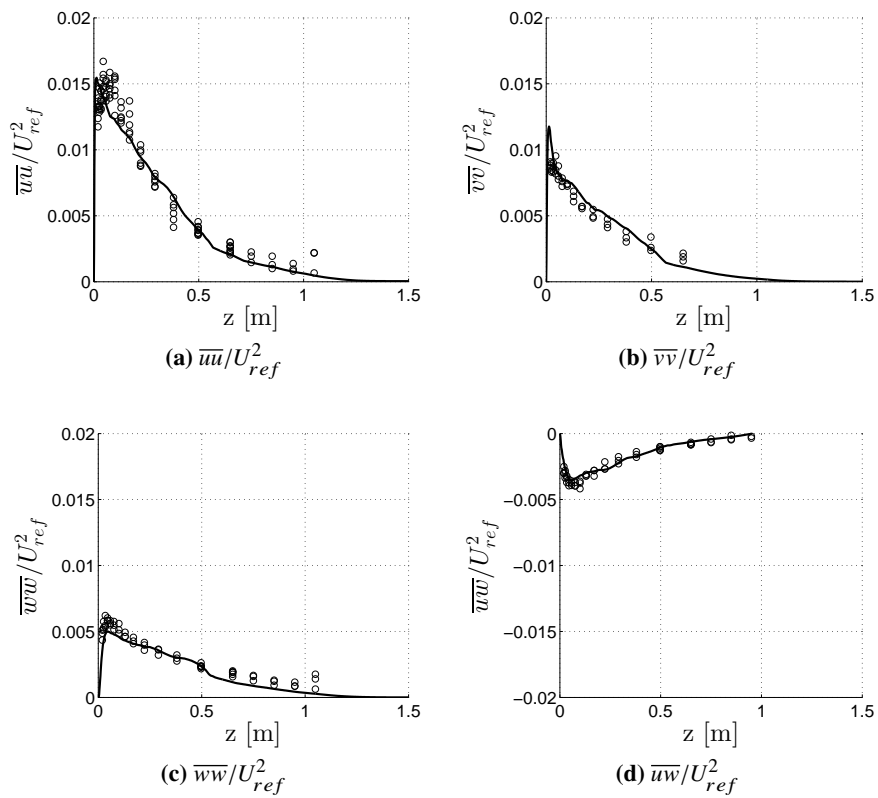
Figure 5.4 *Vertical profiles of normalized Reynolds stress components for experiment (○) and LES (——) at $x = -0.2$ m in the simple array using roughness elements.*
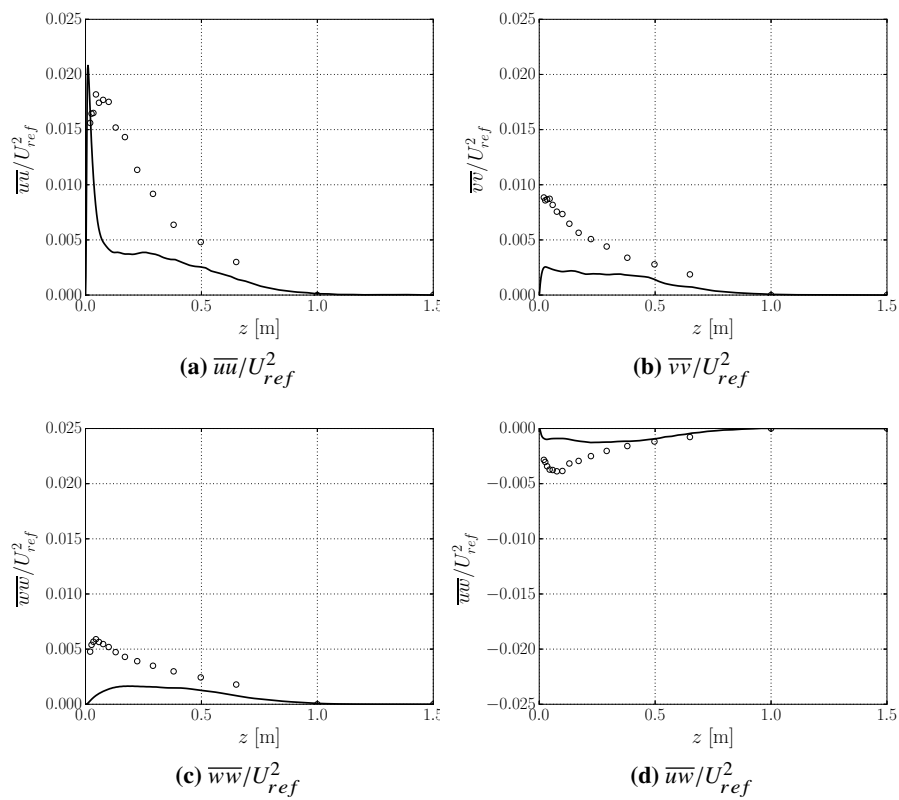
Figure 5.5 *Vertical profiles of normalized Reynolds stress components for experiment (○) and LES (——) at $x = -0.2$ m in the hill case without roughness elements.*
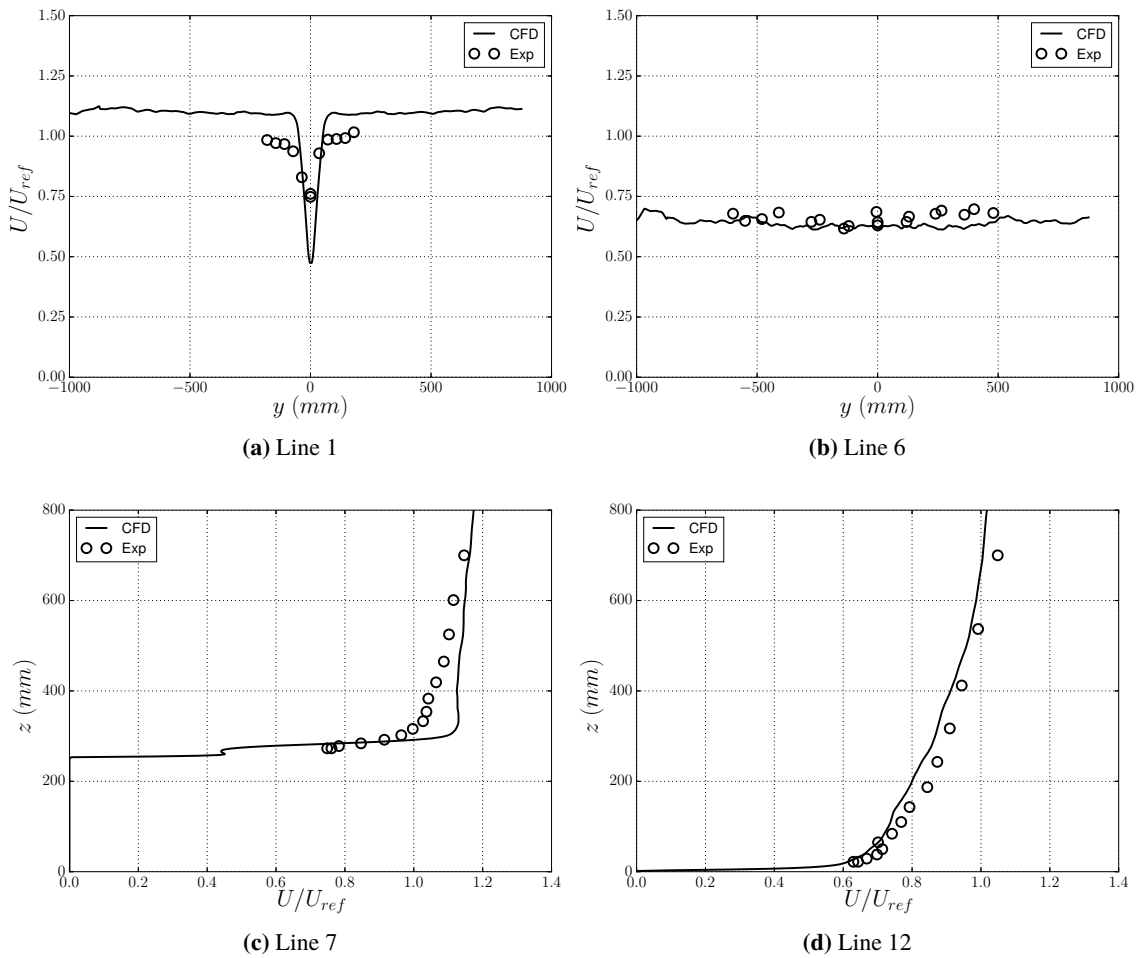
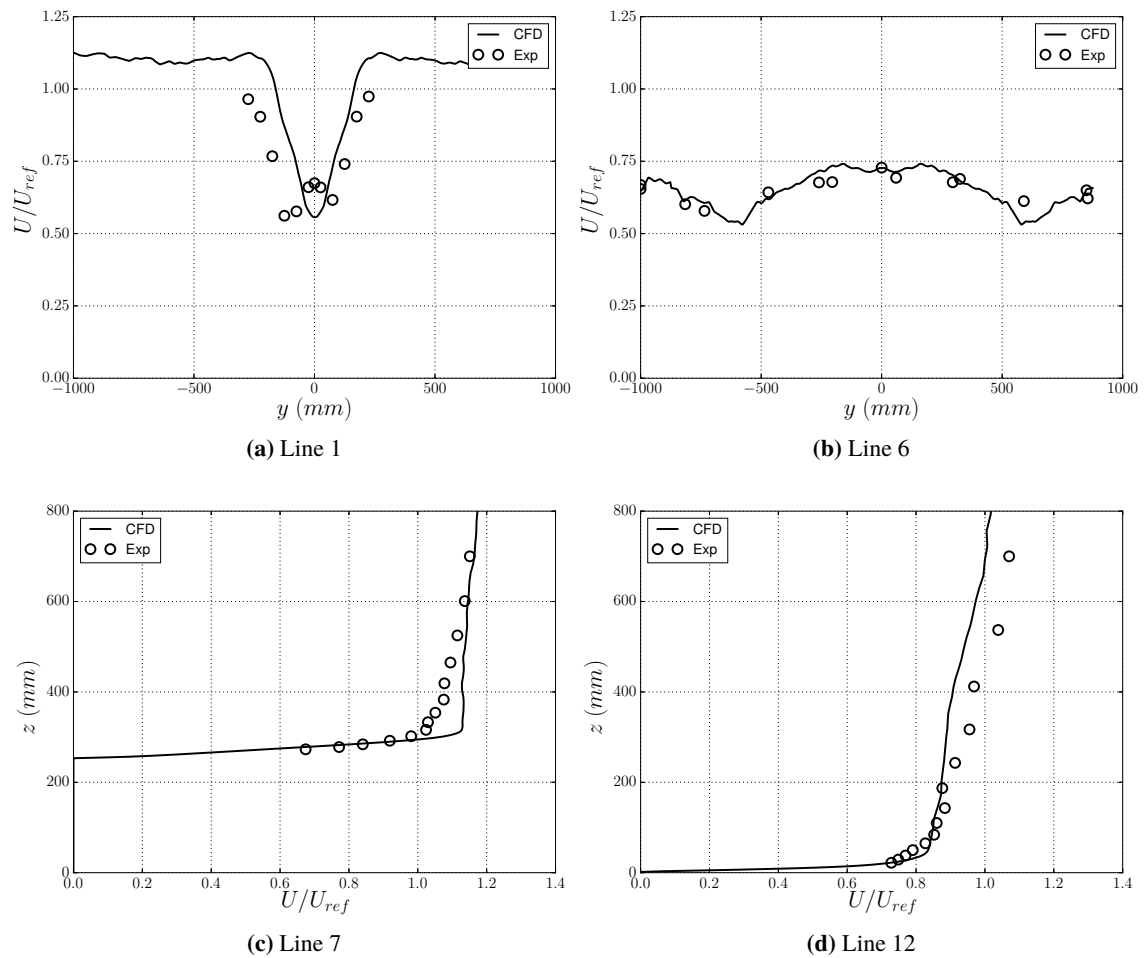**(a)** Line 1

(b) Line 6

(c) Line 7

(d) Line 12

Figure 5.6 *Mean streamwise velocity profiles for the release of neutral gas from the upwind source in the hill case at two streamwise positions.*
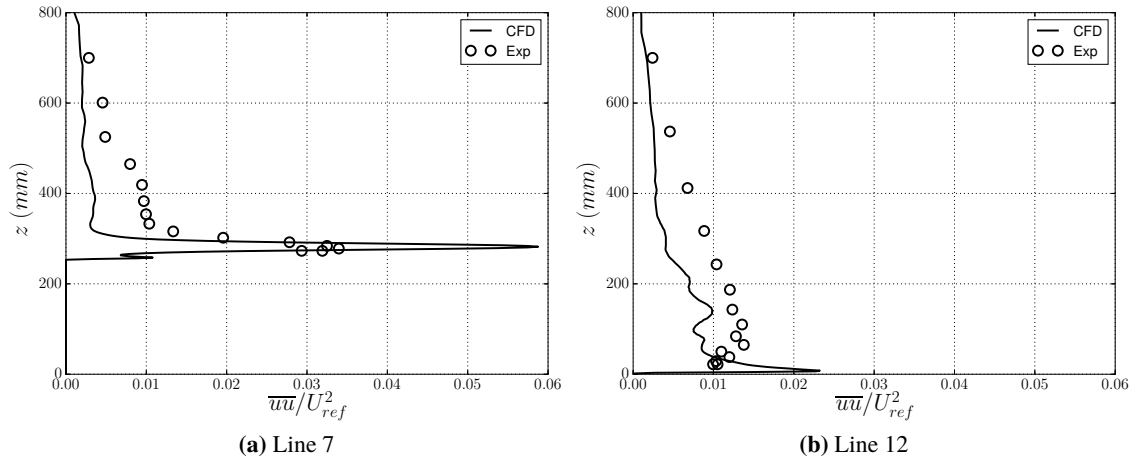
Figure 5.7 *Vertical profiles of $\overline{uu}/U^2_{ref}$ for the release of neutral gas from the upwind source in the hill case at two streamwise positions.*
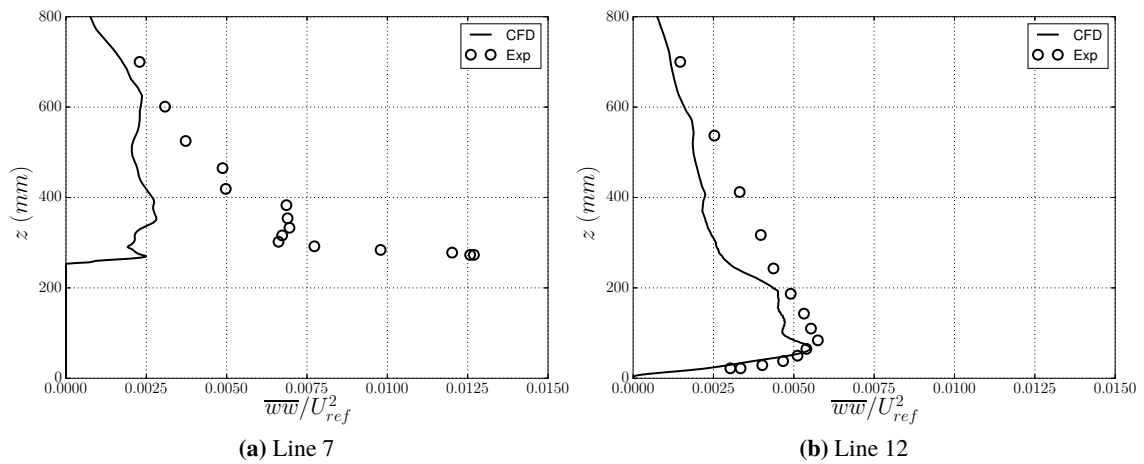
Figure 5.8 *Vertical profiles of $\overline{ww}/U^2_{ref}$ for the release of neutral gas from the upwind source in the hill case at two streamwise positions.*

Figure 5.7 shows the streamwise component of the Reynolds stress at $x = 1.050$ m and $x = 4.0$ m for the release of neutral gas from the upwind source in the hill case. Figure 5.8 shows the wall-normal component of the Reynolds stress. A similar result as in Figure 5.6 is seen. At the first measurement position (line 1 and line 7), the correspondence between the CFD results and the experimental results is not that good, but it improves at the last measurement position (line 6 and line 12). This is likely an effect of the adverse pressure gradient behind the crest of the hill, as inflow conditions likely become less and less important further downstream, and effects from the adverse pressure gradient becomes dominant.

(a) Line 1

(b) Line 6

(c) Line 7

(d) Line 12

Figure 5.9 *Mean streamwise velocity profiles for the release of dense gas from the upwind source in the hill case at two streamwise positions.*

Figures 5.9, 5.10, and 5.11 show the profiles of mean streamwise velocity, streamwise Reynolds stress component, and wall-normal Reynolds stress component respectively, at $x = 1.050$ m and $x = 4.0$ m for the release of dense gas from the upwind source. Again, the results agree more further downstream. From the Reynolds stress profiles it is seen that the release of dense gas significantly dampens the turbulent intensity close to the wall compared to the the case with release of neutral gas.
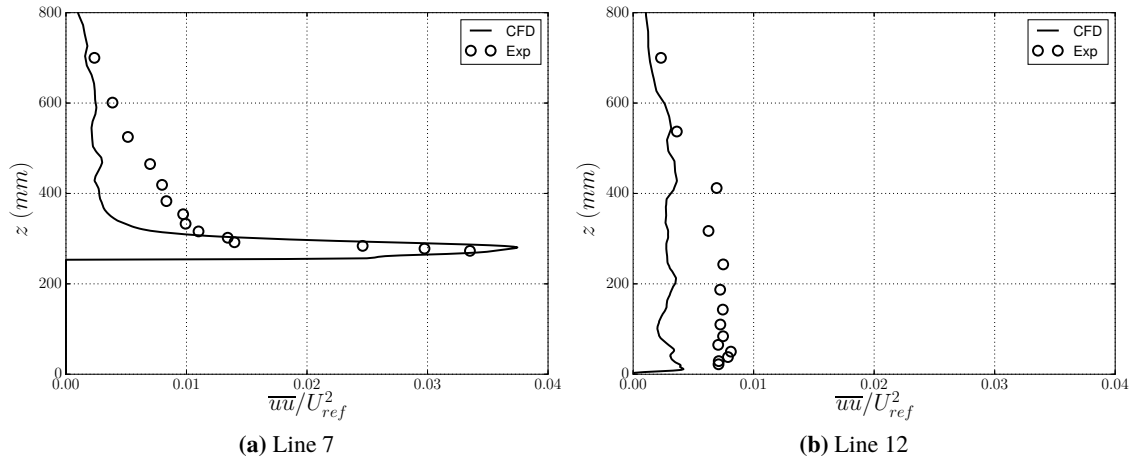
(a) Line 7   **(b)** Line 12

Figure 5.10   *Vertical profiles of $\overline{uu}/U_{ref}^2$ for the release of dense gas from the upwind source in the hill case at two streamwise positions.*
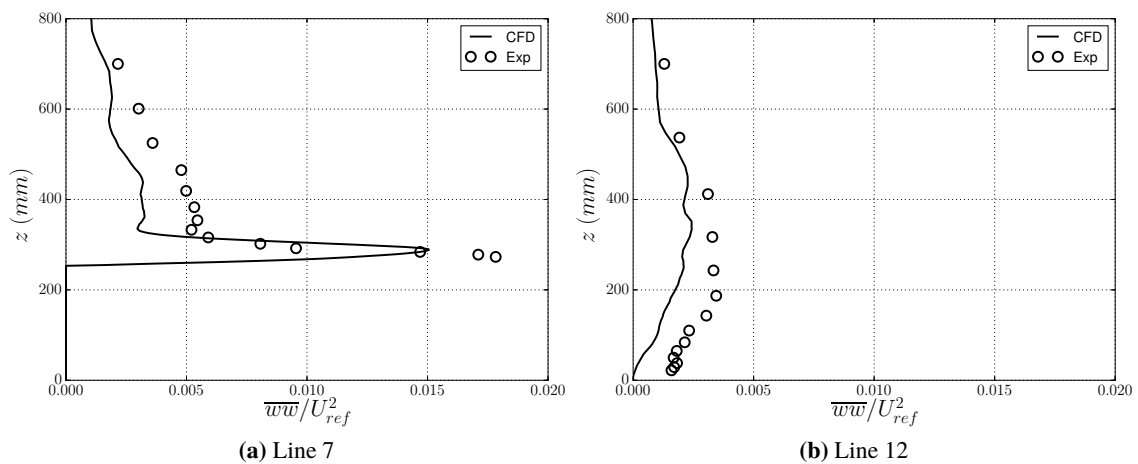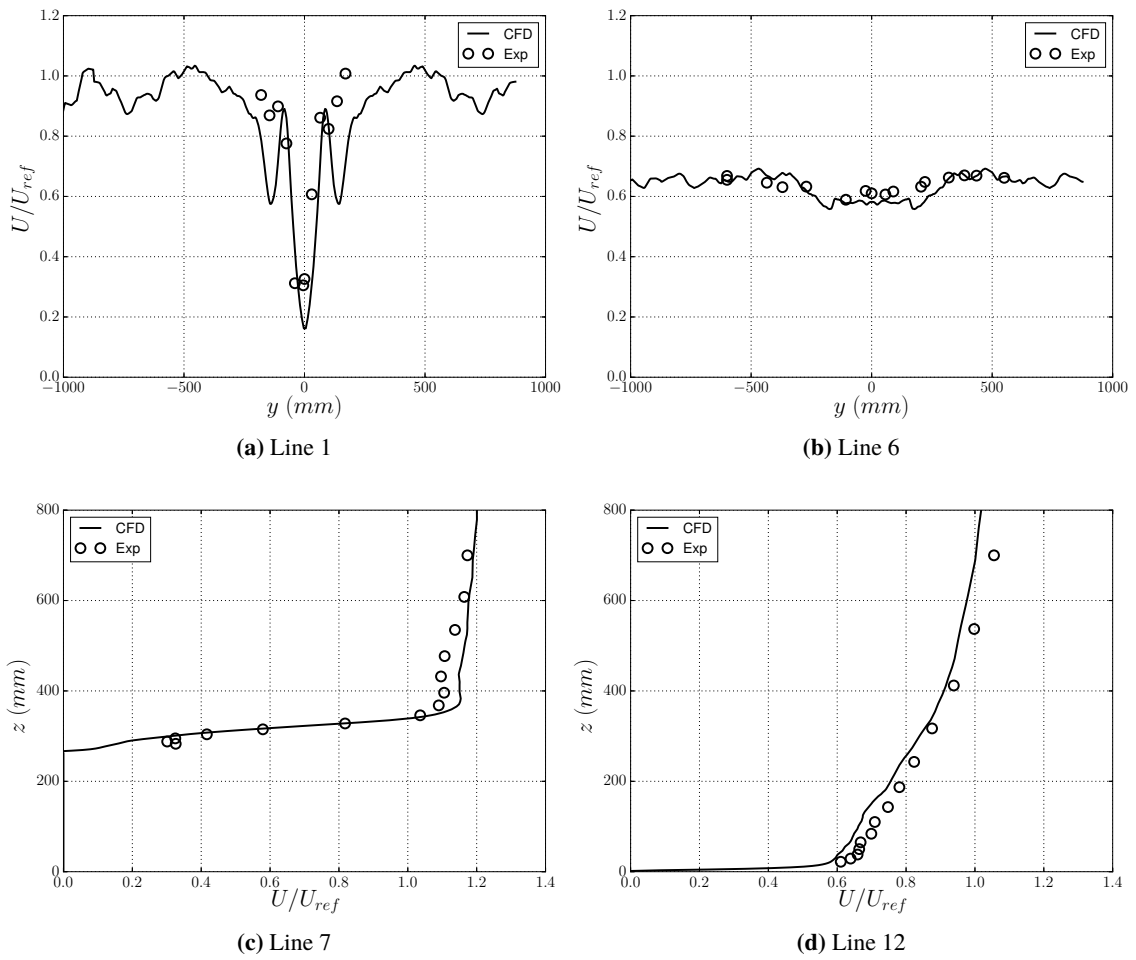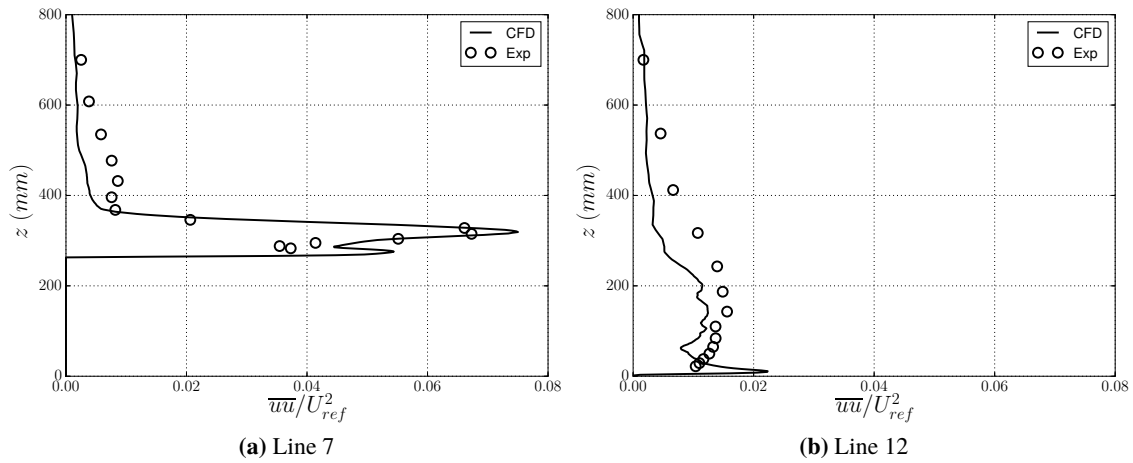

(a) Line 7   **(b)** Line 12

Figure 5.11   *Vertical profiles of $\overline{ww}/U_{ref}^2$ for the release of dense gas from the upwind source in the hill case at two streamwise positions.*

(a) Line 1

(b) Line 6

(c) Line 7

(d) Line 12

Figure 5.12 *Mean streamwise velocity profiles for the release of neutral gas from the downwind source in the hill case at two streamwise positions.*

(a) Line 7

(b) Line 12

Figure 5.13 *Vertical profiles of $\overline{uu}/U_{ref}^2$ for the release of neutral gas from the downwind source in the hill case at two streamwise positions.*
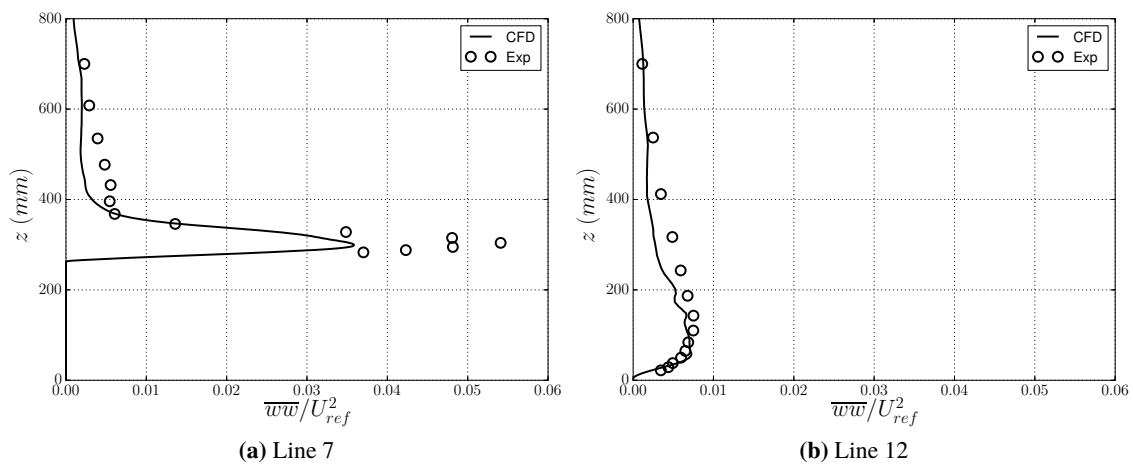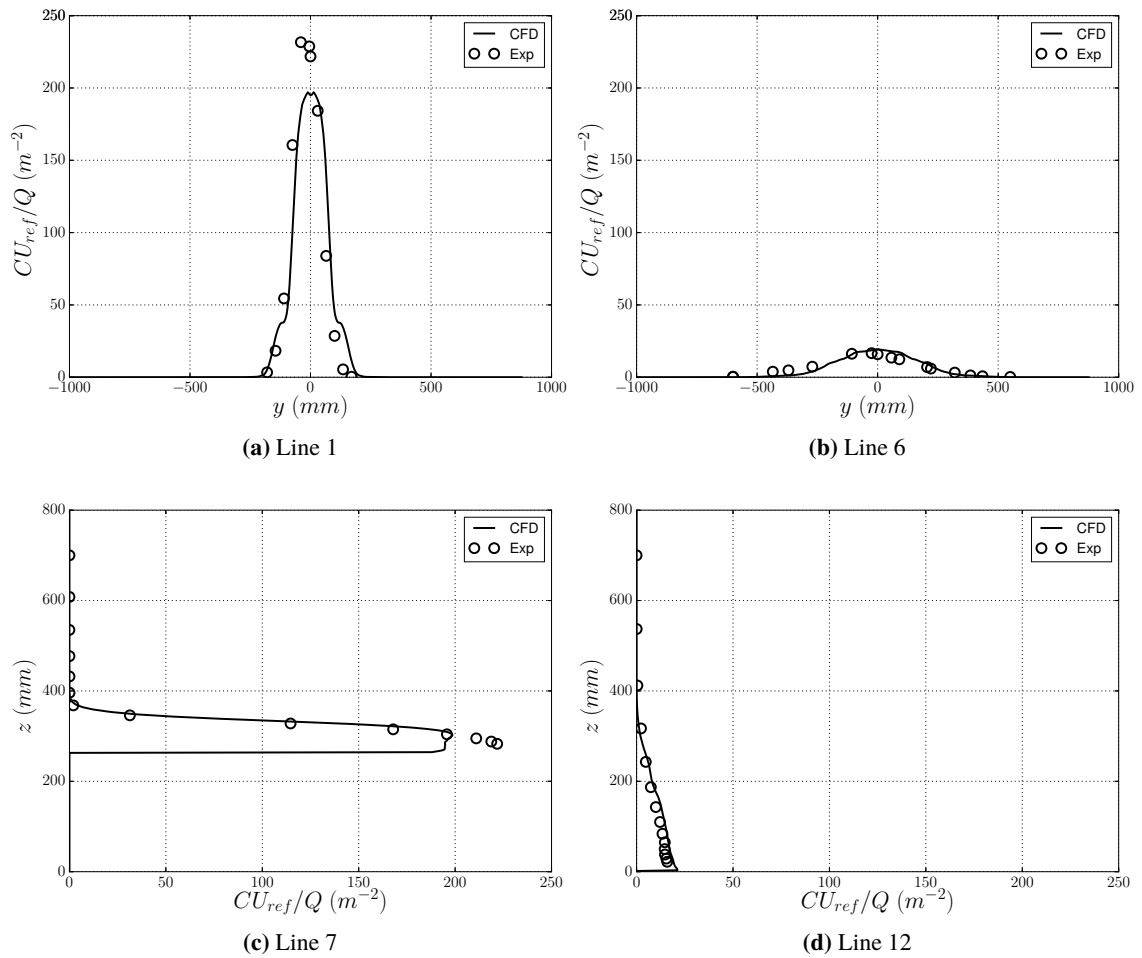

(a) Line 7

(b) Line 12

Figure 5.14 *Vertical profiles of $\overline{ww}/U_{ref}^2$ for the release of neutral gas from the downwind source in the hill case at two streamwise positions.*

(a) Line 1

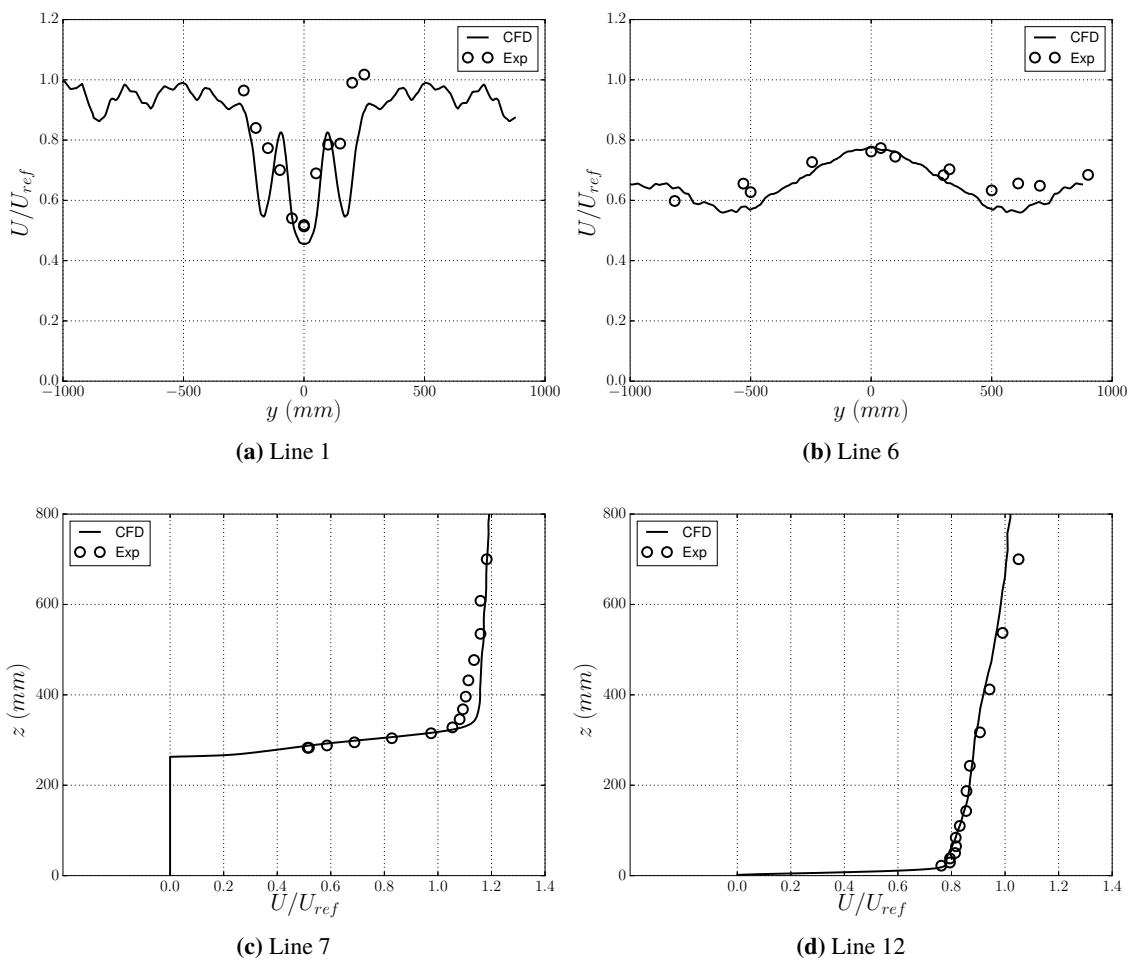**(b)** Line 6

(c) Line 7

(d) Line 12

Figure 5.15 *Mean concentration profiles for the release of neutral gas from the downwind source in the hill case at two streamwise positions.*

Figures 5.12, 5.13, 5.14, and 5.15 show the profiles of mean velocity, streamwise Reynolds stress, wall-normal Reynolds stress, and concentration respectively, at $x = 1.750$ m and $x = 4.0$ m with release of neutral gas from the downwind source. All the results from the CFD simulations are significantly closer to the experimental results than they were for the cases with release from the upwind source. This supports the idea that the adverse pressure gradient on the downstream side of the crest of the hill suppresses the effects of inflow conditions.

(a) Line 1

(b) Line 6

(c) Line 7

(d) Line 12

Figure 5.16 *Mean streamwise velocity profiles for the release of dense gas from the downwind source in the hill case at two streamwise positions.*

Figures 5.16, 5.17, and 5.18 show the profiles of mean velocity, streamwise Reynolds stress, and wall-normal Reynolds stress respectively, at $x = 1.750$ m and $x = 4.0$ m with release of dense gas from the downwind source. As can be seen in Figure 5.19, which shows this measure based on the concentration profiles, the results with release of neutral gas from the downwind source give significantly better results than with release from the upwind source, as observed above.
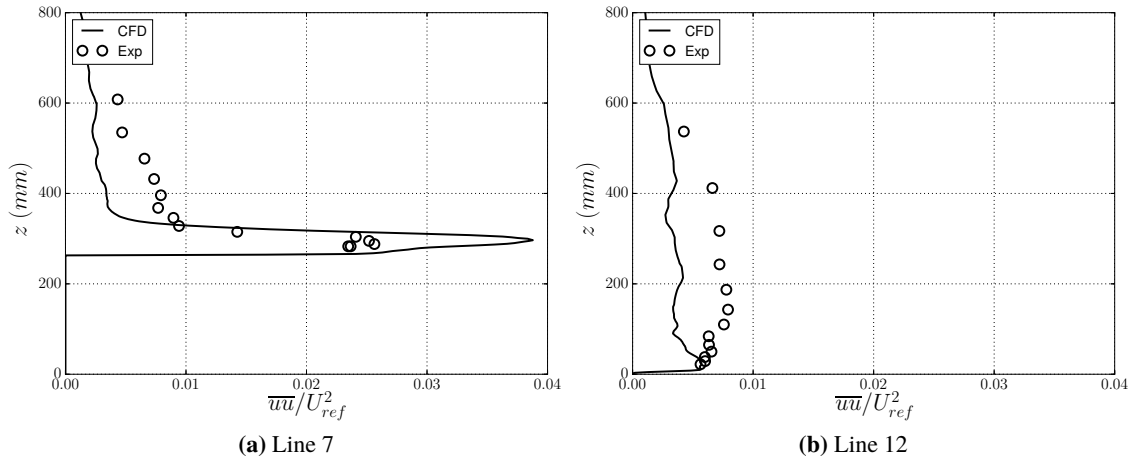
(a) Line 7

(b) Line 12

Figure 5.17 *Vertical profiles of $\overline{uu}/U_{ref}^2$ for the release of dense gas from the downwind source in the hill case at two streamwise positions.*
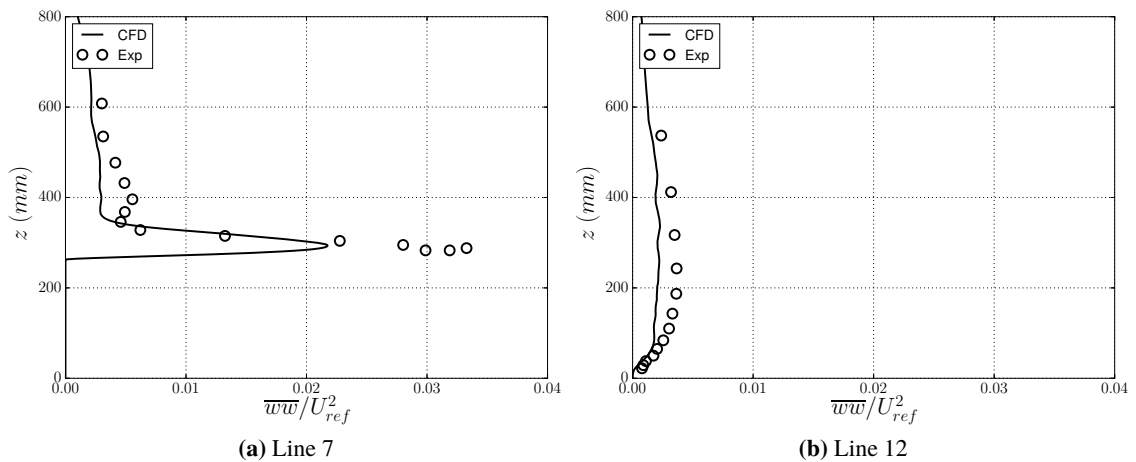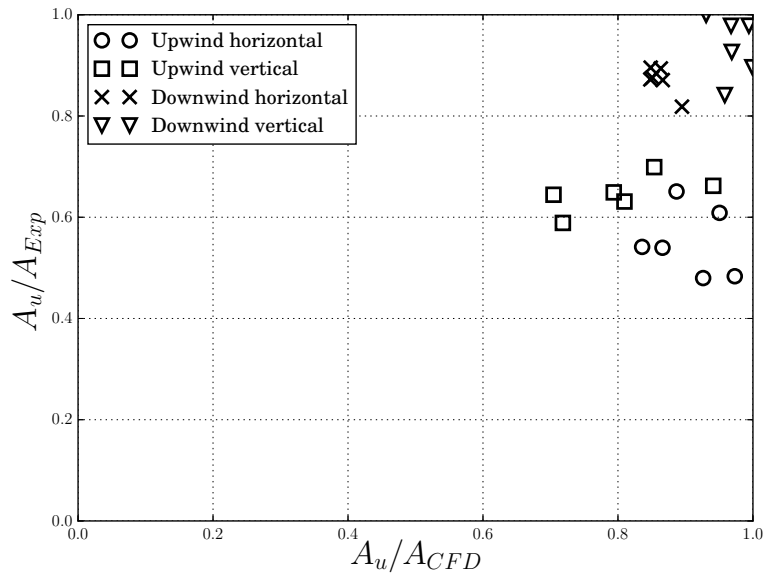

(a) Line 7

(b) Line 12

Figure 5.18 *Vertical profiles of $\overline{ww}/U_{ref}^2$ for the release of dense gas from the downwind source in the hill case at two streamwise positions.*

Figure 5.19 *MOE2 for the release of neutral gas from the upwind and downwind sources in the hill case.*

5.6.3 Simple array

In this section the LES results from the simple array simulations are presented. In Figure 5.20 the horizontal measurement positions are shown. Vertical measurements are taken according to Table 5.8. For each horizontal line, there is a vertical line with the same streamwise position. There are different streamwise positions between the neutrally buoyant and dense gas for line 3,4,9 and 10. Some of the LES results are mirrored around $y = 0$ due to symmetry.

Statistics are sampled for the quantities U, V, W, P, C, c, $\overline{uu}$, $\overline{vv}$, $\overline{ww}$, $\overline{uw}$, $\overline{uc}$, $\overline{vc}$ and $\overline{wc}$. Only some of the results are presented here.
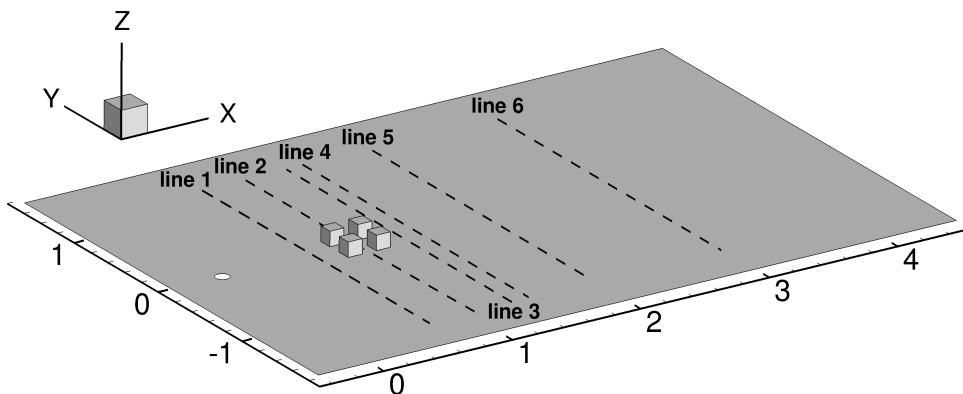

Figure 5.20 *The horizontal measurement positions for the neutral release in the simple array case.*

| Horizontal	x [m] neutral/dense	z [m]	Vertical	x [m] neutral/dense	y [m]
line 1	0.75/0.75	0.025	line 7	0.75/0.75	0
line 2	1.036/1.036	0.025	line 8	1.036/1.036	0
line 3	1.3/1.4	0.025	line 9	1.3/1.4	0
line 4	1.5/1.6	0.025	line 10	1.5/1.6	0
line 5	2.0	0.025	line 11	2.0	0
line 6	3.0	0.025	line 12	3.0	0
(a)			**(b)**		

Table 5.8 *Position of the measurement lines in the simple array cases with release of neutral/dense gas. (a) Horizontal lines and (b) Vertical lines*
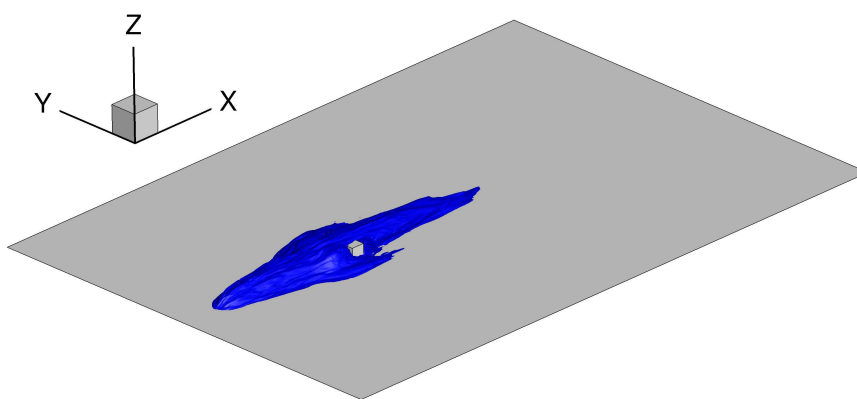
(a) Neutral gas
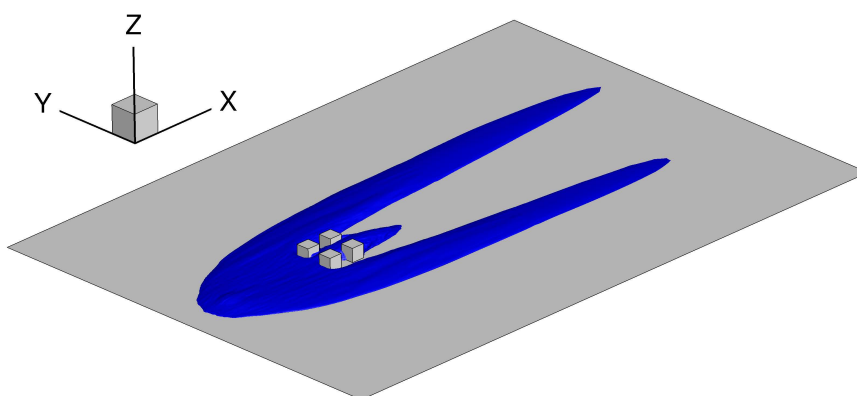
(b) Dense gas

Figure 5.21 *Iso-surface of the normalized concentration ($CU_{ref}/Q = 20$) for the simple array case. $C \approx 0.015$.*

In Figure 5.21 the released gas is visualized with iso-surfaces representing $CU_{ref}/Q = 20$ ($C \approx 0.015$). The difference between neutrally buoyant and dense gas is clearly visible: the spanwise spread is significantly greater for the dense gas and the plume is also shallower.
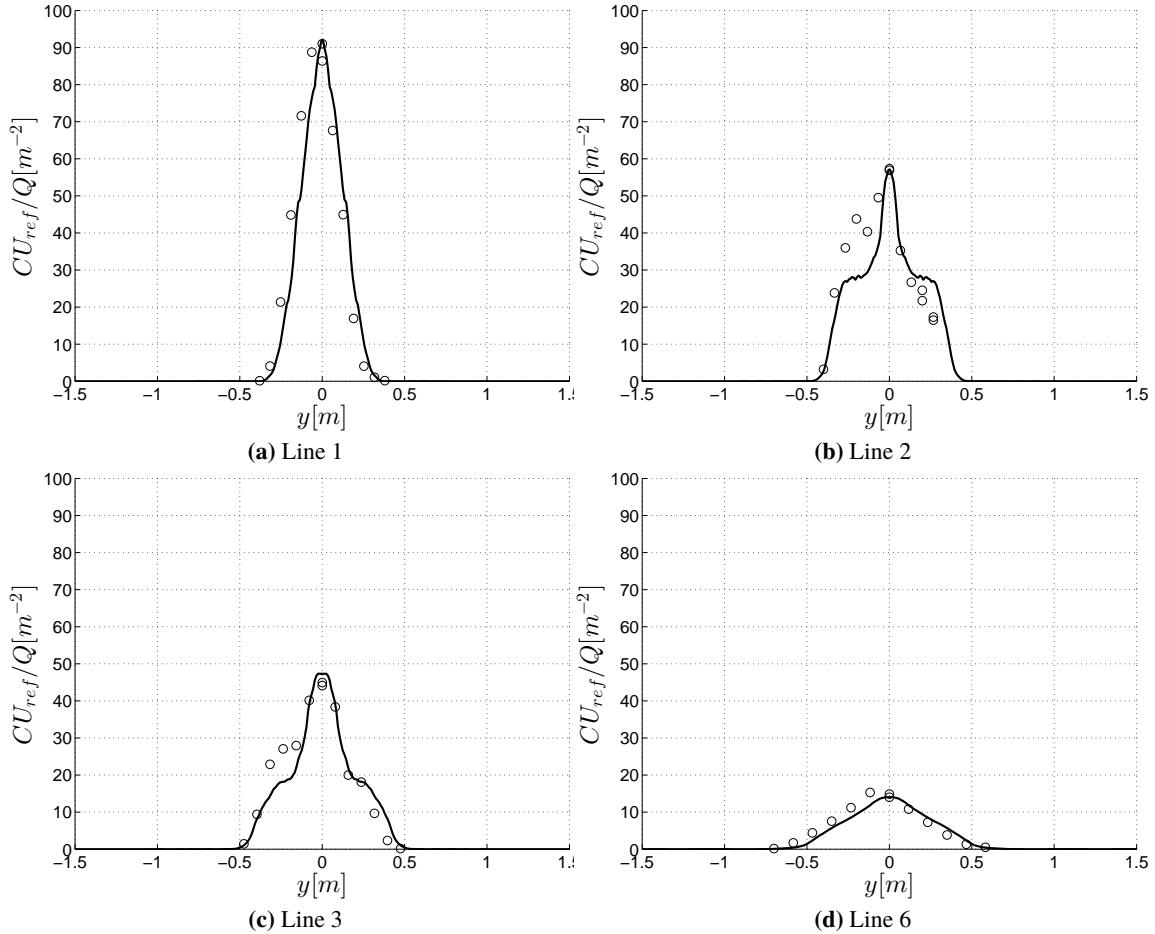

Figure 5.22 *Horizontal profiles of normalized mean concentration of neutral gas in the simple array case. Simulation data is mirrored around y = 0. Experimental value (○) and LES (———).*

Figure 5.22 shows the normalized mean concentration for the horizontal measurements. The neutrally buoyant LES results are very good compared to experimental data. Moving from Figure 5.22a which is positioned upstream of the blocks to Figure 5.22b which is inside, the concentration distribution changes due to the altered wind field. Interestingly, the concentration in between the blocks has a profound peak at $y = 0$ m. This is because the recirculation zone behind each block is advecting the gas towards $y = 0$. However, this effect is also present behind the last block (see Figure 5.22c) and reduced further downstream (see Figure 5.22d).

In Figure 5.23 the results from the vertical measurements for the neutrally buoyant release show very good agreements compared to experimental results. In Figures 5.24 and 5.25 the circulation zones behind the first row of blocks are visible. As mentioned earlier, the recirculation traps the gas and reduces the concentration behind each block. In Figure 5.25 the upstream recirculation, roof separation, and the downstream separation regions are visible. Also, not shown, are the side
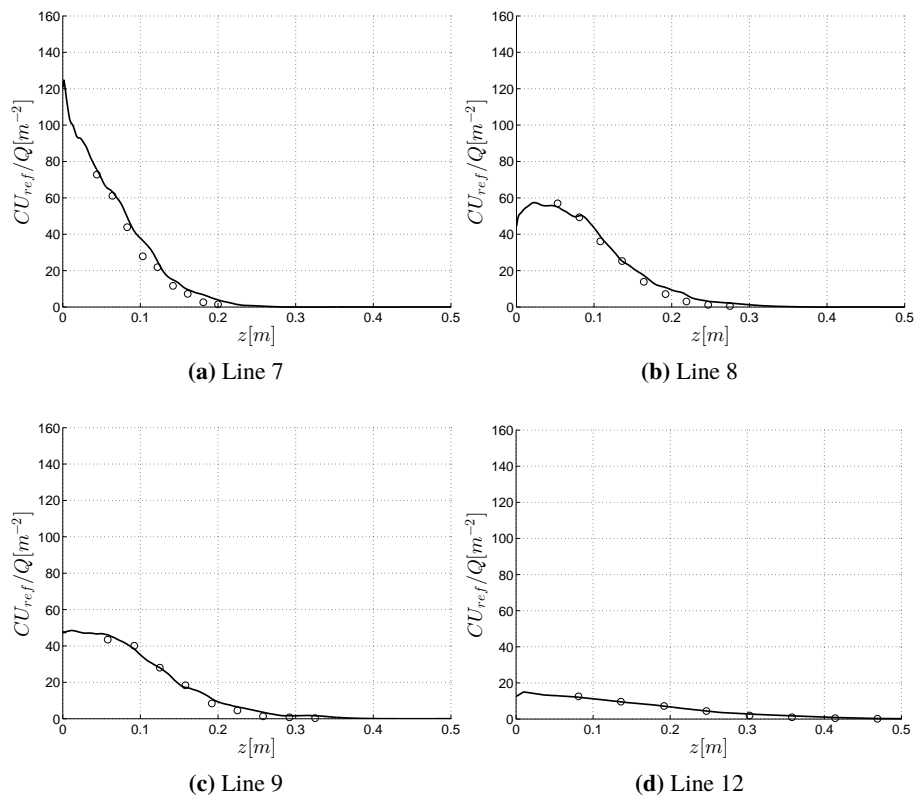
(a) Line 7

(b) Line 8

(c) Line 9

(d) Line 12

Figure 5.23 *Vertical profiles of normalized mean concentration of neutral gas in the simple array case. Experimental value (○) and LES (——).*

wall separation regions on the first row of buildings. The separation region behind the first row are filling the hole space defining this flow as a skimming flow regime. Interesting is the absence of roof and side recirculation regions on the second row of buildings. This is due to the favorable angle of the local wind direction over the second row of buildings.
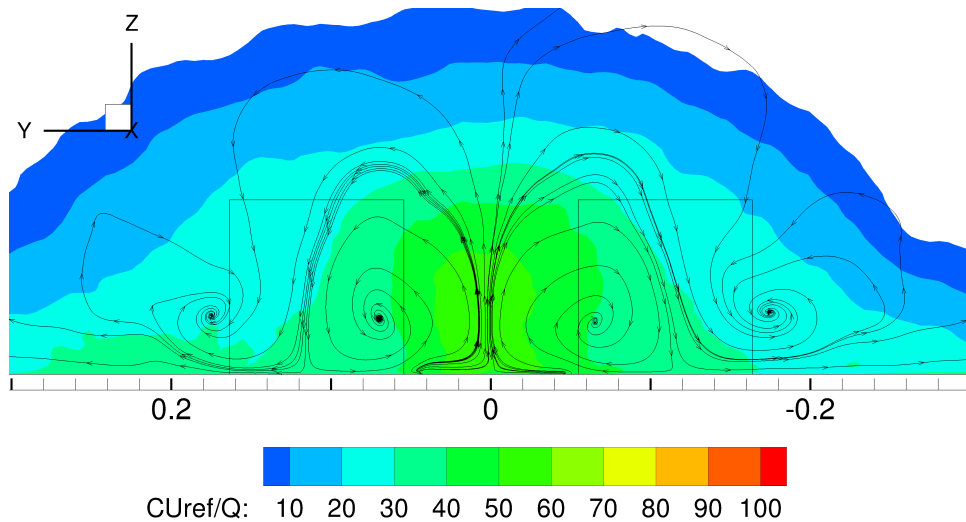

Figure 5.24 *Contour of averaged normalized concentration of neutral gas at $x = 2.47$ m. Streamlines calculated from spanwise and wall-normal velocity components.*
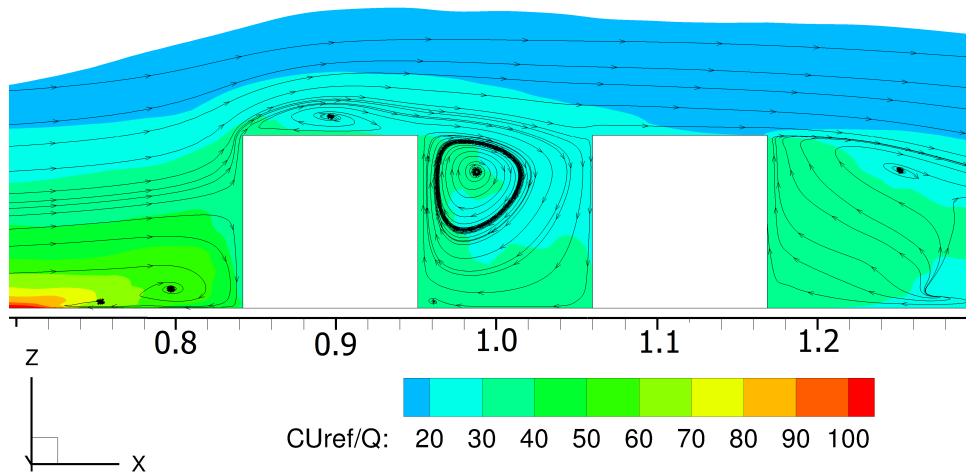

Figure 5.25 *Contour of averaged normalized concentration of neutral gas at $y = 0.1$ m. Streamlines calculated from streamwise and wall-normal velocity components.*

In Figure 5.26 the results of the horizontal measurements for the dense gas are shown. The same patterns as for the neutral gas, with a reduced concentration behind the blocks, are seen. There is a slight overprediction of the concentrations, especially for line 1 (see Figure 5.26a). The reason is the strong concentration gradient that is visible in the vertical measurements (see Figure 5.27a). This means that a slight shift of the plume position results in large deviations in the horizontal concentration profiles.
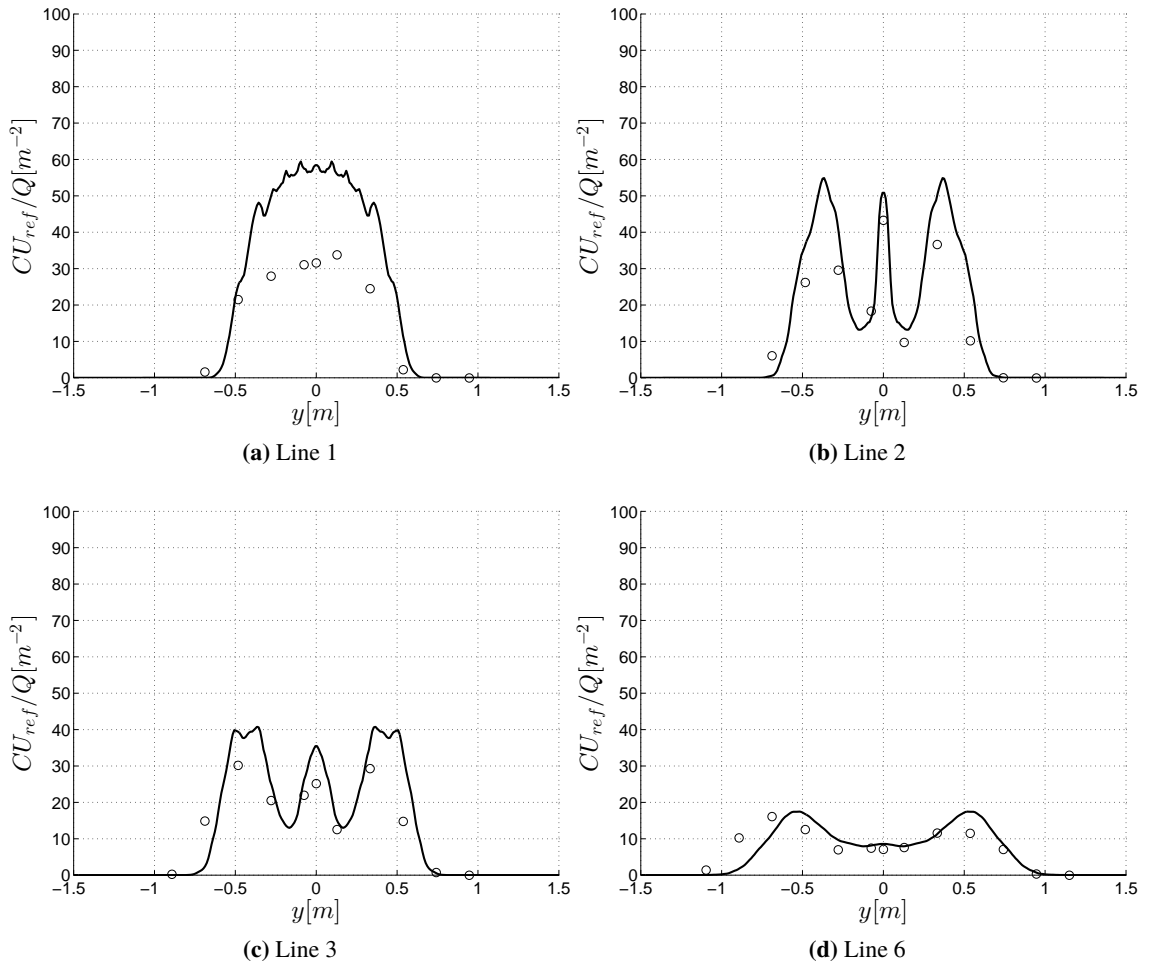
Figure 5.26 *Horizontal profiles of normalized mean concentration of dense gas in the simple array case. Simulation data is mirrored around y = 0. Experimental value(○) and LES (——).*

In Figures 5.28 and 5.29 the mean streamlines and normalized concentration are visible for the dense gas. Due to a more shallow plume compared to the neutrally buoyant gas plume, the the dense gas becomes more diluted when advected in the recirculation zone behind the first row of blocks. From Figure 5.26b there is a reduction of the maximum normalized averaged concentration with approximately 50% whereas the neutral release yields a reduction of around 40% (see Figure 5.22b)
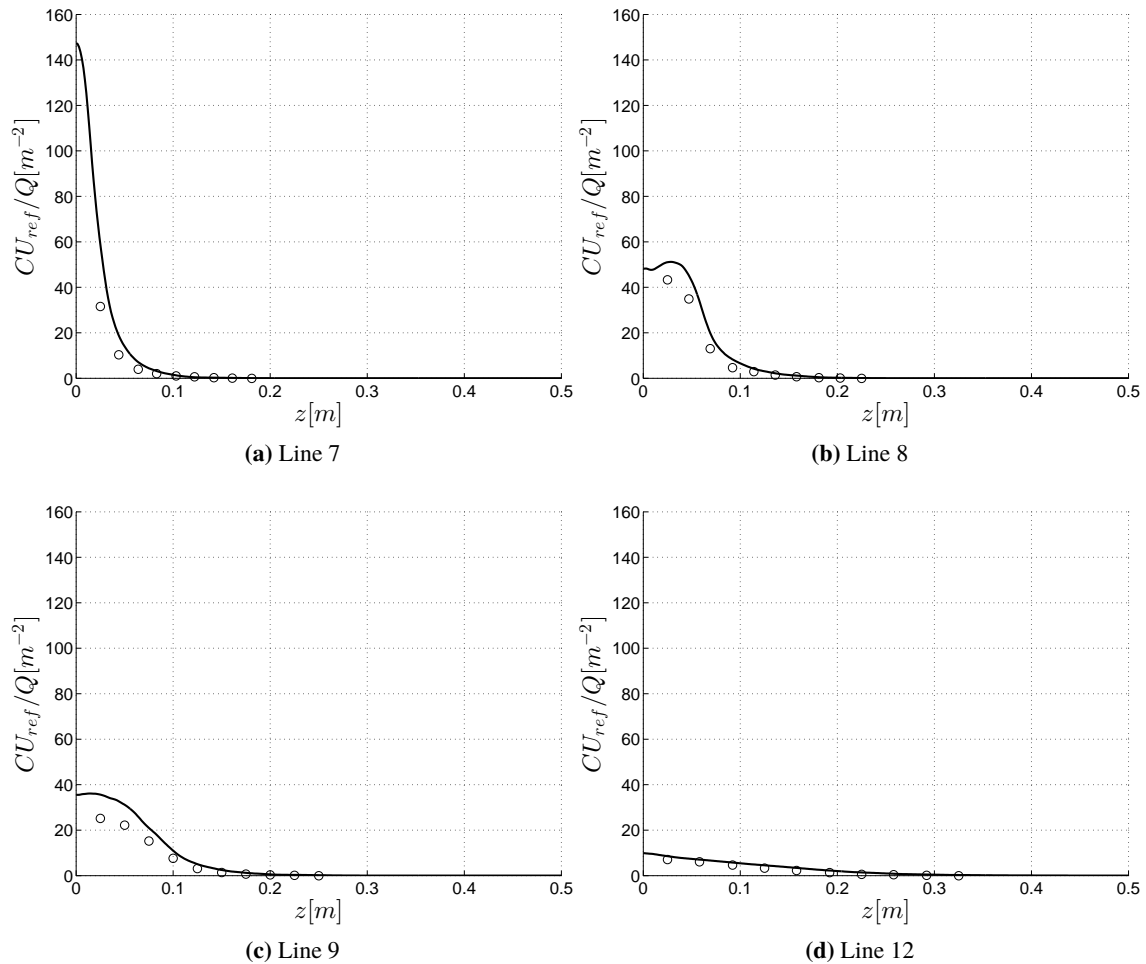

(a) Line 7

(b) Line 8

(c) Line 9

(d) Line 12

Figure 5.27 *Vertical profiles of normalized mean concentration of dense gas in the simple array case. Experimental (○) and LES (——).*

5.6.3.1 Differences between neutrally buoyant and dense gas.

In Figures 5.30 the dimensionless Reynold stresses are compared to experimental measurements upstream of the array at line 7. A small underprediction of $\overline{uu}$ and $\overline{uw}$ is visual. The simulations does, however, manage to predict the reduction of the stresses the dense gas introduces.

The gas is advected into the domain, hence the source is changing the boundary layer locally. Going from neutrally buoyant release to dense release, the momentum flux increases and the flow field
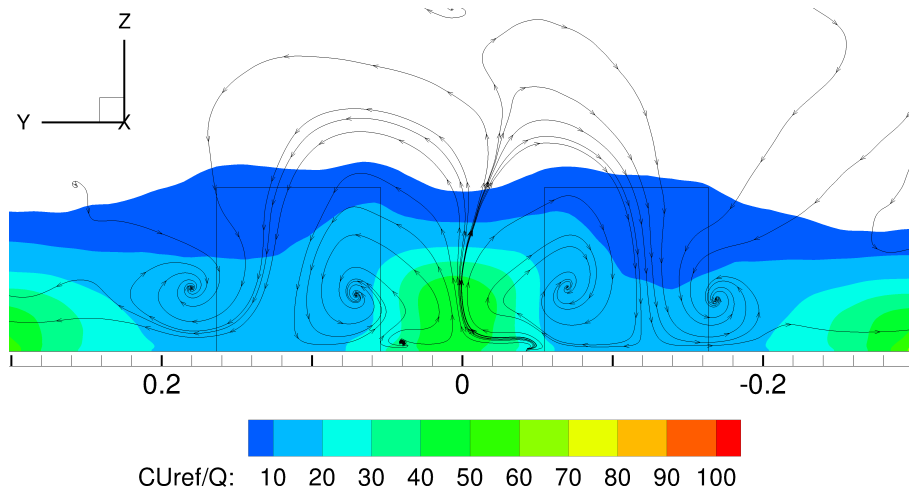
Figure 5.28 *Contour of averaged normalized concentration of dense gas at $x = 2.47$ m. Streamlines calculated from spanwise and wall-normal velocity components.*
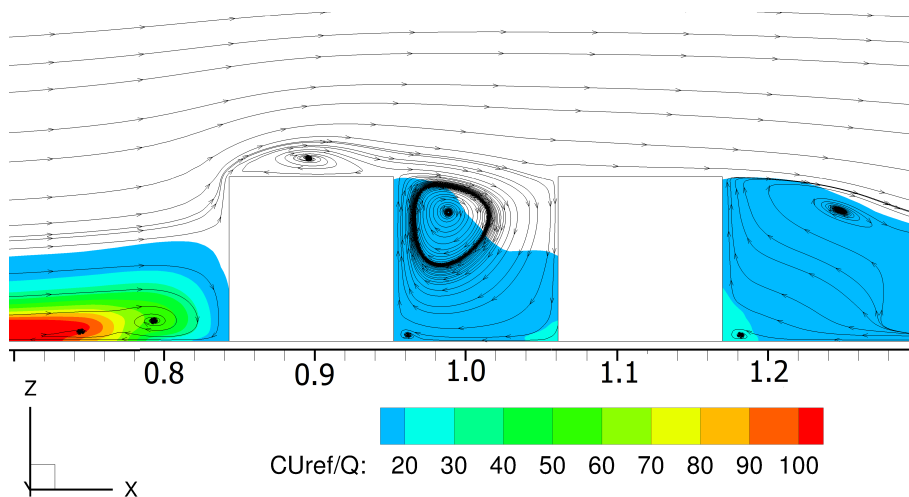

Figure 5.29 *Contour of averaged normalized concentration of dense gas at $y = 0.1$ m. Streamlines calculated from streamwise and wall-normal velocity components.*
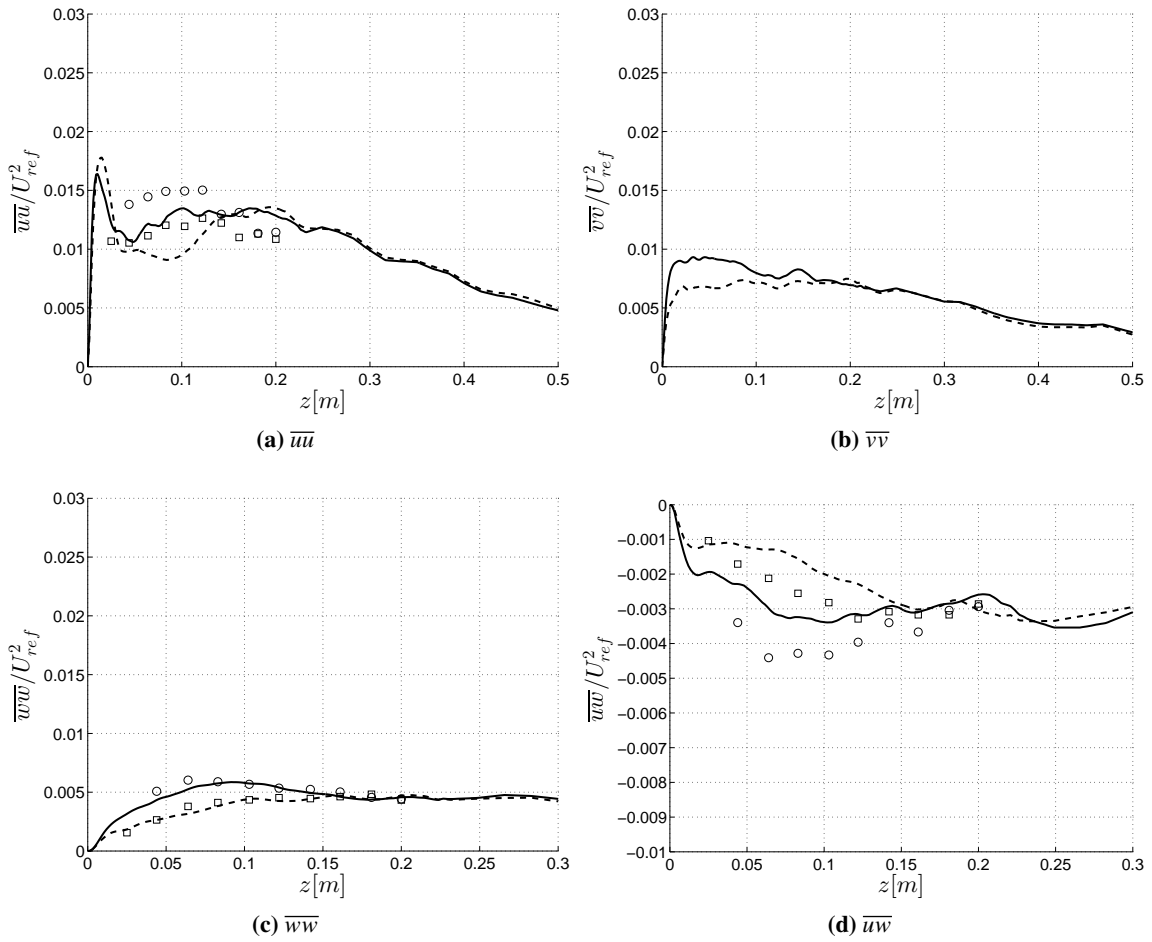
Figure 5.30 *Vertical profiles of dimensionless Reynolds stresses taken at line 7. Symbols denote experimental values and lines LES results. Neutral gas (○) and (——). Dense gas (□) and (−−−).*

around the source is getting more complex. Recirculation zones are developing both upstream and downstream (see Figure 5.31b). These recirculation zones are advecting the dense gas upstream and towards the ground behind the source. This effect is reduced for the neutrally buoyant gas, keeping the gas elevated downstream and the spanwise velocity almost not affected. The spanwise flow upstream of the source is similar to the flow downstream (see Figure 5.32a), suggesting a small region between the source and the cubes, where the spanwise transport only is governed by turbulent convection. The release of dense gas on the other hand introduces a spanwise velocity in both directions away from the source (see Figure 5.32b).
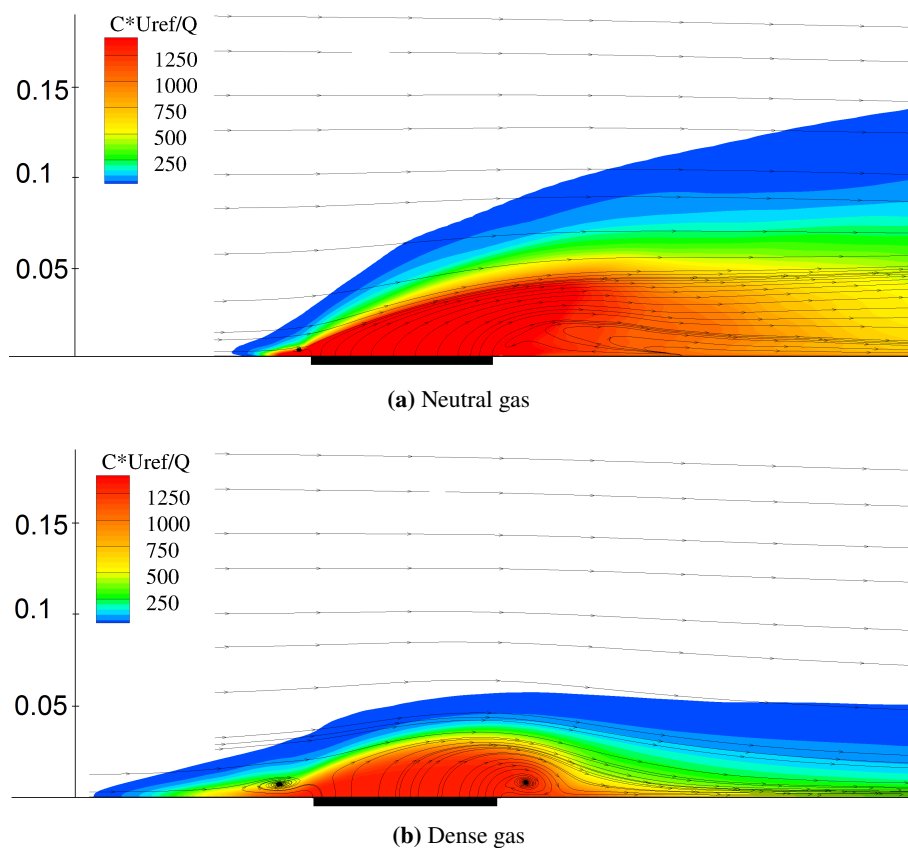

(a) Neutral gas

(b) Dense gas

Figure 5.31   *Contours of normalized averaged concentration with streamlines computed from stream-wise and wall-normal velocity components. The plane shown is $y = 0$ m and the source location is marked with a thick black line.*

The turbulent convection (scalar fluxes) is compared to experiments in Figure 5.33. It is seen that the model is capable of predicting the turbulent convection for both the dense and neutrally buoyant gas. The mixing in the wall-normal direction is the same for the dense and neutral gas up to around 3 cm. Then the neutral mixing continuous to rise while the dense gas mixing is reduced.

(a) Neutral release

(b) Dense gas release

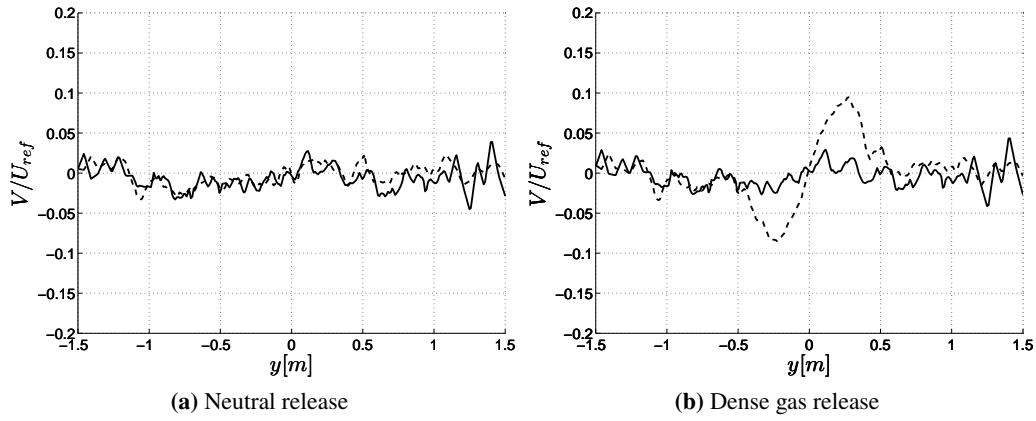**Figure 5.32** *Lateral profiles of the normalized spanwise velocity at $z = 0.01$ m. $x = -0.25$ m (——) and $x = 0.4$ m (– – –).*
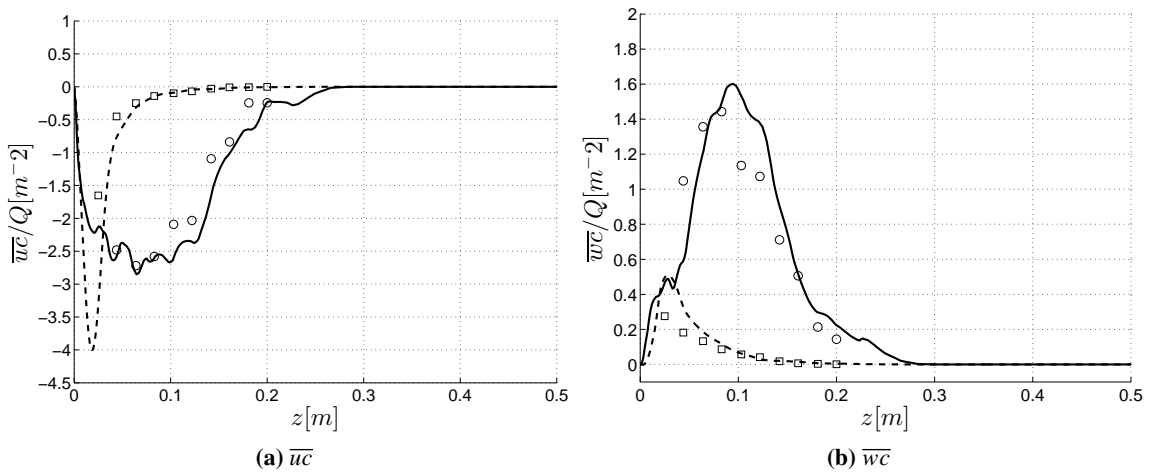

(a) $\overline{uc}$

(b) $\overline{wc}$

Figure 5.33 *Vertical profiles of scalar flux components taken at line 7. Symbols denote experimental values and lines LES results. Neutral gas (∘) and (——). Dense gas (□) and (– – –).*

5.6.3.2 *Method verification.*

In Figures 5.22 - 5.27 the normalized concentrations are compared to the experimental results. The width and height are predicted with good results for the neutrally buoyant and dense gas. The distribution of the neutrally buoyant gas is predicted with very good results, even if the experimental results shows slightly unsymmetrical plumes. If neglecting the effect of molecular diffusion, the good agreement between the LES results and the experimental results for release of neutral gas suggests that the wind field is very well predicted.

For the LES simulation, the neutrally buoyant release have an averaging time of 29 s, which by the very good results seems to capture most of the shedding effects. Even with the concentration not mirrored around y = 0, the plumes are fairly symmetric. This suggests that both the model and grid size are good enough to sustain the dynamics within the boundary layer. The non-zero spanwise velocity (see Figure 5.32a) is probably due to the short distance between the source and roughness elements. Between an averaging time of 34.3 s and 75.7 s, the concentration was stable for the dense gas, which suggests that the averaging time is sufficient to capture the shedding effects generated by the blocks and source.
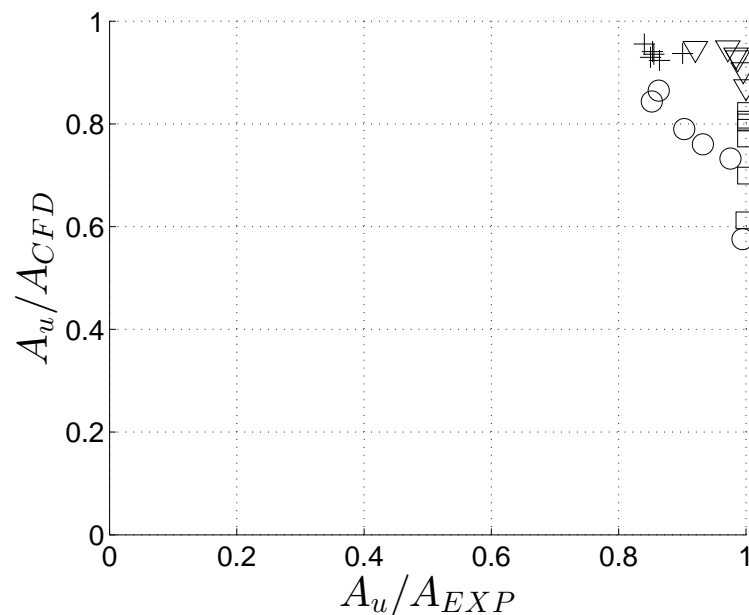
Figure 5.34 *Measure of effectiveness with false positive prediction as a function of false negative prediction for the simple array case. Neutral, horizontal values (+), neutral, vertical values (▽), dense, horizontal values (○) and dense vertical values (□).*

In Figure 5.34 the LES and experimental results are compared by how much the normalized concentration is overpredicted or underpredicted. It is clear that the model easier can predict the neutrally buoyant gas. The small overprediction of the vertical dense profile is also seen.

5.6.4 Paris

This section presents the results from the Paris scenario. In Figure 5.35 the four horizontal measurement lines, placed at $z = 0.12$ m which is just above the rooftops, are shown. The vertical lines defined in Table 5.9 are placed in the main streets. There are also measurements within the street network at $z = 0.01$ m.
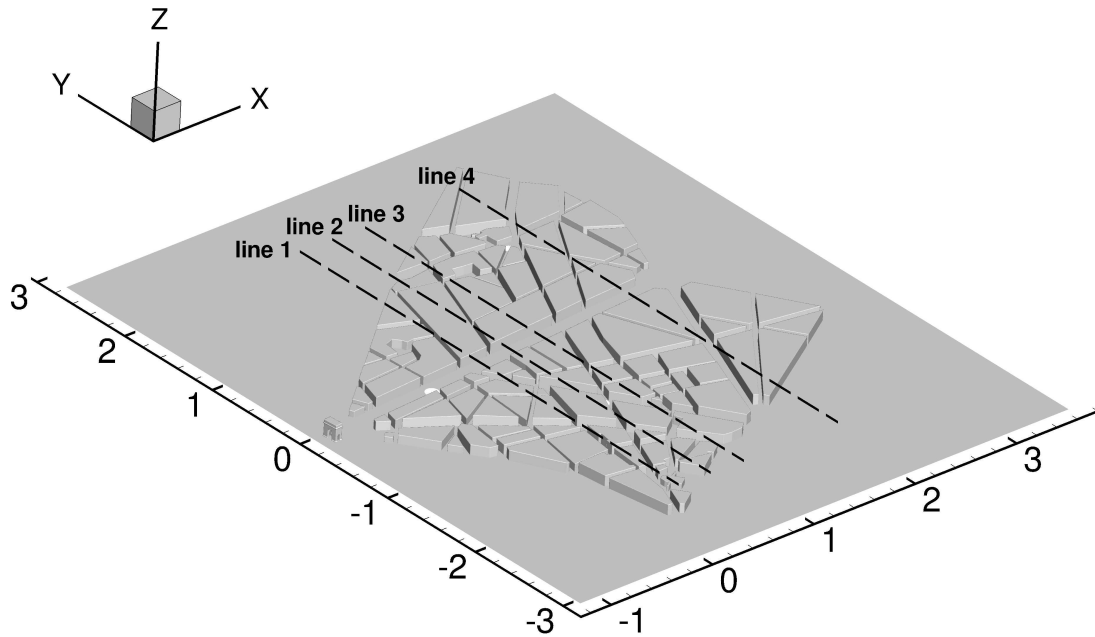

Figure 5.35 *Paris layout*

Horizontal	x [m]	z [m]
line 1	0.50	0.12
line 2	0.75	0.12
line 3	1.00	0.12
line 4	2.00	0.12
(a)		

Vertical	x [m]	y [m]
line 5	0.50	0.041
line 6	1.00	0.082
line 7	2.00	0.164
(b)		

Table 5.9 *Position of the measurement lines in the Paris cases. (a) Horizontal lines and (b) Vertical lines*

In Figure 5.36 the instantaneous concentration is shown for both the neutrally buoyant and dense gas. The main street is tunneling the gas and the effect is most visible for the neutral gas. The dense gas is dispersed in the spanwise direction and remains mainly within the street network, however, there are areas where low concentration is passing above the buildings. Also, the dense gas is transported upstream.

Comparing the wind tunnel results (see Figure 5.38) to the LES results (see Figure 5.37), similar patterns are found. Even though the color scale is not compatible the behavior of the gas can still be
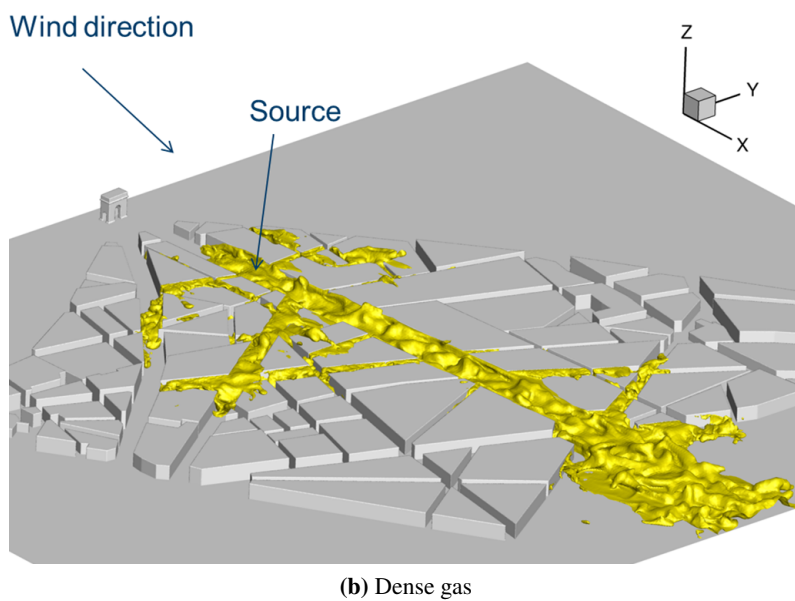
(a) Neutral gas

(b) Dense gas
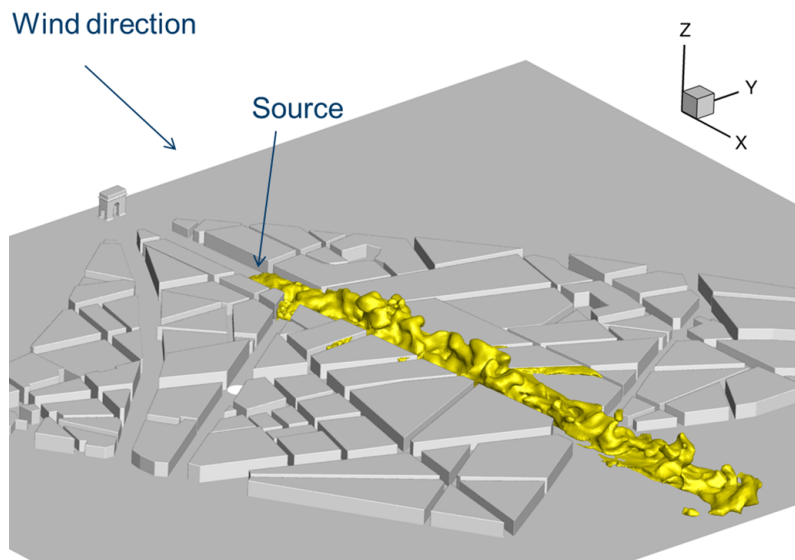
Figure 5.36 *Iso surface of the instantaneous concentration.*

CUr/Q
40 80 120 160 200 240 280 320 360 400

(a) Neutral gas

CUr/Q
40 80 120 160 200 240 280 320 360 400

(b) Dense gas
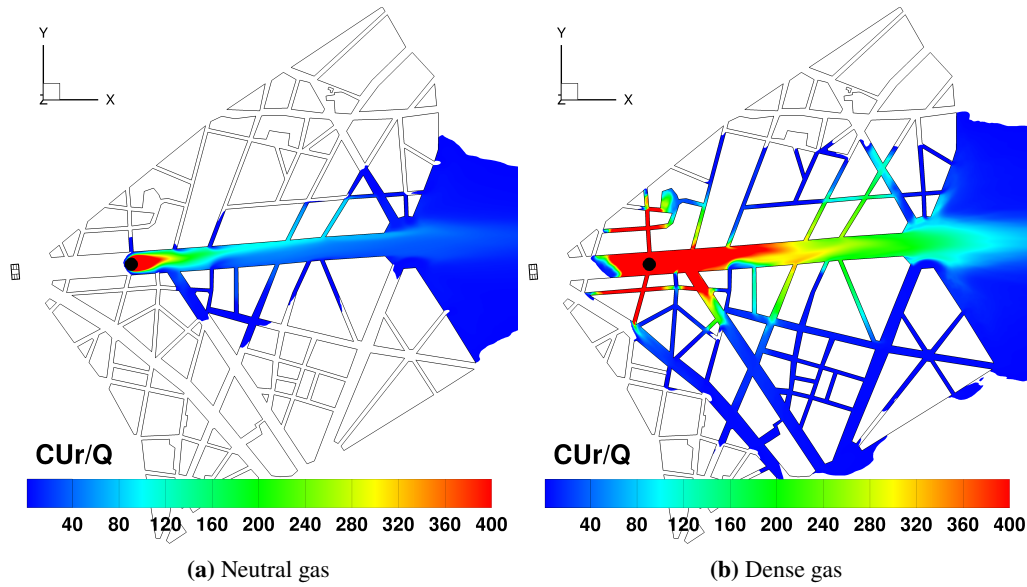
Figure 5.37 *Contours of normalized time averaged concentration close to the ground ($z = 0.01$ m) in Paris.*

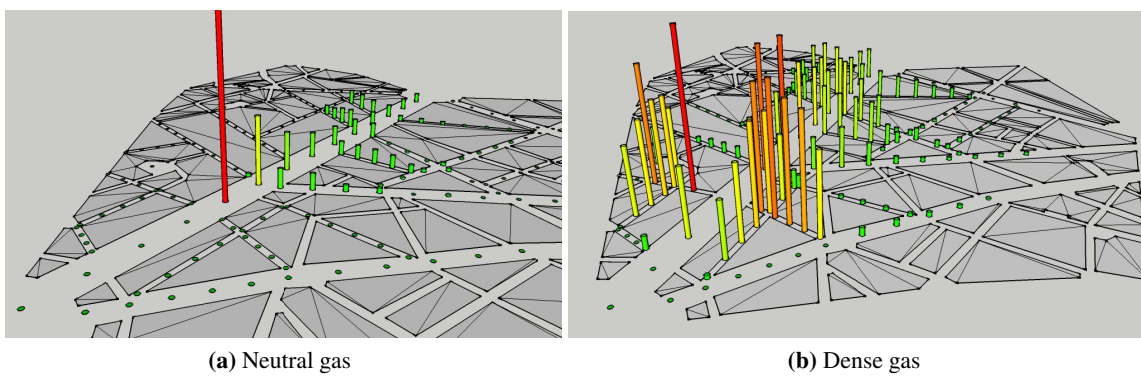**(a)** Neutral gas

(b) Dense gas

Figure 5.38 *Bar plot of normalized concentration measurements from the wind tunnel. Measurements are taken close to the ground ($z = 0.01$ m) for the Paris case. Jack Benson 2015.*

analyzed. For the neutral release, the plume is following the main street with higher concentration towards the left side of the avenue (positive y-direction). The reason is that the wind field is not exactly aligned with the main street and creates a low pressure region in this area. Due to this, the gas is transported into two side streets further downstream which is seen both in the simulation and wind tunnel results. The same effect is visible for the dense gas release, however, the dense gas effect is very strong which results in larger spanwise dispersion. Comparing the simulation to the experiment show the same patterns, especially around the source.

(a) Line 1

(b) Line 4

(c) Line 5

(d) Line 7

Figure 5.39 *Horizontal and vertical profiles of normalized time averaged concentration of neutral gas in Paris. Experimental value (○) and LES (——).*

In Figures 5.39a and 5.39b the mean concentration of neutrally buoyant gas is compared to experimental results. The horizontal measurements are taken above roof height at $z = 0.12$ m. Here, it is clearly seen that the neutral gas remains above the main street. Also, the gas is advected towards the left side as mentioned earlier. The vertical measurements (see Figures 5.39c and 5.39d) are taken at the center of the main street and misses the high concentration visible in the horizontal results. Both the horizontal and vertical results correspond well to experiments.
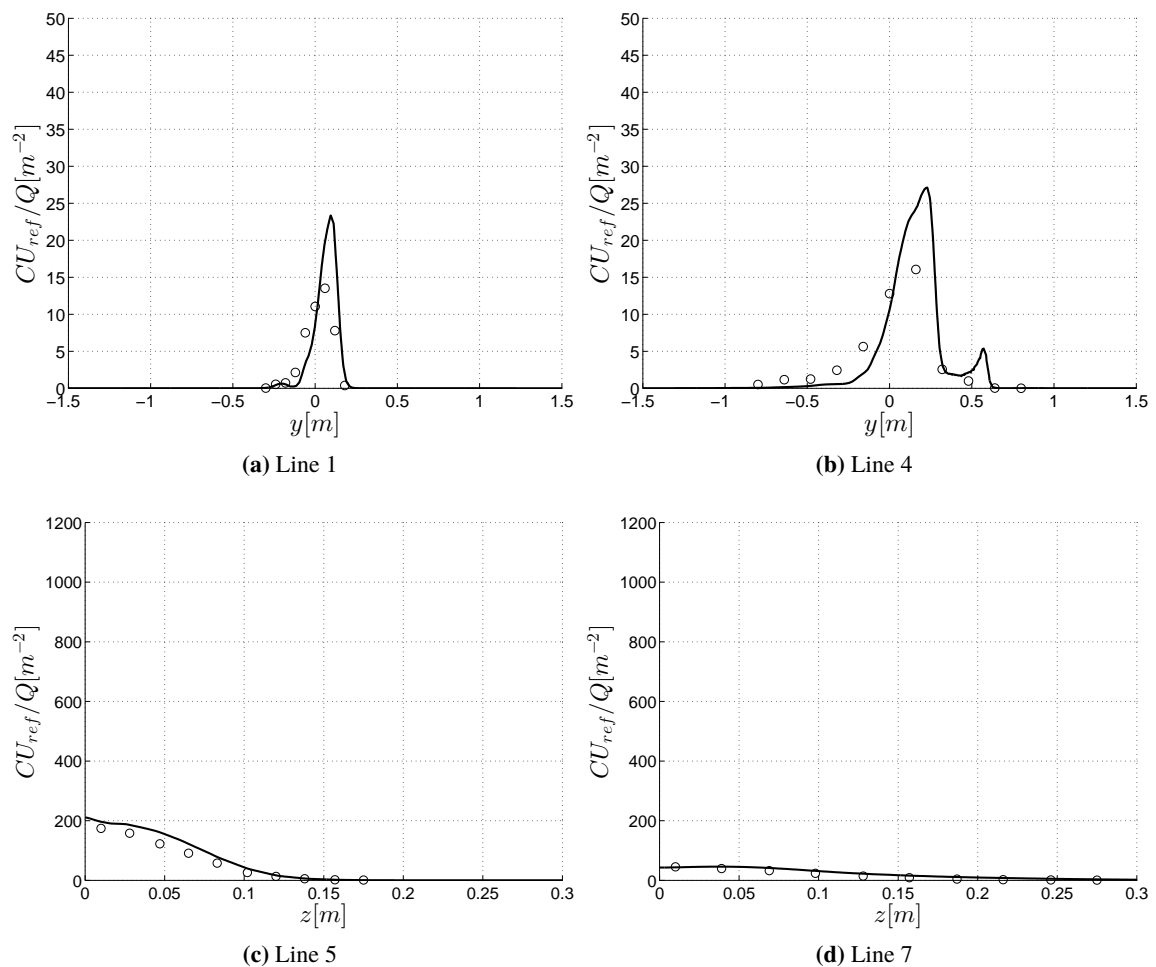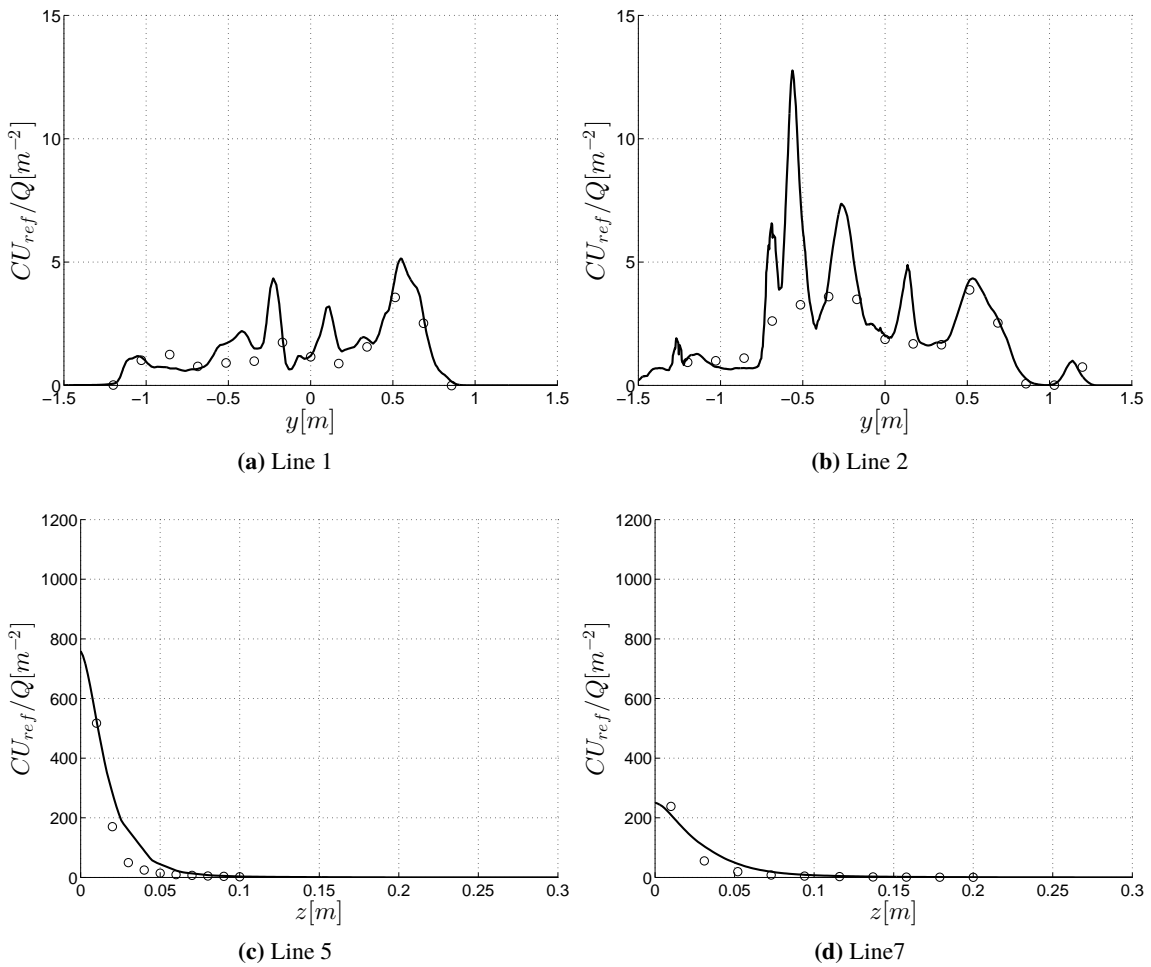
Figure 5.40 *Vertical and horizontal profiles of normalized time averaged concentration of dense gas in Paris. Experimental value (○) and LES (——).*

In Figures 5.40a and 5.40b the mean concentration of dense gas is compared to experimental results. There are overall very good agreement above the rooftops ($z = 0.12$ m). However, there are areas where the LES results deviates (see Figures 5.40b). The peaks (around $y = -0.5$ m) are most likely due to buildups of gas within the streets that spills over the rooftops. The vertical measurements are shown in Figures 5.40c and 5.40d where a slight overprediction is visible, but overall a very good prediction.
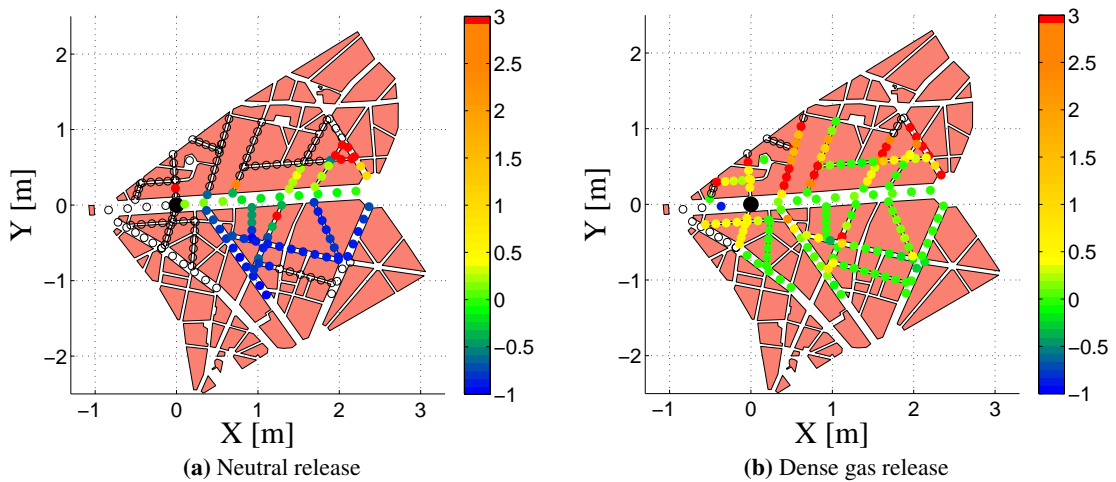

(a) Neutral release

(b) Dense gas release

Figure 5.41   *The difference between experimental and LES results at z = 0.01 m for Paris with release from source 1. Empty circles are areas where both experimental and LES results are below C = 0.001. A positive collar value of 1 means that the LES result is overpredicting by a factor of 1.*

From Figures 5.37 and 5.38 it is clear that the main features of the gas plumes predicted by the LES corresponds to the results from wind tunnel. Figure 5.41 show the difference between the numerical and experimental results with very good agreement along the main street for both the dense and neutrally buoyant gas. When considering the outer regions of the plume the results start to deviate. Considering Figure 5.42 its clear that the low concentrations deviates more than higher concentrations. The combined conclusion is that it is more difficult to predict the low concentrations on the outer edge of the plume correctly.

In the Paris scenario there are many buildings that creates shedding effects and recirculation regions. For the dense gas, the horizontal and vertical mean concentration remains relatively steady when comparing a 47.9 s average to a 60.8 s average. For the neutrally buoyant gas, the mean concentration is changing when comparing to a shorter time average which suggests that the dense gas is reducing the time scale for plume shedding.

In Figure 5.43 the measures of effectiveness for the vertical and horizontal profiles are shown with good results. The LES results for the dense gas release have a tendency to overpredict rather than underpredict.

(a) Neutral release

(b) Dense gas release
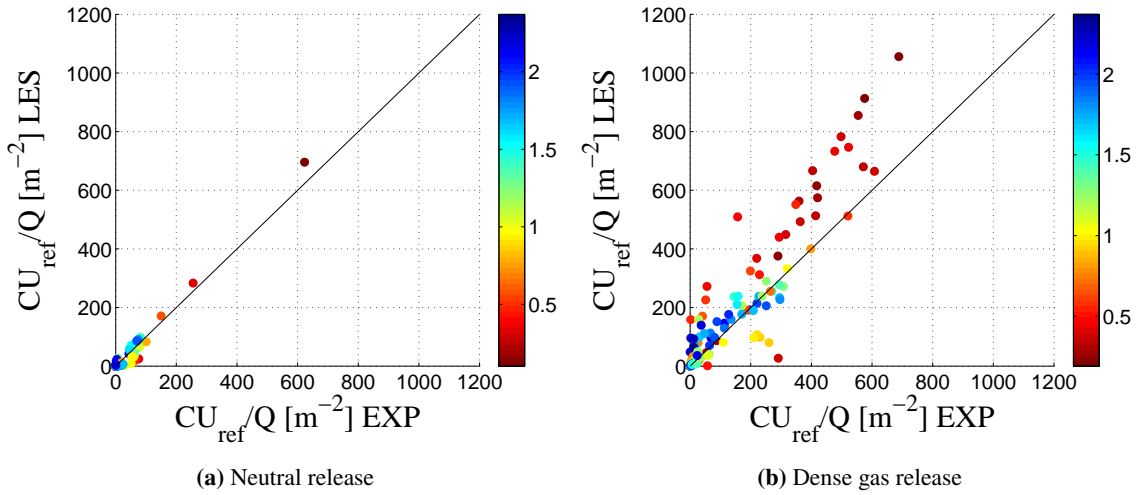
Figure 5.42 *Normalized LES concentration as a function of the experimental results, at z=0.01 m. The color represents the distance from the source.*
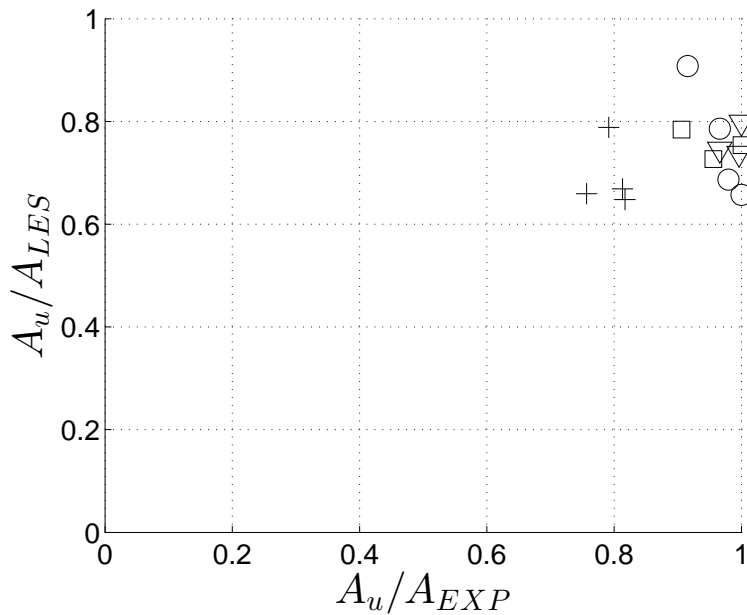

Figure 5.43 *Measure of effectiveness with false positive prediction as a function of false negative prediction in the Paris case with release from source 1. Neutral, horizontal values(+), neutral, vertical values (▽), dense, horizontal values (○), and dense, vertical values (□).*

5.7 Conclusions

5.7.1 Turbulent boundary layer

In this study, two different incoming turbulent boundary layers are used. Both are generated separately with an inflow boundary condition corresponding to the mean streamwise velocity of the experiment and added fluctuations. The instantaneous wind field is stored and discretized in both time and space. For the hill case the closest time step is matched, and for simple array and Paris scenario, a linear interpolation is used to create a smooth transition in time. The hill simulations use a flat surface in contrast to the other cases were roughness elements are used to increase the wall-normal velocity gradient and produce turbulence kinetic energy, which is lost due to adaptation (see Section 5.6.1). When using the roughness element method the Reynold stresses correspond well to experiments. Not using roughness elements results in a reduced turbulence kinetic energy in the upper regions of the boundary layer.

The spanwise velocity (see Figure 5.32b) upstream of the simple array, which is not influenced by buildings, is non-zero even after a 75 s average. This suggests that a theoretical flat plate turbulent boundary layer is not present. The very good results in predicting the dispersion of neutrally buoyant gas (see Figures 5.22 and 5.23), and that the turbulent integral time scale derived from experiments in [16] does not exceed 1 s, suggest that the 29.2 s cycle is adequate to represent the turbulent boundary layer and that the non-zero spanwise velocity is a roughness element effect.

5.7.2 Prediction of released gas

If considering neutrally buoyant gas (see Figure 5.19) for the hill case, it is clear that the downstream source gives better results compared to the upstream source. The difference between these two cases is the adverse pressure gradient behind the crest that affects the wind field upstream of the source. For the simple array, the wind field is not affected by the geometry before the source but even so the experimental results are reproduced with good agreement. The difference between the hill and the simple array simulations is the incoming boundary layer. The lower turbulence kinetic energy for the hill simulations suggests that a reduced turbulent convection could be the reason for the reduced wall-normal and spanwise spread for the upstream source. This shows the importance of a well-defined incoming boundary layer in order to predict the flow and dispersion correctly, especially in the absences of geometry affecting the wind field.

The dispersion of neutral and dense gas is in overall well predicted. The plumes correspond to the experiments, and the effect of the dense gas is visible. The prediction of the neutral gas for the simple array and the hill (downstream source), shows very good results when comparing the different MOE2 plots (see Figures 5.34 and 5.19). Even if the grid size is larger for the hill than the simple array, it seems to be sufficient to represent the effect of the adverse pressure gradient behind the crest. In the Paris model, the plumes, both neutral and dense, predicted using LES are comparable to the experimental results. The normalized concentration deviates when the concentration is low and far away from the source. It is in these areas small deviations from the wind tunnel results are most visible.

5.7.3   The dense gas effect on the wind field

Releasing dense gas is changing the wind field. The most visible effect is the increased average spanwise velocity which creates a wider plume (see Figure 5.32). A recirculation area is also formed on the upstream side of the source, which transports the dense gas upstream. The most visible changes are around the source, which is logical since this is where the local gradient Richardson number is the highest. Comparing the Reynolds stresses just downstream of the source suggests that the dense gas is reducing the turbulence kinetic energy (see Figure 5.30).

5.7.4   Overall conclusions

The developed LES methodology, using an incoming turbulent boundary layer corresponding to the experiment, is very well suited for predicting dispersion of both dense and neutrally buoyant gases in urban-like geometries. The method is suitable both for the simpler cases investigated as well as the ones with a more complex wind field. The mean flow statistics, Reynolds stresses, concentrations and scalar fluxes have been successfully predicted. Changes imposed on the wind field by the dense gas have been observed, especially close to the source where the dense gas effect is greatest. This yields a transport of gas upstream of the source as well as a larger spanwise spread.

6 Work conducted by FOI Sweden

This chapter is authored by FOI who is also responsible for the quality validation.

6.1 Objectives

FOI uses a range of contaminant transport models. These range from the simplest gaussian plume models to complex CFD-based tools. Neither of these have been extensively tested for release of dense gases. Understanding of the physics of dense gas release is necessary for improving the design and use of fast operational model. This understanding includes the implications of release properties, dispersion, geometry and model complexity. The objective of the present FOI participation is to study the simulated effects of dense gas releases and to validate these using wind tunnel experimental data.

6.2 Mathematical modelling

Paris simulations (c.f. Chapter 2 and Table 2.1) for neutral and dense gas releases were performed for source number 2, with a wind direction of $220°$. The simulations were carried out using the finite volume method with the OpenFOAM[1] [20],[21] package and the FOI inhouse implementation of subgrid modelling for incompressible LES, *oodlesFOI*. The solver is based on the predictor-corrector *PISO* (Pressure Implicit with Splitting of Operators) algorithm.

6.2.1 Turbulence modelling

When the incompressible Navier-Stokes equations are filtered,

$$\frac{\partial \overline{u}_i}{\partial t} + \overline{u}_j \frac{\partial \overline{u}_i}{\partial x_j} = -\frac{\partial \left(\overline{p} \delta_{ij} + \tau_{ij} \right)}{\partial x_j} + \nu \frac{\partial^2 \overline{u}_i}{\left(\partial x_j \right)^2}, \tag{6.1}$$

the subgrid stress tensor τ_{ij} remains unknown and must be modelled in terms of the resolved velocity field $\overline{u}$. There are several ways of modelling the subgrid-scale turbulence, the most popular are possibly those based on the eddy viscosity hypothesis. That states that the subgrid-scale momentum transfer due to turbulent eddies can be modeled as a viscosity. This means that,

$$\tau_{ij} = 2\nu_T \overline{S}_{ij} + \frac{1}{3} \delta_{ij} \tau_{kk}, \tag{6.2}$$

---

[1]www.openfoam.org

where ν_T is the *eddy viscosity* and,

$$\overline{S}_{ij} = \frac{1}{2}\left(\frac{\partial \overline{u}_i}{\partial x_j} + \frac{\partial \overline{u}_j}{\partial x_i}\right),$$ (6.3)

is the strain rate tensor. Popular models for the eddy viscosity are e.g. the *Smagorinsky* model [22] or the *OEEVM* (One Equation Eddy Viscosity Model) [23]. In the latter a transport equation is solved for the subgrid-scale kinetic energy and the turbulent viscosity is modeled as,

$$\nu_T = C_\tau k_{sgs}^{3/2}\Delta,$$ (6.4)

where Δ is the LES filter width (usually mesh size dependent) and C_τ is a coefficient. The coefficient C_τ is sometimes a constant like in the OEEVM and it is sometimes dynamic. In the *LDKM* (Localized Dynamic Kinetic energy Model, [24]) the coefficient is dynamically computed from the resolved flow. In [24] it is noted that because of similarity between the subgrid-scale stress and the resolved stress originiating in a larger test filter (typically twice the size of the mesh filter), expressions can be obtained for C_τ as well as for the turbulent dissipation rate ϵ.

6.2.2   Dispersion modelling

Released gases are dispersed using a transport algorithm where the concentration C follows the flow:

$$\frac{\partial C}{\partial t} = -\overline{u}_j\frac{\partial C}{\partial x_j} + \nu\frac{\partial^2 C}{\left(\partial x_j\right)^2},$$ (6.5)

evaluated with the updated velocity in each time step, implicitly using a unity Schmidt number. The concentration field is then a passive scalar within a homogeneous gas volume.

dense gas is modelled using a Boussinesq approach, e.g. [25]. The vertical momentum equation

$$\frac{Dw}{Dt} = -\frac{1}{\rho_0}\left(\frac{\partial p}{\partial z}\right) + \nu\frac{\partial^2 w}{\left(\partial x_j\right)^2},$$ (6.6)

where the total derivative has been used, is changed to

$$\frac{Dw}{Dt} = -C\frac{\rho'}{\rho_0}g - \frac{1}{\rho_0}\left(\frac{\partial p}{\partial z}\right) + \nu\frac{\partial^2 w}{\left(\partial x_j\right)^2}.$$ (6.7)

In the case of no release, this change does not alter the solution. However, in the case of a present gas, the volume will experience an acceleration depending on the size and sign of ρ'.

It is worth noting that this model only includes an extra forcing on the flow. It does not allow the flow dynamics to affect mixing of the gases, or cross-species momentum fluxes. For that treatment a mass fraction in combination with a proper Schmidt number and varying density treatment is necessary. The present way of modelling was chosen for simplicity and the possibility of including it in simpler models.

6.3 Meshing procedure

The mesh is constructed using the OpenFOAM tools *blockMesh*, *extrudeMesh*, and *snappyHexMesh*. First, a low square block is created using blockMesh. That mesh is $12 \times 3.5 \times 0.16$ m^3, consisting of only cubic hexahedras with an 8 mm side length. The mesh is decomposed. Then the snappyHexMesh utility is invoked running in parallel. The utility is set up to refine resolution three times to the lower boundary, giving cubic hexahedras with a 1 mm side lenght; and two times to the houses, giving cubic hexahedras with a 2 mm side length. After the refinement, mesh cell sides are "snapped" onto the surfaces of the geometries. The two geometries, lower boundary with roughness elements and houses, are given in two files in STL-format. Once the mesh is created, the extrudeMesh utility is used to extrude cells from the top of the mesh to the top of the wind tunnel. Finally, the mesh is reconstructed using the *reconstructParMesh* utility. Figure 6.1 shows an illustration of the simulated domain.
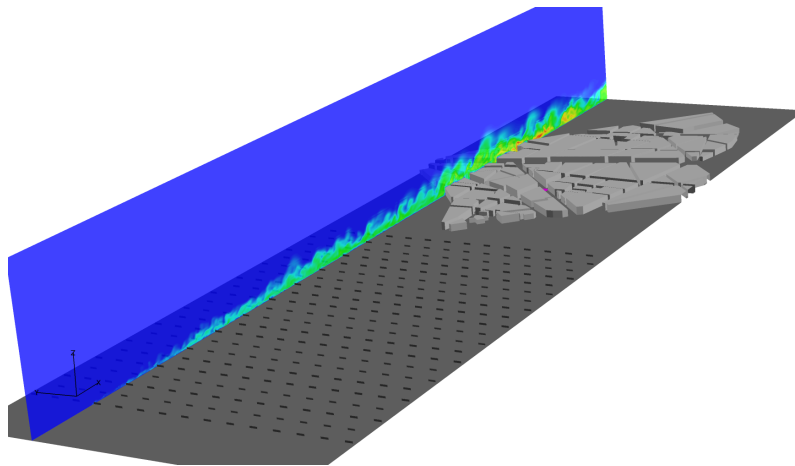

Figure 6.1 *View of the domain, with semi-transparent view of growing subgrid kinetic energy.*

6.4 Boundary condition

The simulation uses seven boundaries. One for each of the four walls of the wind tunnel, the ceiling, the floor of the wind tunnel together with the houses, and the source. The source is set to be a number of boundary faces on the wind tunnel floor. The side walls, floor, and ceiling are set to boundary type *wall* while the inlet, source, and outlets are of type *patch*, both names are OpenFOAM boundary keywords, [21]. The boundary conditions used are summarized in Table 6.1.

An inlet profile that resembles the measured profile from the wind tunnel, and that also give a reasonable profile after passage of the roughness elements, was chosen. Figure 6.2 shows the velocity profiles at the inlet and just in front of the city model, after passage of the roughness elements, including the corresponding data from the wind tunnel.

Simulating the roughness elements is a considerable cost in the simulation. In fact there are more cells assigned to the floor and roughness elements than there are to the houses. The roughness

Boundary	Velocity	Pressure	Concentration
lowerBC	fV=0	zG	zG
Houses	fV=0	zG	zG
Sides	fV=0	zG	zG
Inlet	fV	zG	zG
Outlet	zG	fV=0	zG
Ceiling	zG	zG	zG
source	fV=0.08	zG	fV=1

Table 6.1 *Simulation boundary conditions for FOI simulation. fV=fixed Value condition. zG= zero Gradient condition.*
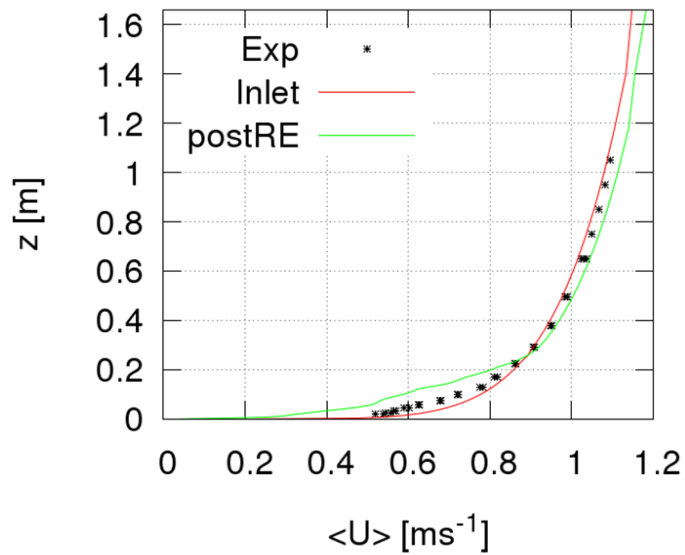

Figure 6.2 *Wind profiles. Prescribed inlet velocity and velocity on center plane after passage of roughness elements, together with measured values from the wind tunnel.*

elements are however important for a reasonable growth of turbulent kinetic energy. Compare figure 6.1 where the growing subgrid kinetic energy is shown.

6.5   Calculation set-up and control

Two simulations were carried out. In addition, a precursor simulation was made to initiate the velocity field. This simulation ran for four seconds of simulated time. The resulting wind field was used as a start wind field for both the neutral release, and the dense gas release simulations. Simulation statistics are given in table 6.2. The neutral release simulation was visibly developing over the first 10 seconds after which averaging started. Table 6.2 summarizes the parameters.

	Neutral gas	dense gas
simulated time	23.5 s	17.45 s
averaging time	13.5 s	17.3 s
time step	$5 \cdot 10^{-4}$ s	$5 \cdot 10^{-4}$ s
Max Courant	≤ 0.6	≤ 0.6

Table 6.2   *Simulation setup for FOI simulation.*

6.5.1   Averaging times

The domain length is given in Section 6.3 as 12 meters. Given the reference flow speed of 1 m/s, a domain flow through would be 12 seconds. The actual city spans approximately 5 meters, giving a flow past of roughly 5 seconds. From these scales it was estimated that for a neutral release at least one flow through (similar to two city flow pasts, or 10-12 seconds) would be needed for setting up the flow structures in the city. To achieve well defined averages it was estimated that at least another four city flow pasts would be needed (i.e. another 20 seconds). For the case of dense gas release the estimates were that considerable more time would be needed. Limited resources means that these goals for averaging were not met, c.f. Table 6.2. Results suggest that the estimates for a neutral release were reasonable. Unless otherwise stated figures shown in this section are taken from the times specified in Table 6.2.

6.6   Results

6.6.1   Flow simulation

Figure 6.4 shows mean axial flow (left to right) on a plane 25 mm above the wind tunnel floor. Both neutral and dense gas release cases are shown. It is clear that the axial flow proceeds vividly through the city as long as streets are approximately aligned with the flow. However, the orientation of the houses and streets relative to the flow is such that most of the streets are at an angle to the oncoming flow. This causes a considerable retardation throughout most of the built up area. In

particular Champs-Élysées (c.f. Figure 6.3), which is almost perpendicular to the oncoming flow, shows very slow moving, intermittent flow. Conversely Avenue Montaigne, in the bottom of the figure, is open along the flow and shows almost no retardation of the flow. The same is true in the upper part of the figure where flow velocities are high during approximately one block, but decays rapidly when approaching the wider crossing streets (Avenue Marceau and Avenue George V).
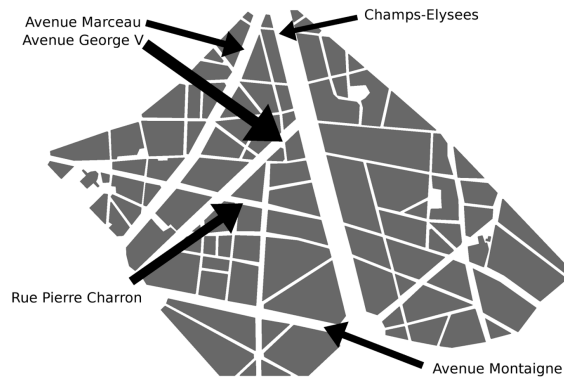

Figure 6.3 *Map of Paris domain with street names referenced in the text.*
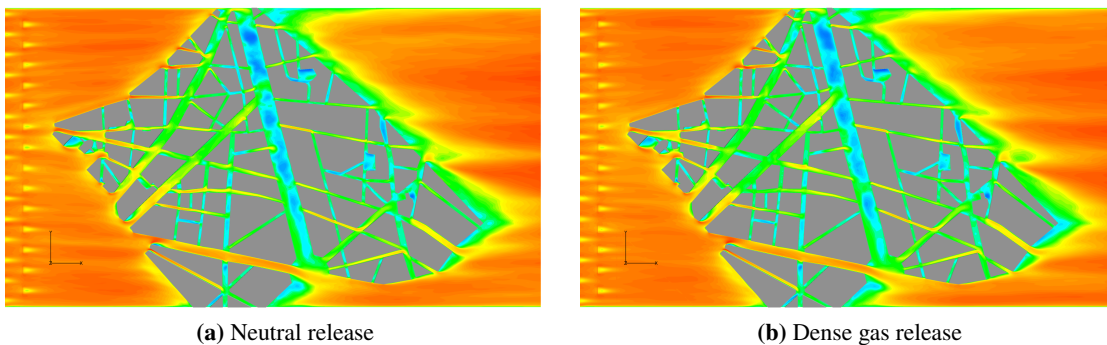

(a) Neutral release

(b) Dense gas release

Figure 6.4 *Mean values of axial velocity at 25 mm above floor. Color scales are the same in the two figures.*

Figure 6.5 shows the spanwise flow, across the wind tunnel axis. Here, it is evident how the oncoming flow is diverted to the sides of the city model. At the same time, the wide streets marking the end of the axial flow in Figure 6.4 show a very strong component of flow transverse to the wind tunnel. These two streets mark an exception to the rule with their strong transverse components. It is interesting to note that although the Champs-Élysées is at a sharp angle to the flow and could be expected to show a rightward (down in the figure) motion, it shows instead a split image. The lower part of the boulevard shows a rightward motion (blue, motion down in the figure), while the upper part of the boulevard is forced with a leftward (red, upward in the figure) motion by the joining wider streets.

Figure 6.6 shows the mean vertical flow. The two panels are very similar showing slight rising motion along the upwind sides of obstacles, and similar sinking motion downwind of the obstacles. Looking at Champs-Élysées, with is almost perpendicular to the oncoming flow, there is a clear canyon vortex present with sinking flow on the right hand side and rising on the left-middle part of
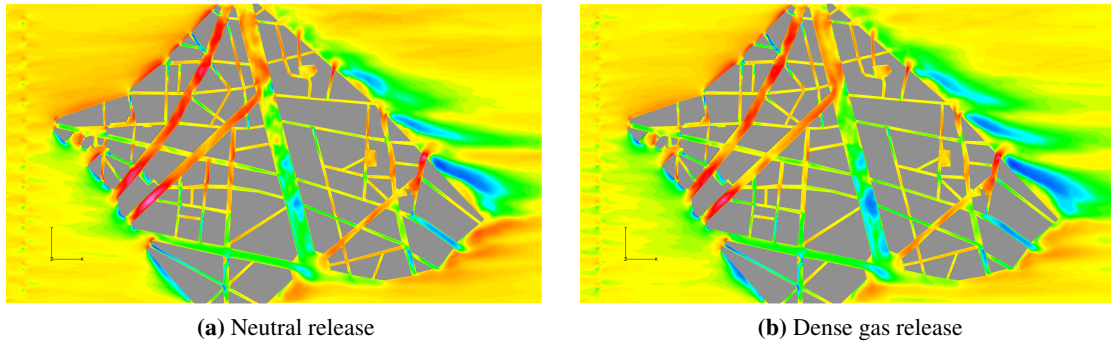
(a) Neutral release   **(b)** Dense gas release

Figure 6.5 *Mean values of spanwise flow velocity at* 25 *mm above floor. Color scales are the same in the two figures.*

the street. More complex is the wake interactions on the right, downwind side of the houses. There is a clear interaction between the transverse and vertical motion as flow exits the narrower streets while the entire lee-ward side of the house limit is sloping relative to the flow.
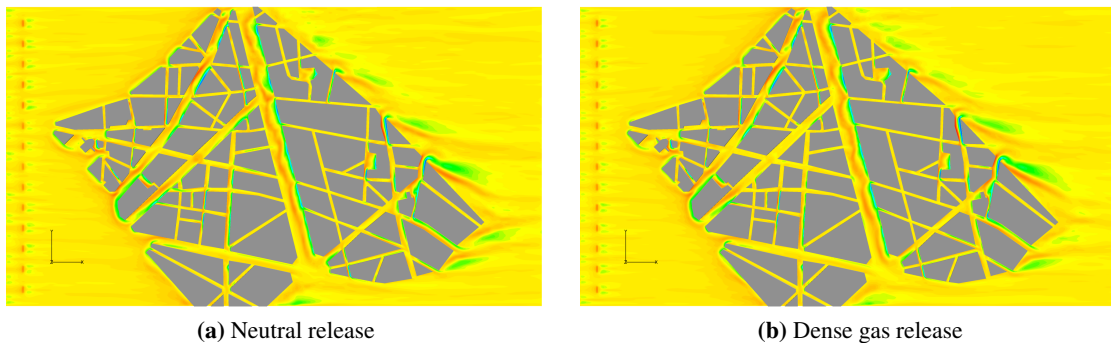

(a) Neutral release   **(b)** Dense gas release

Figure 6.6 *Mean values of vertical flow velocity at* 25 *mm above floor. Color scales are the same in the two figures.*

Figures 6.4 – 6.6 all include double panels, for the cases of neutral and dense gas releases, respectively. Although these have not been commented on, there are slight but distinct differences. These will be addressed following a description of the gas concentration, required for the understanding of the induced effects on the flow.

6.6.2 Dispersion results

Figure 6.7 shows an illustration of the instantaneous dispersed gas cloud using an iso-surface of the concentration. This figure shows clearly the very different nature of the dispersion of neutrally buoyant or dense gases. While the neutrally buoyant gas is forming into a plume-like structure, the dense gas is spreading out through the streets eventually covering much of the simulated city area. This spreading is also visible in the concentration on a plane 25 mm above the surface seen in the same figure. Concentrations are the same in between the planes showing the much higher local

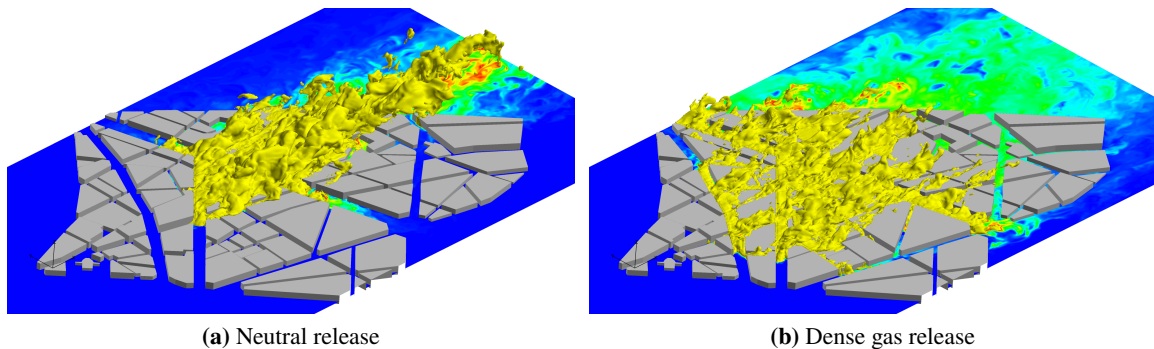concentration below the cloud in the neutral case, but also the much wider area affected by the dense gas.

(a) Neutral release   **(b)** Dense gas release

Figure 6.7   *Iso-surfaces of concentration of neutral and dense gas. Also shown are concentration on a surface at* 25 *mm above the floor. Instants given in Table 6.2*

For a more detailed study, Figure 6.8 shows the instantaneous concentration on a plane 25 mm above the wind tunnel floor. This is one of the most informative comparisons of the different behaviour of neutral and dense gas dispersion. The neutral gas (Figure 6.8a) follows a mean flow direction that is mainly down-wind, i.e. to the right, following the transverse channeling previously seen in Figure 6.5. This cleary shows a strong channeling effect. Almost nothing of the gas escapes along the streets in the axial direction. Figure 6.8b shows a completely different view. Here, the release location is detectable by the strong concentrations, but the gas has spread out almost isotropically. The dense gas is in fact present in considerable quantity even one block straight upwind of the source. Obviously, referring back to Figure 6.4 the dispersion is helped by the fact that the axial flow is weak here, due to the upwind transverse streets. The dispersive pattern of figure 6.8b differ further from the neutral one in subpanel (a) in that it is not directly linked with the flow. Instead, locally, the governing force is a mixture of background flow and the internal buoyant force. This manifests itself not only in the flow upwind directly from the source but also in how gas travels strongly along all the side roads to the main street along which the neutral gas moves (Avenue George V). A detailed study of the figure shows further interesting features. For example, looking due down-stream from the release, right in the figure, it appears as if there is an area of lower concentration, extending to the next crossroads. Looking further downstream from there, the concentration has increased. An obvious explanation could be that it is a variation in time, rather than space.

Figure 6.9 shows the mean concentrations on the same plane, 25 mm above the wind tunnel floor. Recall that the averaging time is insufficient for the neutral case, and probably very much insufficient for the dense gas case. Nevertheless, bearing this in mind, we can compare the mean and instantaneous concentrations. Except for some variation at the far limit of the cloud, the neutral gas concentrations look very much like its instantaneous version in Figure 6.8a. Similarly, the dense gas mean concentration looks similar to the instantaneous field in Figure 6.8b. From Figure 6.9 it seems the dense gas reaches about one block in counter-mean-flow direction. It is clear here (given the limited averaging time) that the decreasing-increasing behaviour of the concentration as it moves downstream that was visible in Figure 6.8 still remains. In fact, it is even more clear in the average field. The explanation can be seen in Figure 6.11 showing the mean concentration from the dense gas release, on a vertical plane along the downwind direction from the source. Houses are outlined
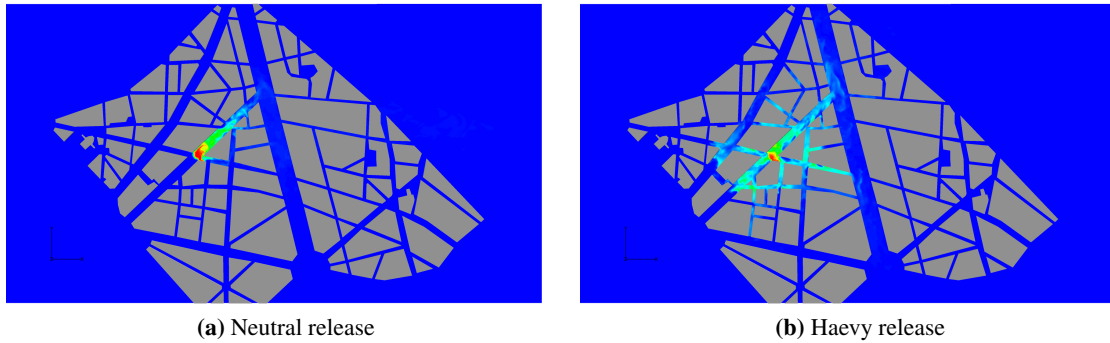
(a) Neutral release   **(b)** Haevy release

Figure 6.8 *Instantaneous values of concentrations at $25mm$ above floor. Color scales are the same in the two figures.*

for reference. It is clear here that what appears in Figure 6.9 to be an increase in concentration is in fact the wave-like behaviour of the upper limit of the dispersed dense gas. Figure 6.10 show the scaled concentrations, similar to those in Figure 5.37, but for the source 2 scenario.
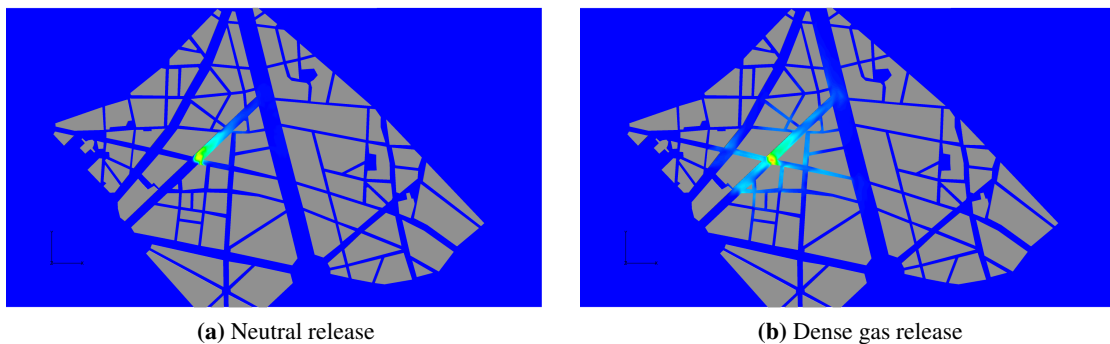

(a) Neutral release   **(b)** Dense gas release

Figure 6.9 *Mean values of concentrations at 25 mm above floor. Color scales are the same in the two figures.*

Figure 6.11a also shows how the upstream propagation of the dense gas is fairly constant over the first block of houses and then forced downwards. Figure 6.11b shows the mean vertical velocity in same plane as Figure 6.11a. The figure shows how the dense gas produces a low level barrier along the street forcing the oncoming flow to rise over the release location and then sink back in the wake, causing the relatively strong downward motion that pushes the dense gas on the downwind side closer to the ground.

Clearly, the dense gas is flowing upwind (left in the figure) from the source towards the first intersection. For reference, Figure 6.11c shows the mean velocity in the axial direction. This is close to, but not the same as, the plane of the figure, the figure also uses a different color scheme to enhance the differences. The figure shows how the dense gas is indeed inducing a backwards flow opposing the background flow. This flow is not strong, but it is persistent. Again, the figure indicates the rising motion of the oncoming flow as it reaches the backward flow. Figure 6.11 also indicates that this effect is strongest over the first block, where the dense gas is forced from its back by the source emitting more gas. As soon as the gas reaches the crossroads, there is the possibility
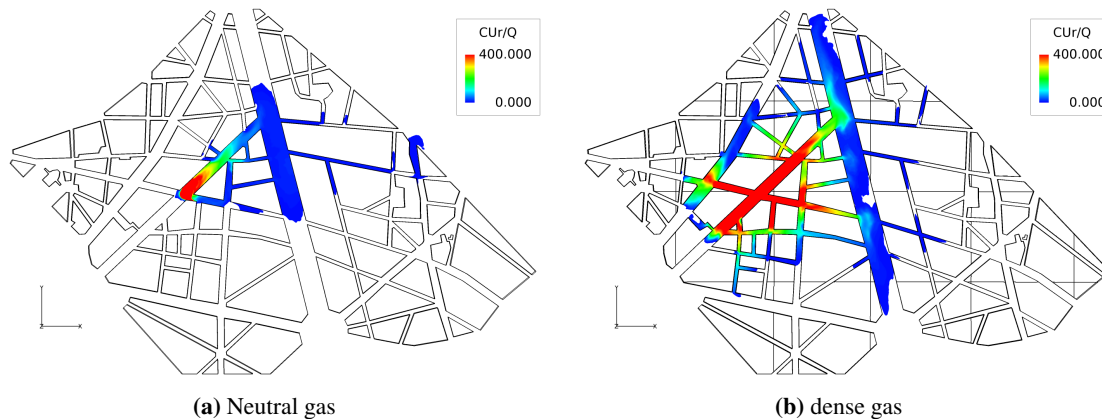
(a) Neutral gas   **(b)** dense gas

Figure 6.10 *Normalized mean concentration at* 10 *mm above the floor in Paris with release from source 2.*

of the dense gas spreading laterally, rather than opposing the oncoming flow. When that possibility arises, the dense gas immediately stops progressing upwind.

Also, referring back to Figure 6.9, even in the same direction that the neutral gas is dispersing, there is a higher concentration of the dense gas. This is due to the dense gas concentrating close to the floor. Figure 6.12 shows a section along the Avenue George V, i.e. almost perpendicular to Figure 6.11. Here it is clear from Figure 6.12a, showing the mean concentration, how the gas is located close to the floor. Panel 6.12b shows the mean cross wind tunnel velocity along the same section. The color scale in Figure 6.12b is saturated so the maximum values are not distinguishable. It is however also symmetric around zero and shows clearly how the mean background flow from right to left in figure, colored yellow-red, is lifted over the dense gas that is flowing left to right (blueish) close to the floor. This is further substantiated by the mean vertical velocity shown in Figure 6.12c. Interestingly, Figure 6.11b also seems to suggest that there may be a turbulent shedding of background flow in lee of the dense gas obstacle created by the source. In fact, close study of Figure 6.12a suggest that the upwind slope of the dense gas dome is sharper than the downwind slope. It is possible that a similar feature is present also in Figure 6.11, although not as pronounced.

Figure 6.13 shows the same perspective for the neutral gas as Figure 6.12 do for the dense gas. Comparison of the figures highlights the distinct differences in dispersive behaviour. It is clear how the neutral gas released is immediately transported with the flow and upwards. The cross wind tunnel flow is also in Figure 6.13 lifted as it encounters the source, but this lifting motion is much weaker and occurs only at the location of the source, there is no spreading of the gas opposite to the background flow.

The stronger vertical transport of the neutral gas is also visualized in Figures 6.14 and 6.15, showing instantaneous and mean concentration respectively, both at 80 mm above the floor. This level is above several of the buildings which is why fewer buildings are visible. The figure show a similar pattern to that discussed previously, where the neutral gas is moving upwards, and then transported with the mean flow. This transport also means that gas within the plume created is transported downward with downstream turbulent eddies. The dense gas is also transported upward, when it is mixed with surrounding neutral air. For comparison the panels of Figures 6.14 and 6.15 all use
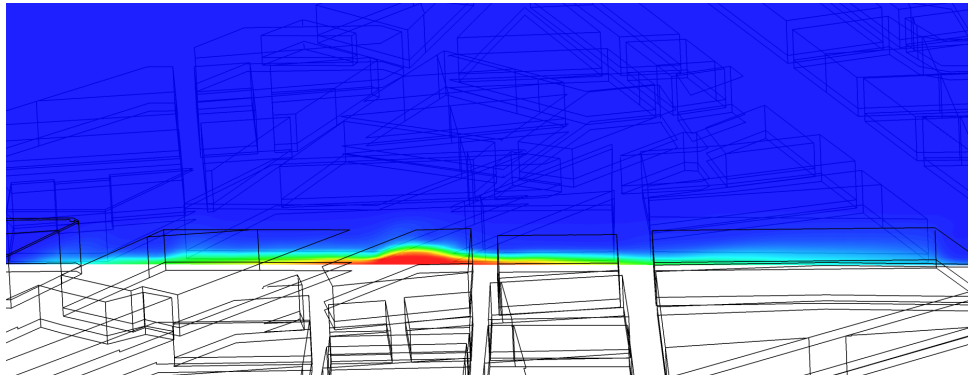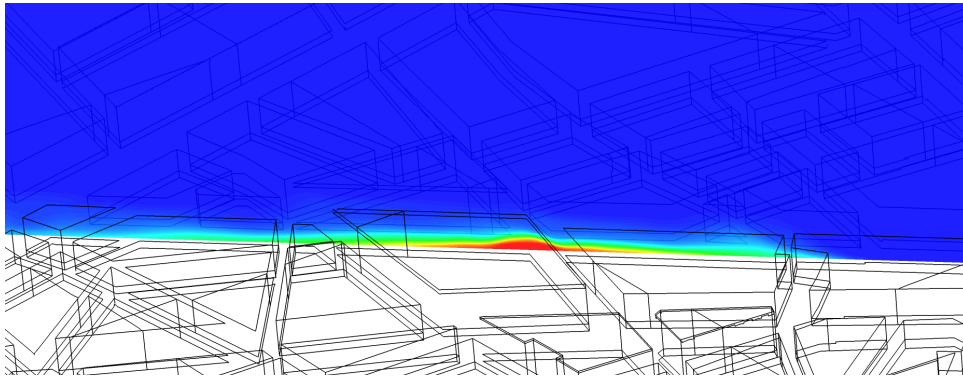
(a) Mean concentration
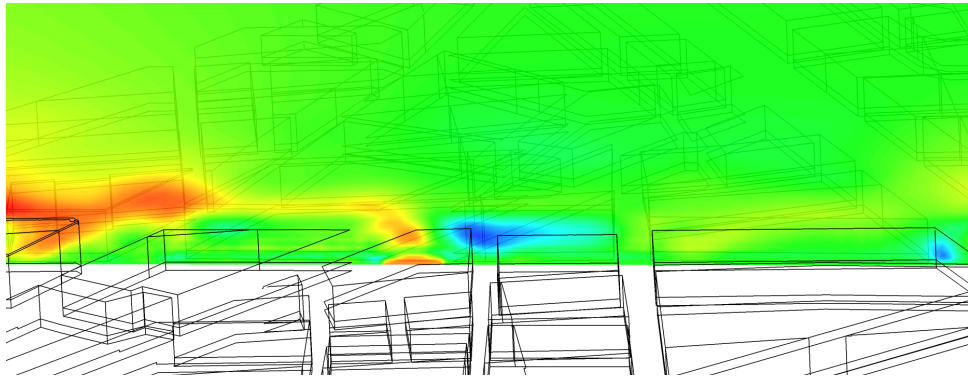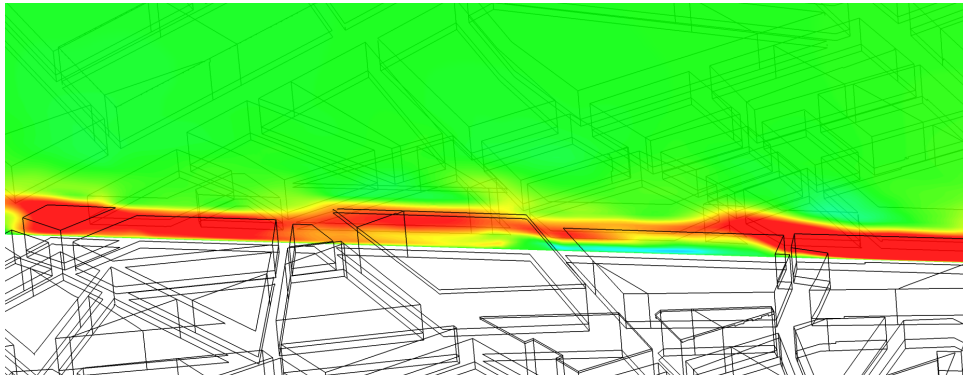

(b) Mean vertical velocity
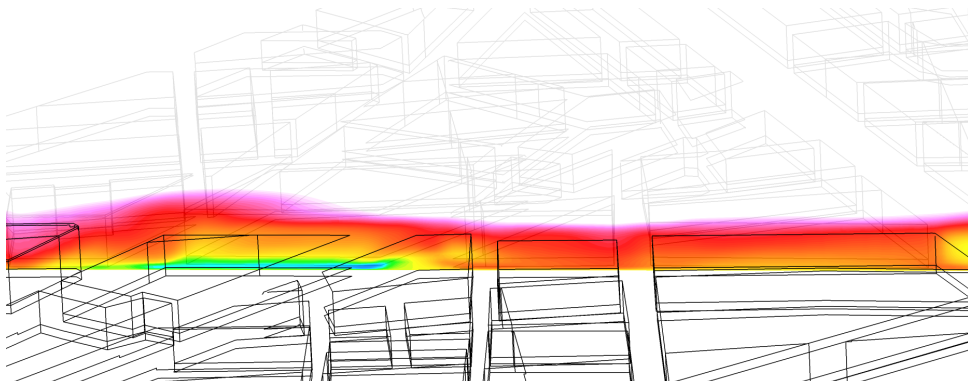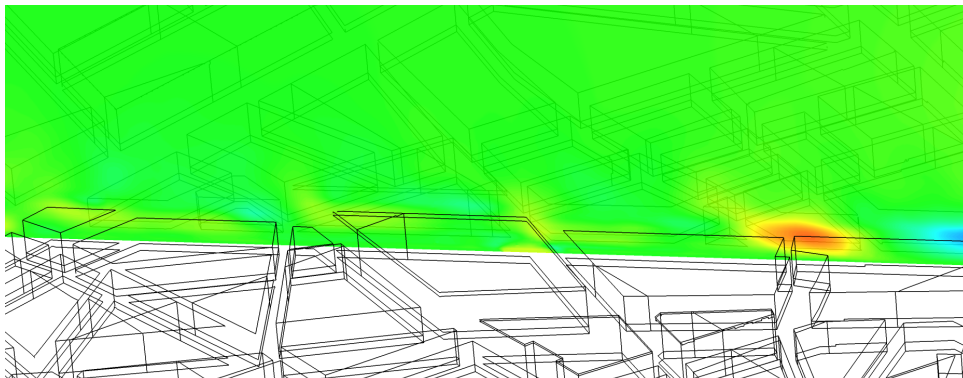

(c) Mean axial velocity

Figure 6.11 *Section following Rue Pierre Charron (c.f. Figure 6.3) for a dense gas release. Note that color scheme in (c) is different and that the plane is not strictly aligned with the wind tunnel axis.*
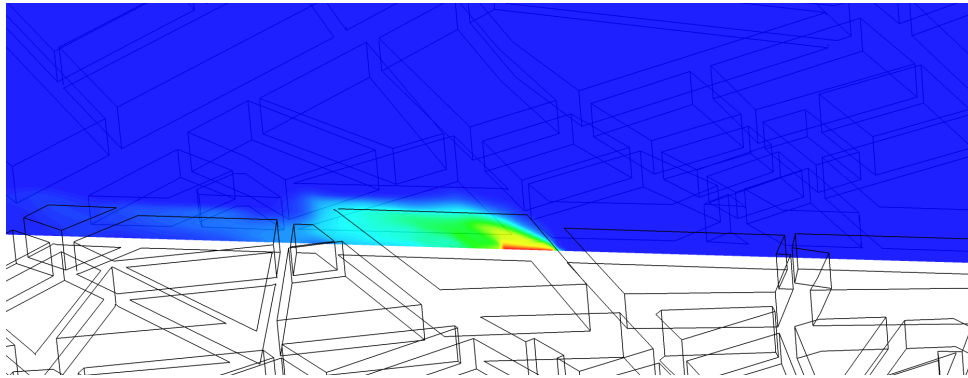
(a) Mean concentration
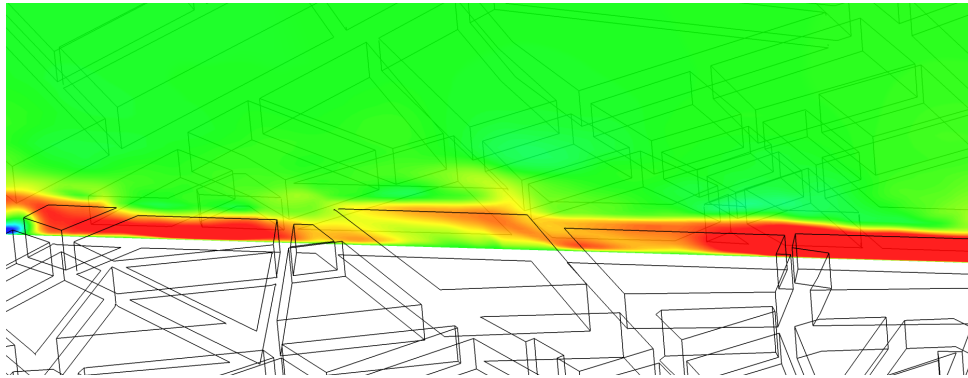

(b) Mean vertical velocity
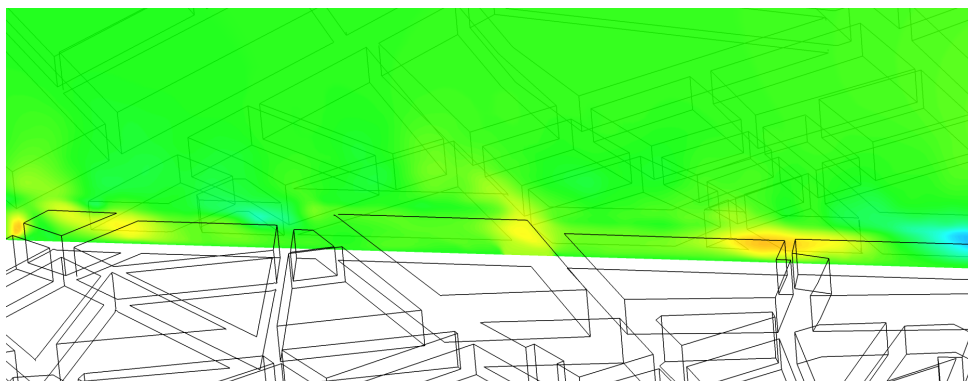

(c) Mean corss wind tunnel velocity

Figure 6.12   *Section following Avenue George V (c.f. Figure 6.3) for dense gas release. Note that color scale in (b) is saturated for the highest values and that the plane is not perpendicular to the wind tunnel axis.*

(a) Mean concentration

(b) Mean vertical velocity

(c) Mean cross wind tunnel velocity

Figure 6.13 *Section following Avenue George V (c.f. Figure 6.3) for release of neutral gas. Note that color scale in (b) is saturated for the highest values and that the plane is not perpendicalar to the wind tunnel axis.*
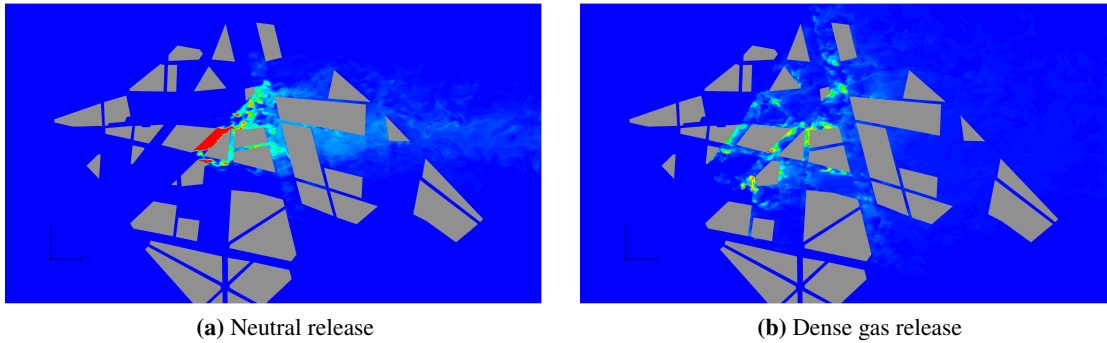
(a) Neutral release   (b) Dense gas release

Figure 6.14 *Instantaneous values of concentrations at* 80 *mm above floor. Color scales are the same in the two panels.*

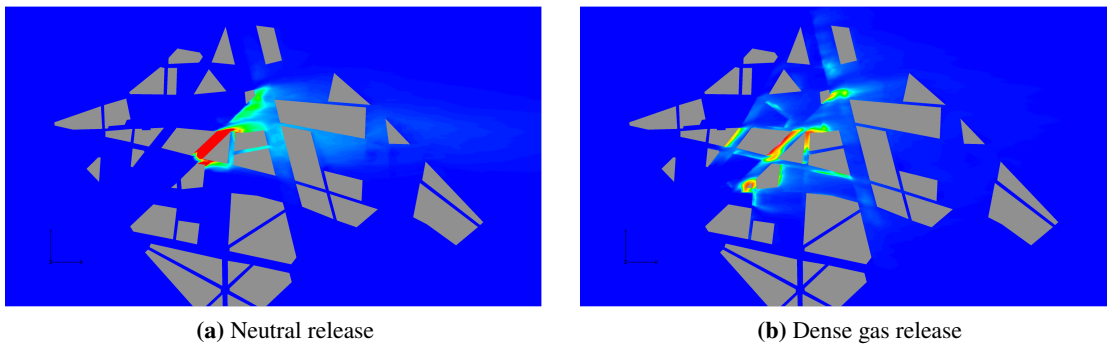(a) Neutral release   (b) Dense gas release

Figure 6.15 *Mean values of concentrations at* 80 *mm above floor. Color scales are the same in the two panels.*

the same color scale (based on dense gas concentrations). This scale is, however, saturated for the neutral case, hiding the fact that the concentration in the main plume is considerably higher (maximum mean value is ≈ 0.3 or about six times the maximum mean dense gas concentration) than that for the dense gas. It is also clear from Figures 6.14 and 6.15 that the neutral gas rises with the background flow while the rising gas in Figure 6.15 is mostly located on the upwind sides of buildings, associated with the updrafts seen in Figure 6.6 and expected from urban canyon flow.

6.6.3 Comparison to measurements

Figure 6.16 shows horizontal profiles of simulated mean concentrations together with measurements for the neutral 6.16a and dense 6.16b gas simulations, at several locations downstream of the source. The profiles are located at $z = 120$ mm which places them at a considerably higher level than the surfaces shown in Figure 6.15 ($z = 80$ mm). As related in Section 6.5 and the opening paragraph of this section, the averaging times of the simulations presented here are less than sufficient. Despite the short averaging time and the large height of profiles, the neutral gas concentrations (Figure 6.16a) show agreement with the measurements. The profile closest to the source, at $x = 500$ (red in figure) have mostly a very good agreement. It is only the dip at about $y = 0$ mm that is exaggerated in the simulation. Moving further downstream, the maximum simulated values become

smaller than the experimental ones. This is in all likelihood the effect of too short averaging as the actual concentration decreases with distance from the source. Very good agreement is achieved in simulating the asymmetry of the concentration, in particular capturing the details of the leftward drift of the dispersed cloud (tail into positive values of y).

The dense gas release shown in Figure 6.16b shows similar behaviour but also more noise. Note that the vertical axis is different from Figure 6.16a. Maximum values of Figure 6.16b are only less than half of the maximum values of Figure 6.16a. The combination of low absolute values and short averaging time causes the rather high level of noise seen in the dense gas concentrations. Nevertheless, again many of the off center features are captured by the simulation. Most of the spanwise variability is captured in each of the profiles, although the amplitude is exaggerated in the closest ones.
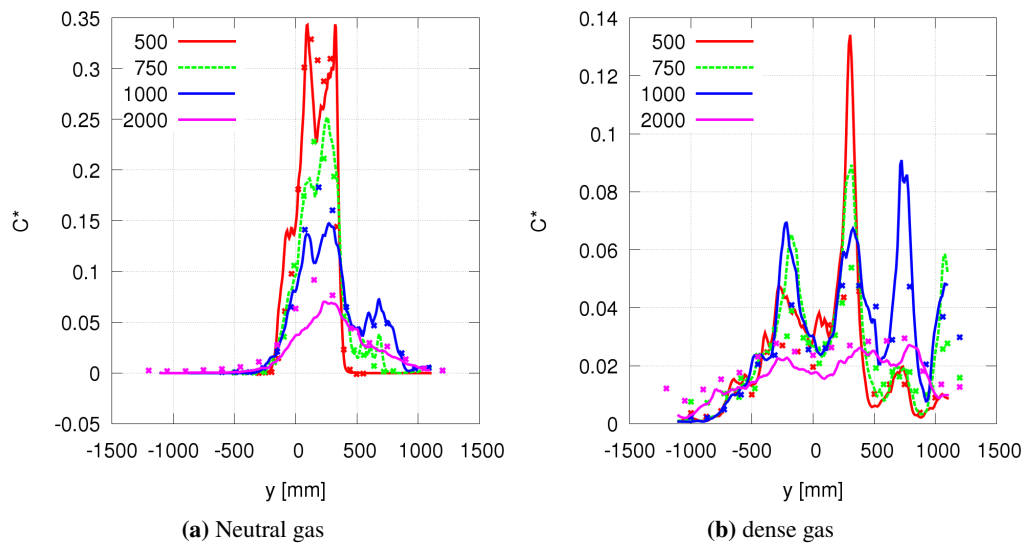

(a) Neutral gas   **(b)** dense gas

Figure 6.16 *Horizontal profiles of normalized concentration across wind tunnel at given locations (x[mm]), 120 mm above the floor. Lines represent simulation results and symbols experimental values.*

Figure 6.17 shows vertical profiles of the mean gas concentration at given measured locations. These profiles are taken at three locations for the neutral gas release, Figure 6.17a, and five locations for the dense gas release, Figure 6.17b. Neutral gas release concentrations in Figure 6.17a show good agreement between simulation and experiments above approximately 120 mm (incidentally the level of the horizontal profiles presented above). Below that height all simulated data underestimates the measured concentration. For reference, three extra vertical profiles are included in Figure 6.17a, one for each of the measured locations, all three taken three seconds earlier in the simulation/averaging. These earlier profiles seem to agree with the earlier suggestion that the averaging times are too short. It is likely that an additional 10-20 seconds of averaging would alleviate the differences seen in Figure 6.17a. Figure 6.17b shows similar profiles for the dense gas release. These profiles show the strong influence of gas density, similar to Figures 6.11a and 6.12a. They also indicate the very low values of concentration available at the height of 120 mm. It was assumed earlier that the averaging time required for dense gas releases would be larger than that for neutral releases. The results shown here rather suggests the opposite. It may be that there is in fact a local balance

between dense gas density, source strength and channel (street) width that determines the vertical extent of dense gas, and thereby the low level concentrations. The limited averaging time means that concentration RMS-values are inconclusive and can not be used to determine weather the low level flow is turbulent or not.
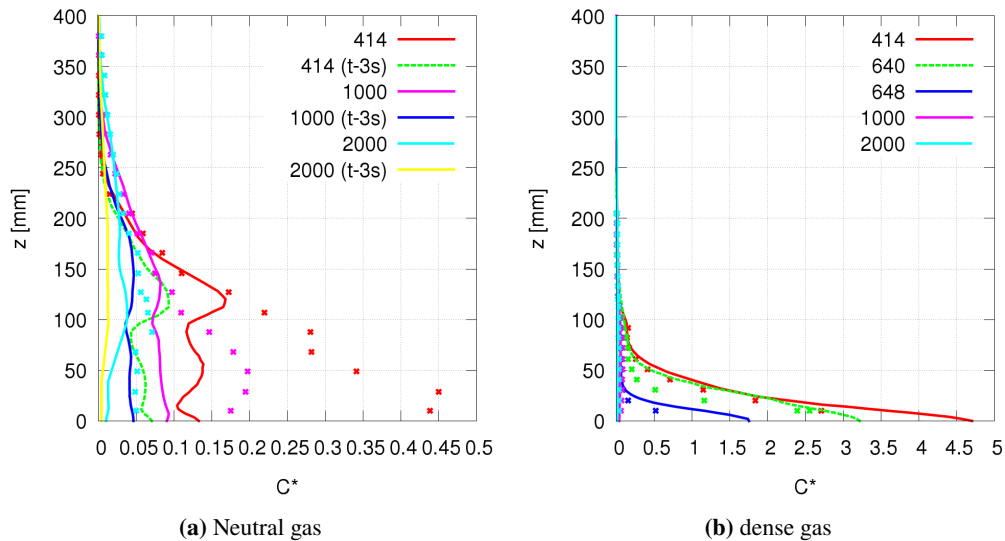

(a) Neutral gas   **(b)** dense gas

Figure 6.17   *Vertical profiles of normalized concentration at given streamwise locations (x[mm]). Lines represent simulation results and symbols experimental values.*

Figure 6.18 shows the scaled concentrations in the LES simulation compared to the experimental values for all measurements 10 mm above the floor. It is only the very largest simulated values that fall outside the standard deviation of the measurements (not shown). Most of the simulated points of the neutral release underestimate the measurements. Looking back to the vertical profiles in Figure 6.17 this is not surprising. This may again very well be an effect of too short averaging time. Looking at the dense gas simulations of Figure 6.18b the much closer agreement from 6.17b is also present. This suggests that the behaviour seen in the vertical profiles is common within the simulation.

6.6.4   Measure of effectiveness

The measure of effectiveness [26] has been computed for the profiles given in Figures 6.16 and 6.17. The MOE1 values are given in Table 6.3. Note that vertical profiles at $x = 640$ mm and $x = 648$ mm are not taken in the neutral case. Similarly the two-dimensional MOE2 are given in Figure 6.19.

The MOE1 ([26]) values are the area integral of simulation and experiment overlap divided by the total simulated and experiment area integral. This value is ideally unity. The MOE2 values are the area of overlap (A_{TP} for True Positive) divided by the area of observation (A_{EXP} for Experiment) versus A_{TP} over area of simulation (A_{LES}). Both dimensions should ideally be unity. In Figure 6.19 the abscissa shows non-false negatives and the ordinate shows non-false positives. In relational to dispersion of hazardous material false positives (low value on ordinate) is undesirable while false negatives (low value on abscissa) may prove fatal.
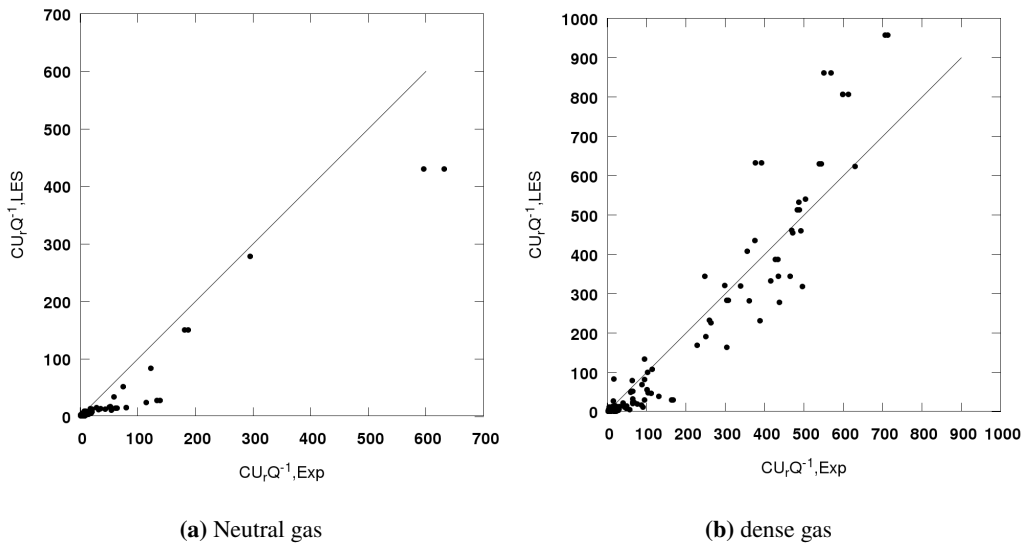
(a) Neutral gas   **(b)** dense gas

Figure 6.18 *Normalized concentrations at 10 mm above the floor in wind tunnel experiments and LES simulations.*

profile $x[mm]$	MOE	
Vertical profiles		
	Neutral	Dense
414	0.56	0.77
640	-	0.58
648	-	0.62
1000	0.70	0.70
2000	0.80	0.58
Horizontal profiles		
	Neutral	Dense
500	0.82	0.72
750	0.8	0.70
1000	0.86	0.76
2000	0.78	0.76

Table 6.3 *One dimensional measure of effectiveness ([26]), MOE1, for profiles in Figures 6.16 and 6.17.*
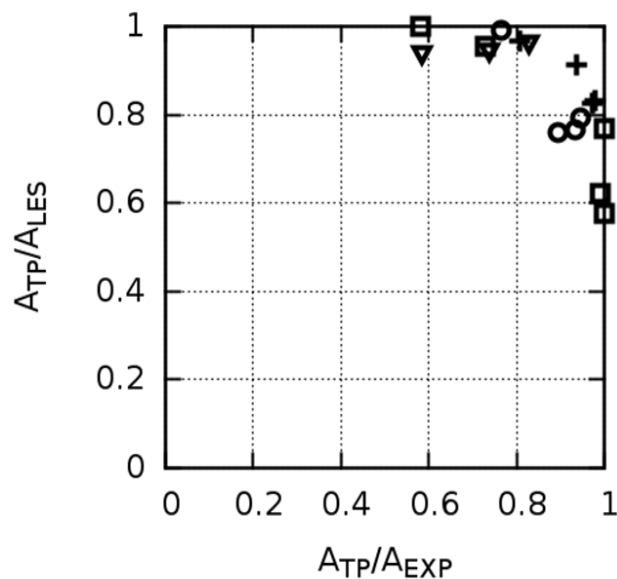
Figure 6.19 *Measure of effectiveness showing amount of non-false positive (A_{TP}/A_{LES}) prediction on vertical axis and non-false negative (A_{TP}/A_{EXP}) prediction on horizontal axis; for Paris with release from source 2 with (+) for neutral horizontal profiles, ($\triangledown$) for neutral vertical, ($\circ$) for dense horizontal and ($\square$) for dense vertical profiles.*

6.7   Conclusions

Despite the short averaging time the simulations presented here suggest several interesting features of the dense gas dispersion. The comparisons with measurements in Figures 6.16 and 6.17 show that the dense gas concentration is amplified by as much as a factor of ten close to the floor, compared to a similar release of a neutrally buoyant gas. The decay of concentration with height appear to mostly take place over the height of the buildings. This is probably caused by the cooperative effect of building wakes and gas subsidence. The street plane views of Figures 6.11, 6.12, and 6.13 show how the dense gas affects the low level flow in the streets surrounding the source. In these streets the dense gas spreads almost evenly in all directions. Once the first block of buildings are negotiated there appear to be a pause in the spreading counter to the oncoming flow. This is probably due to the possibility for the gas to turn the corner, i.e. a relieving of the channeling effect. Downstream, a similar spread is seen, where the dense gas spreads to the sides and settles on the side preferred by the background flow. Figure 6.12 indicates the very interesting possibility that the released dense gas acts as a lower boundary isolated hill to the background flow, even to the level that there may be vortex shedding on the lee side. Similarly interesting is the wave like behaviour seen in Figure 6.11 where the background flow is pushing the low level dense gas.

Although the simulations shown here are limited in time, the results of this work show that LES is a viable tool for simulation of dense gas dispersion. Despite the simplicity of the dense gas treatment, using only a Boussinesq formulation of buoyancy, results are in reasonably agreement with measurements. This suggests that low level interaction between turbulent properties and dense gas properties is not determining the dispersion. Longer averaging of the fields might resolve the open questions remaining from this work.

A   Appendix

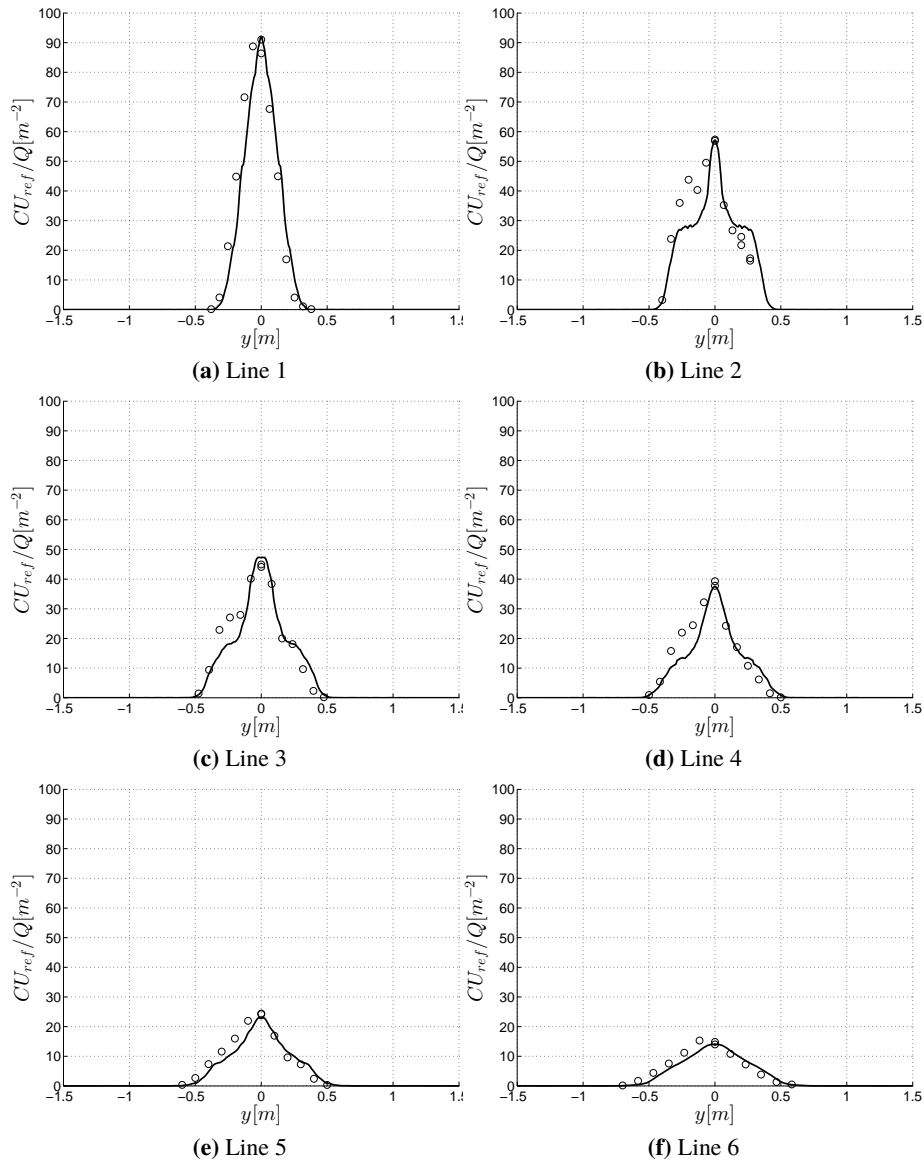## A.1   FFI results from simple array case

Figure A.1   *Horizontal profiles of time averaged normalized concentration of neutral gas. The simulation data is mirrored around $y = 0$. Experimental values ($\circ$) and LES (——).*
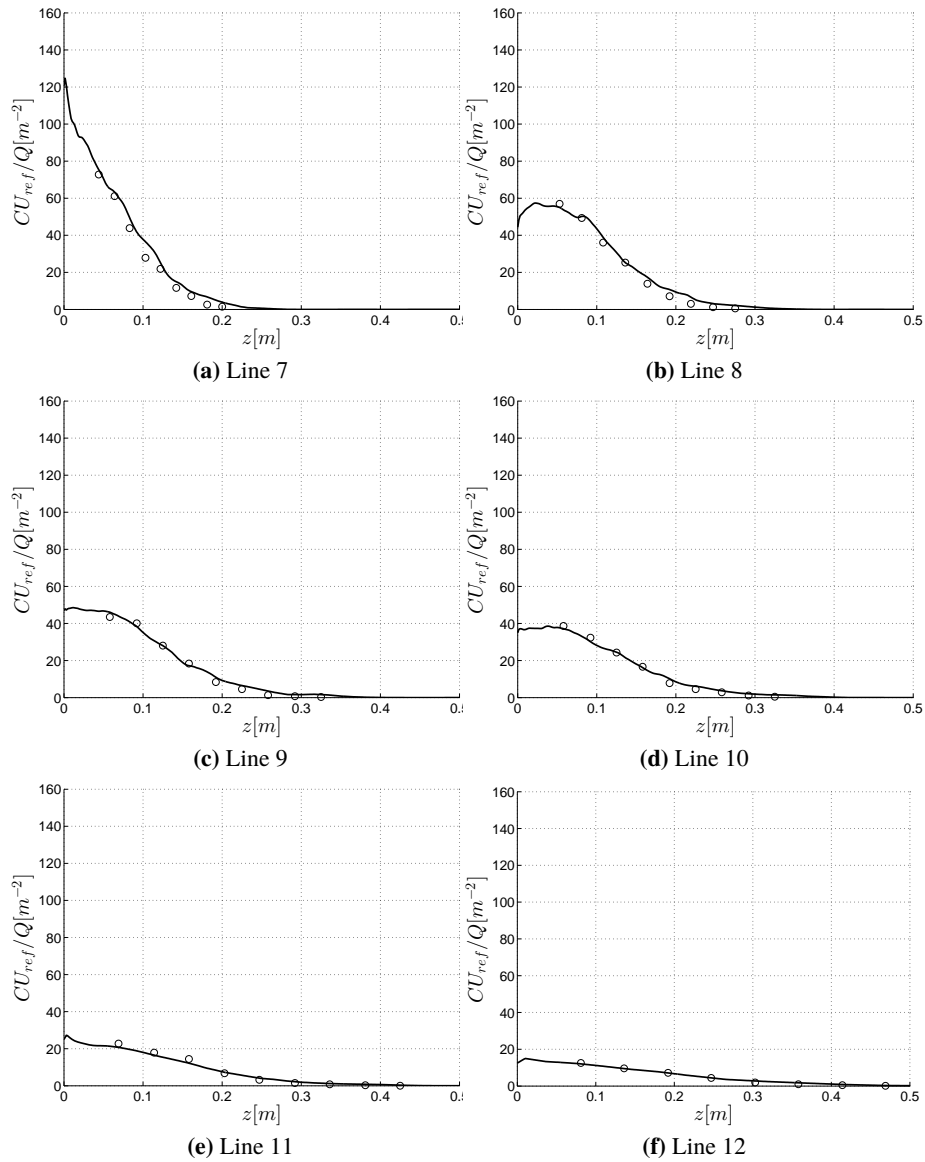
Figure A.2 *Vertical profiles of time averaged normalized concentration of neutral gas. Experimental values (○) and LES (——).*
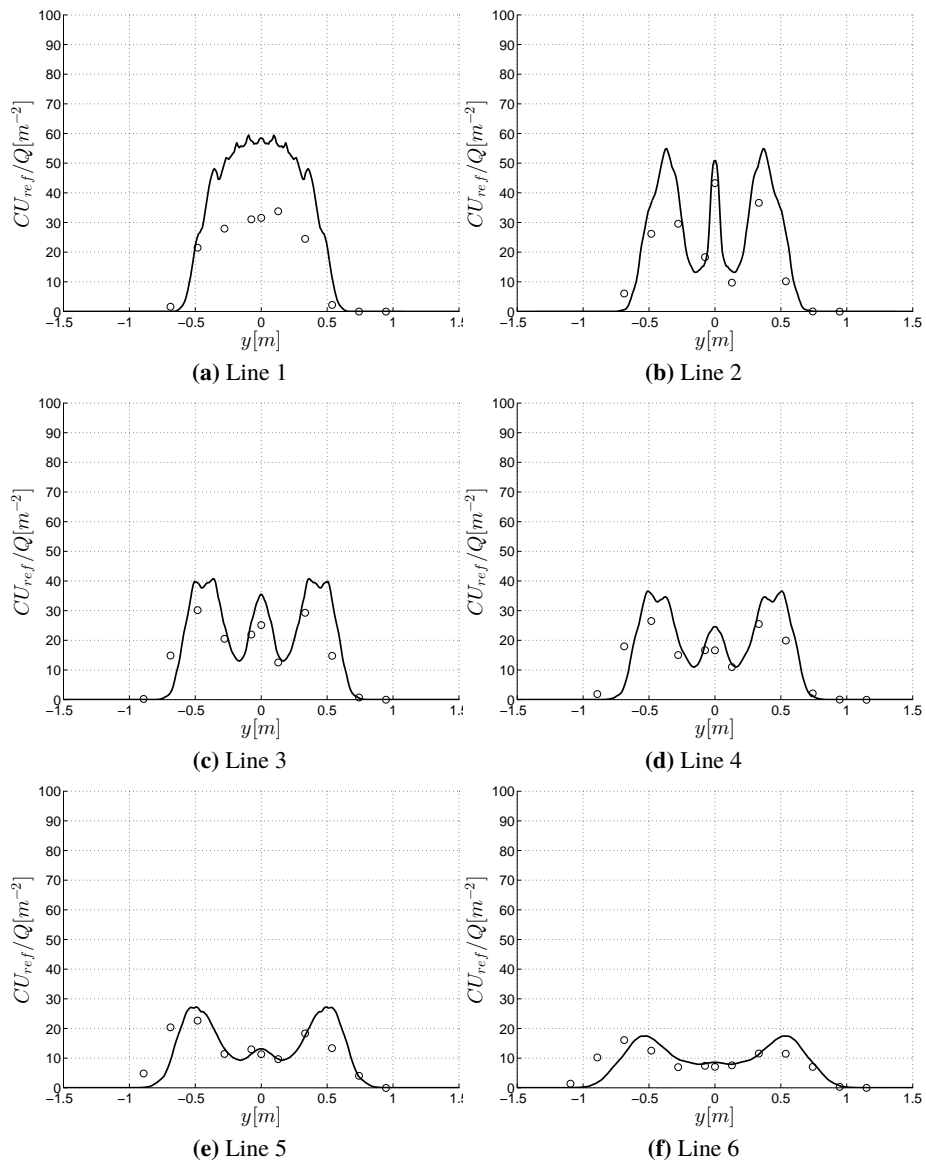
Figure A.3 *Horizontal profiles of time averaged normalized concentration of dense gas. The simulation data is mirrored around $y = 0$. Experimental values (○) and LES (——).*
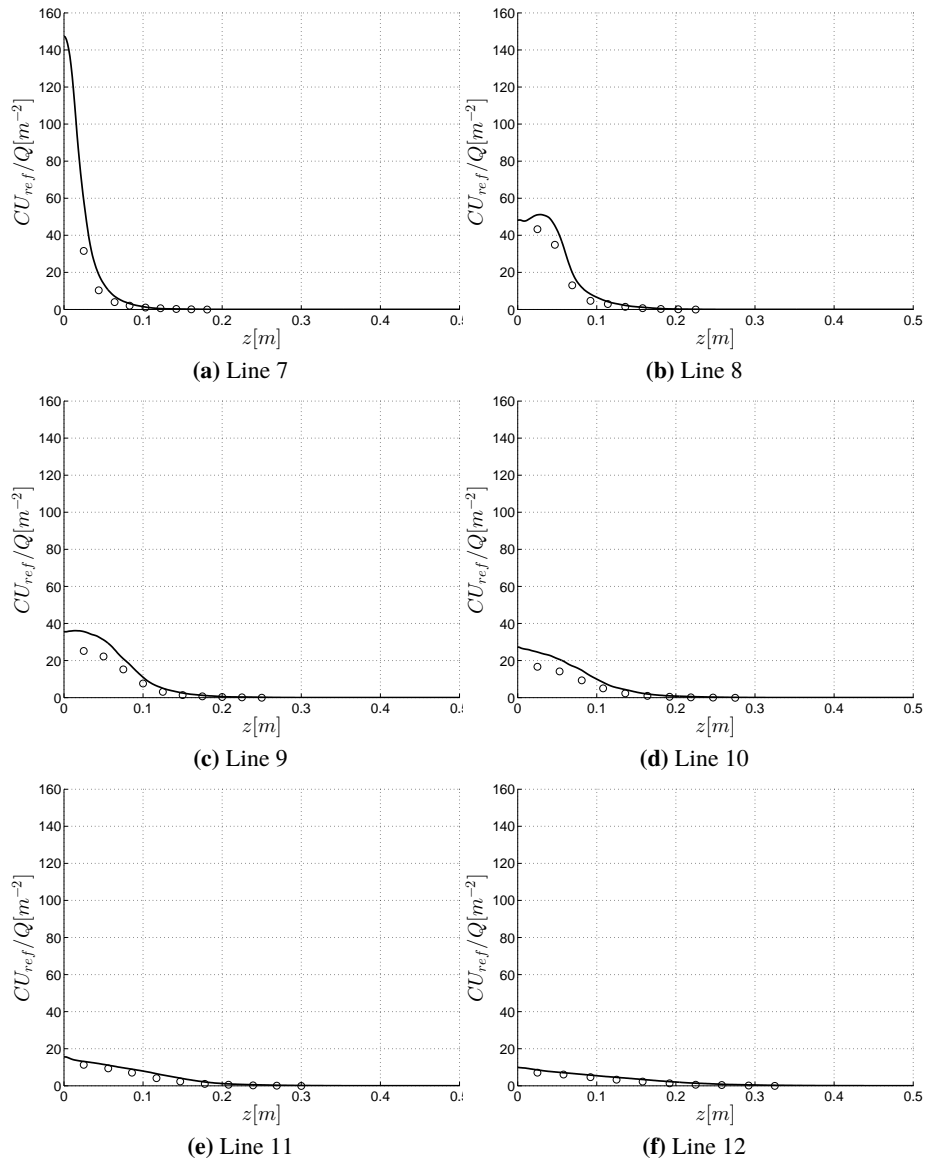
(a) Line 7

(b) Line 8

(c) Line 9

(d) Line 10

(e) Line 11

(f) Line 12

Figure A.4 *Vertical profiles of time averaged normalized concentration of dense gas. Experimental values (○) and LES (——).*
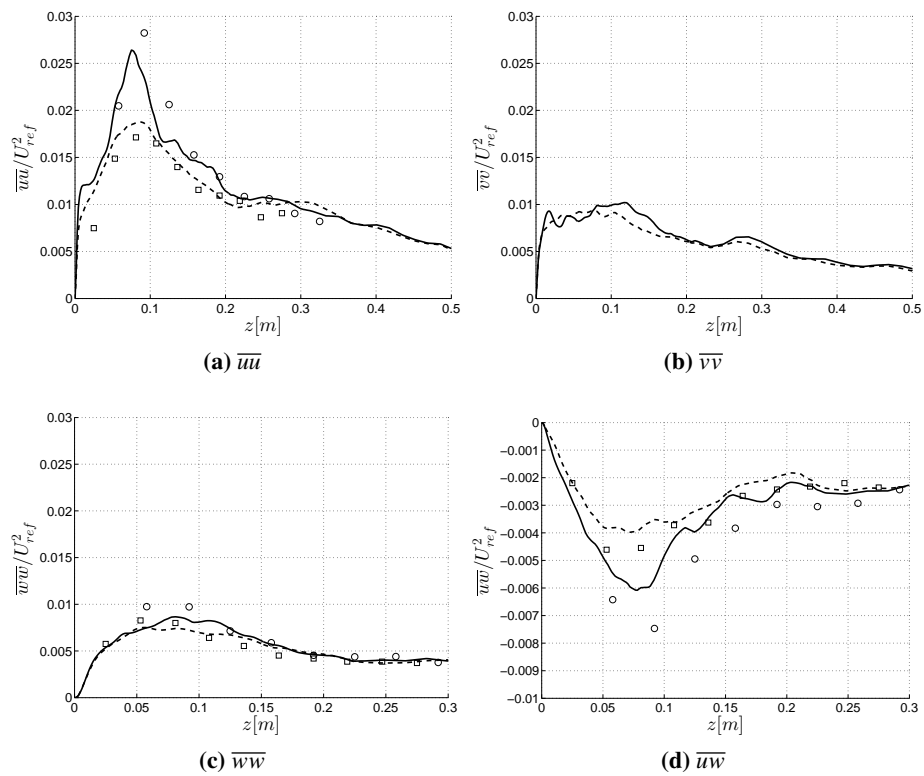
Figure A.5 *Vertical profiles of dimensionless Reynolds stresses taken at line 10. Symbols denote experimental values and lines LES results. Neutral gas (○) and (——). Dense gas (□) and (−−−).*

Bibliography

[1] P. Durbin and B. P. Reif, "The elliptic relaxation method," <u>Closure Strategies for Turbulent and Transitional Flows</u>, pp. 127–152, 2002.

[2] R. L. Lee, R. Calhoun, S. Chan, J. Leone, J. Shinn, and D. Stevens, "Urban dispersion CFD modeling, fact or fiction," in <u>3rd Symposium on the Urban Environment</u>, pp. 14–18, 2000.

[3] W. Coirier, D. Fricker, M. Furmanczyk, and S. Kim, "A Computational Fluid Dynamics approach for urban area transport and dispersion modeling," <u>Environmental Fluid Mechanics</u>, vol. 5, no. 5, pp. 443–479, 2005.

[4] F.-S. Lien and E. Yee, "Numerical modelling of the turbulent flow developing within and over a 3D building array, Part I: A high-resolution Reynolds-Averaged Navier-Stokes approach," <u>Boundary-Layer Meteorology</u>, vol. 112, pp. 427–466, 2004.

[5] F.-S. Lien, E. Yee, H. Ji, A. Keats, and K. J. Hsieh, "Progress and challenges in the development of physically-based numerical models for prediction of flow and contaminant dispersion in the urban environment," <u>Int. Journal of Computational Fluid Dynamics</u>, vol. 20, pp. 323–337, 2006.

[6] J. L. Santiago, A. Martilli, and F. Martin, "CFD simulation of airflow over a regular array of cubes. Part I: Three-dimensional simulation of the flow and validation with wind-tunnel experiments," <u>Boundary-Layer Meteorology</u>, vol. 122, pp. 609–634, 2007.

[7] M. A. McBride, A. B. Reeves, M. D. Vanderheyden, C. J. Lea, and X. X. Zhou, "Use of advanced techniques to model the dispersion of chlorine in complex terrain," <u>Process Safety Environment</u>, vol. 79, pp. 89–102, 2001.

[8] G. A. Perdikaris and F. Mayinger, "Numerical simulation of heavy gas cloud dispersion within topographically complex terrain," <u>Journal of Loss Prevention in the Process Industries</u>, vol. 7, pp. 391–396, 1994.

[9] S. Sklavounos and F. Rigas, "Validation of turbulence models in heavy gas dispersion over obstacles," <u>Journal of Hazardous Materials</u>, vol. A108, pp. 9–20, 2004.

[10] S. Tauseef, D. Rashtchian, and S. Abbasi, "CFD-based simulation of dense gas dispersion in presence of obstacles," <u>Journal of Loss Prevention in the Process Industries</u>, vol. 24, no. 4, pp. 371–376, 2011.

[11] V. Boppana, Z.-T. Xie, and I. P. Castro, "Large-eddy simulation of dispersion from surface sources in arrays of obstacles," <u>Boundary-Layer Meteorology</u>, vol. 135, no. 3, pp. 433–454, 2010.

[12] H. E. Fossum, B. A. Pettersson-Reif, M. Tutkun, and T. Gjesdal, "On the Use of Computational Fluid Dynamics to Investigat Aerosol Dispersion in an Industrial Environment: A Case Study," <u>Boundary-Layer Meteorology</u>, vol. 144, pp. 21–40, 2012.

[13] Y. Liu, G. Cui, Z. Wang, and Z. Zhang, "Large eddy simulation of wind field and pollutant dispersion in downtown Macao," Atmospheric Environment, vol. 45, no. 17, pp. 2849–2859, 2011.

[14] Z.-T. Xie and I. P. Castro, "Large-eddy simulation for flow and dispersion in urban streets," Atmospheric Environment, vol. 43, no. 13, pp. 2174–2185, 2009.

[15] J. Burman, B. A. P. Reif, S. Burkhart, O. Parmhed, and A. Robins, "WP1000 - Scenario definition and dissemination strategy," Swedish Defence Research Agency, FOI Rapport, no. 2015/..., 2015.

[16] A. Robins, P. Hayden, and E. M. M. Wingstedt, "MODITIC wind tunnel experiments," Tech. Rep. 2016/01483, Forsvarets Forskningsinstitutt, 2016.

[17] E. Åkervik and D. Eriksson, "Turbulent boundary layer simulations: comparison with experiments," tech. rep., Technical Report FFI-rapport 2016/00827, Forsvarets Forskningsinstitutt, 2016.

[18] C. T. Inc, "User's and developer's manual. jefferson release version 4.1.0," 2014.

[19] E. D, O. N. A, and Åkervik. E, "Neutrally buoyant gas dispersion within an urban street canyon," MekIT15 Eight national conference on Computational Mechanics, pp. 149–166, 2015.

[20] W. H.G., T. G., J. H., and F. C., "A tensorial approach to cfd using object oriented techniques," Comp. in Physics, vol. 12, p. 629, 1997.

[21] T. Maric, J. Hopken, and K. Mooney, "The openfoam technology primer," 2014.

[22] S. J., "General circulation experiments with the primitive equations. i. the basic experiment," Mont. Wea. Rev., vol. 91, p. 91, 1963.

[23] U. Schumann, "Subgrid scale model for finite difference simualtion of turbulent flows in plane channels and annuli," J.Comp.Phys., no. 18, p. 376, 1975.

[24] S. Menon and W.-W. Kim, "High reynolds number flow simulations using the localized dynamic subgrid-scale model," AIAA paper, no. 96-0425, 1996.

[25] R. Stull, An Introduction to Boundary Layer Meteorology. Dordrecht: Kluwer Academic Publishers, 1988.

[26] S. Warner, N. Platt, J. F. Heagy, S. Bradley, G. Bieberbach, G. Sugiyama, J. S. Nasstrom, K. T. Foster, and D. Larson, "User-oriented measures of effectiveness for the evaluation of transport and dispersion models," Institute For Defense Analysis, no. P-3554, 2001.

About FFI

The Norwegian Defence Research Establishment (FFI) was founded 11th of April 1946. It is organised as an administrative agency subordinate to the Ministry of Defence.

FFI's MISSION

FFI is the prime institution responsible for defence related research in Norway. Its principal mission is to carry out research and development to meet the requirements of the Armed Forces. FFI has the role of chief adviser to the political and military leadership. In particular, the institute shall focus on aspects of the development in science and technology that can influence our security policy or defence planning.

FFI's VISION

FFI turns knowledge and ideas into an efficient defence.

FFI's CHARACTERISTICS

Creative, daring, broad-minded and responsible.

Om FFI

Forsvarets forskningsinstitutt ble etablert 11. april 1946. Instituttet er organisert som et forvaltningsorgan med særskilte fullmakter underlagt Forsvarsdepartementet.

FFIs FORMÅL

Forsvarets forskningsinstitutt er Forsvarets sentrale forskningsinstitusjon og har som formål å drive forskning og utvikling for Forsvarets behov. Videre er FFI rådgiver overfor Forsvarets strategiske ledelse. Spesielt skal instituttet følge opp trekk ved vitenskapelig og militærteknisk utvikling som kan påvirke forutsetningene for sikkerhetspolitikken eller forsvarsplanleggingen.
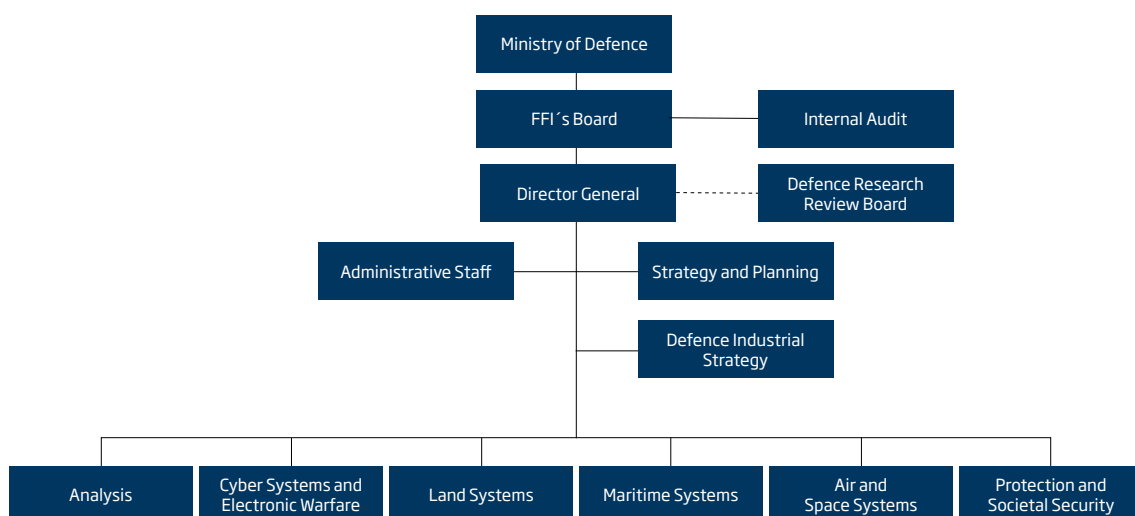
FFIs VISJON

FFI gjør kunnskap og ideer til et effektivt forsvar.

FFIs VERDIER

Skapende, drivende, vidsynt og ansvarlig.

FFI's organisation

FFI **Forsvarets
forskningsinstitutt**
Norwegian Defence Research Establishment